

# Evaluation of position and current sensor technologies for a PMSM used in automotive applications

Master's thesis in Master Program Electrical Power Engineering

NILS HÖGLUND

DANIEL POPOSKI



MASTER'S THESIS 2019

**Evaluation of position and current sensor technologies for a  
PMSM used in automotive applications**

NILS HÖGLUND  
DANIEL POPOSKI



**CHALMERS**  
UNIVERSITY OF TECHNOLOGY

Department of Electrical Engineering  
*Division of Electric Power Engineering*  
CHALMERS UNIVERSITY OF TECHNOLOGY  
Gothenburg, Sweden 2019

Evaluation of position and current sensor technologies for a PMSM used in automotive applications

© NILS HÖGLUND, DANIEL POPOSKI, 2019.

Supervisor: Tomas Gustafsson, CEVT

Examiner: Stefan Lundberg, Department of Electrical Engineering

Master's Thesis 2019

Department of Electrical Engineering

Division of Electric Power Engineering

Chalmers University of Technology

SE-412 96 Gothenburg

Telephone +46 76 795 50 40, +46 73 525 36 73

Cover: Evaluation of position and current sensor technologies for a PMSM used in automotive applications.

Typeset in  $\LaTeX$

Printed by [Reproservice]

Gothenburg, Sweden 2019

# Abstract

This thesis investigates the impact of typical current and position sensor measurement errors on a PMSM. The investigated PMSM is used as the electric traction motor in a dedicated hybrid transmission developed by CEVT. The thesis also compares the main attributes of different current and position sensor technologies applicable for this particular system. For a safe and functional vehicle operation, the PMSM must be reliable and efficient. This can only be achieved with accurate sensors which also withstands the harsh environment experienced in vehicle operation.

It is through simulations showed that phase current DC offsets and time delays in the current sensor result in a torque ripple. It was found that the ripple exceeds a constraint of  $\pm 5$  Nm when the offset becomes larger than 3.5 A. The impact of the time delay did not cause the torque to exceed the torque constraint of  $\pm 5$  Nm other than at peak spikes. The ripple in the currents increases significantly for bandwidths below 100 kHz of a LPF representing the time delay. Regarding the impact of position measurement errors, it is shown that the efficiency of the system is reduced. An angle offset error as well as a time delay result in a suboptimal current vector. This is translated into a resistive power loss indicating a significant impact of the measurement errors. It is concluded that the power loss experiences a significant increase above 1 mechanical degree offset and for a bandwidth below 7.5 kHz in the LPF representing time delay.

The comparison of applicable sensor technologies indicates that an AMR current sensor respectively an Inductive Encoder position sensor shows promising attributes. The AMR sensor is small, reliable, cheap and provides galvanic isolation with a wide bandwidth. The resolver is a common position sensor technology used in vehicle application due to its robust and accurate properties. The Inductive Encoder does however possess the properties of the resolver but without many of its disadvantages. This is a relatively new technology which is not widely recognized in the industry. Deeper investigations is therefore recommended to be conducted regarding its applicability in CEVT's dedicated hybrid transmission.

## Keywords:

PMSM, Field Oriented Control, current sensor, position sensor, Impact of measurement errors, sensor technologies comparison.

# Acknowledgements

This master thesis has been carried out at CEVT AB in Gothenburg, Sweden. It has been done with terrific supervision from CEVT and also the Division of Electric Power Engineering in the Department of Electrical Engineering at Chalmers University of Technology (CTH).

We would like to express our gratitude to our examiner Stefan Lundberg (CTH) and our supervisor Tomas Gustafsson at CEVT. We would also like to thank Ehsan Behrouzian (CTH) and Dan Hagstedt (CEVT) for assisting us with matters regarding our simulations.

# List of Acronyms

<b>AMR</b>	- Anisotropic Magnetoresistive
<b>CEVT</b>	- China Euro Vehicle Technology
<b>DHT</b>	- Dedicated Hybrid Transmission
<b>EMF</b>	- Electromotive Force
<b>FOC</b>	- Field Oriented Control
<b>ICE</b>	- Internal Combustion Engine
<b>KCL</b>	- Kirchhoff's Current Law
<b>LPF</b>	- Low Pass Filter
<b>MTPA</b>	- Maximum Torque Per Ampere
<b>MTPV</b>	- Maximum Torque Per Voltage
<b>PCM</b>	- Power Control Module
<b>PLL</b>	- Phase Locked Loop
<b>PMSM</b>	- Permanent Magnet Synchronous Machine
<b>PTP</b>	- Peak to Peak
<b>PI</b>	- Proportional Integral
<b>PID</b>	- Proportional Integral Derivative
<b>PWM</b>	- Pulse Width Modulation
<b>VCO</b>	- Voltage Controlled Oscillator
<b>VR</b>	- Variable Reluctance
<b>WF</b>	- Wound Field

# Contents

<b>1</b>	<b>Introduction</b>	<b>1</b>
1.1	Background . . . . .	1
1.2	Aim . . . . .	2
1.3	Scope and limitations . . . . .	2
1.4	Previous work on PMSM sensor measurement errors . . . . .	4
1.5	Sustainable, social and ethical aspects . . . . .	5
<b>2</b>	<b>The Dedicated Hybrid Transmission system</b>	<b>7</b>
2.1	The permanent magnet synchronous machine . . . . .	8
2.1.1	Synchronous coordinate system transformation . . . . .	8
2.1.2	Dynamic model . . . . .	10
2.1.3	Torque and speed characteristics . . . . .	11
2.1.4	Saliency . . . . .	12
2.2	Control of PMSM . . . . .	12
2.2.1	PI Current controller . . . . .	13
2.2.2	PI speed controller . . . . .	15
2.2.3	Speed estimation through a Phase Locked Loop . . . . .	16
2.2.4	Maximum Torque Per Ampere . . . . .	17
2.2.5	Maximum Torque Per Voltage and Field weakening . . . . .	19
2.3	Bandwidth . . . . .	20
<b>3</b>	<b>Current sensor technologies</b>	<b>21</b>
3.1	Shunt based current sensors . . . . .	21
3.2	The Hall effect utilized for sensor technologies . . . . .	22
3.2.1	Basic strategy of Hall sensor technology . . . . .	22
3.2.2	Hall based current sensors . . . . .	24
3.2.3	Galvanic isolation . . . . .	25
3.3	Rogowski Coil . . . . .	25
3.4	Anisotropic Magnetoresistive current sensors . . . . .	25
3.5	Effect and causes of current measurement errors . . . . .	27
<b>4</b>	<b>Position sensor technologies</b>	<b>29</b>
4.1	Resolver . . . . .	29
4.2	Incremental and Absolute Encoder . . . . .	31
4.3	Optical Encoder . . . . .	31
4.4	Capacitive Encoder . . . . .	32
4.5	Inductive Position Sensor . . . . .	33
4.6	Inductive Encoder . . . . .	33
4.7	Sensorless control . . . . .	34
<b>5</b>	<b>Drive system modelling</b>	<b>35</b>
5.1	PMSM model . . . . .	36

5.2	Field oriented controlled PMSM Simulink implementation . . . . .	39
5.2.1	Implementation of the current controller . . . . .	39
5.2.2	Implementation of the speed controller . . . . .	39
5.2.3	Implementation of MTPA/MTPV . . . . .	40
5.2.4	Phase locked loop . . . . .	40
5.3	Discretization of the simulink model . . . . .	41
5.4	Implementation of sensor measurement errors in Simulink model . . . . .	42
5.4.1	Implementation of a current sensor . . . . .	43
5.4.2	Implementation of position sensor . . . . .	44
5.4.3	Implementation of combined current and position errors. . . . .	44
5.5	Evaluation of applicable sensor technologies . . . . .	45
<b>6</b>	<b>Results</b>	<b>47</b>
6.1	Simulation results of continuous system without errors . . . . .	47
6.2	Continuous system sensor error simulation . . . . .	51
6.2.1	Current sensor errors . . . . .	51
6.2.2	Position sensor error . . . . .	52
6.3	Discrete system measurement error effects . . . . .	55
6.3.1	Current DC offset error effects in the discrete system . . . . .	57
6.3.2	Current sensor time delay effects . . . . .	60
6.3.3	Effect of position angle offset error in the discrete system . . . . .	62
6.3.4	Position sensor time delay effects . . . . .	65
6.3.5	Combined error effects in the discrete system . . . . .	68
6.4	Sensor technologies comparison matrices . . . . .	73
6.4.1	Current sensor technologies comparison . . . . .	73
6.4.2	Position sensor technologies comparison . . . . .	73
<b>7</b>	<b>Discussion</b>	<b>75</b>
7.1	Current sensor simulation . . . . .	75
7.2	Position sensor simulation . . . . .	76
7.3	Combined sensors simulation . . . . .	77
7.4	Applicable current sensor technologies . . . . .	77
7.5	Applicable position sensor technologies . . . . .	78
7.6	Future work . . . . .	80
<b>8</b>	<b>Conclusion</b>	<b>81</b>
	<b>References</b>	<b>4</b>
	<b>Appendices</b>	<b>A.1</b>
	<b>Appendix 1</b>	<b>A.1</b>
	<b>Appendix 2</b>	<b>A.2</b>
	<b>Appendix 3</b>	<b>A.3</b>



# 1

## Introduction

### 1.1 Background

One of the biggest challenges the world faces today is climate change and the reduction of greenhouse gas emission. The vehicles produced today have evolved immensely in terms of quality, safety and especially in reduction of gas emissions especially in the past two decades. Still, road transport accounts for 17% of the global greenhouse gas emissions, making it a major contributor to climate change [1]. The efforts of further reductions of carbon emissions are thus crucial during development of the vehicles of tomorrow. Especially in order to achieve the goal of the Paris Agreement which is to keep the global average temperature as close as possible to 1.5°C above pre-industrial levels [1]. The high demand in reduction of greenhouse gas emission is pushing the automotive industry towards electrification of vehicles [2]. The reason for this can be understood by examining a traditional combustion engine. It has around 30% efficiency where the rest of the energy is being wasted [3], whereas an electric motor can have an efficiency above 90% [4]. It is therefore only logical that the automotive industry seeks to produce more efficient vehicles that both satisfies consumer needs and are environmental friendly.

The Geely holding group is a global automotive group currently advancing further and further as one of the leaders in the electric and hybrid vehicle industry [5]. The company established the R&D centre China Euro Vehicle Technology AB (CEVT) in Gothenburg in 2013 which is developing automotive technology that meet the demands of future global markets [5].

Hybrid vehicles are seen as a step towards reducing the greenhouse gas emissions and the vehicles' negative effect on the environment. One of the ongoing automotive technologies currently being developed at CEVT is a transmission system for hybrid electric vehicles. This system is referred to as Dedicated Hybrid Transmission (DHT) and consists of two Permanent Magnet Synchronous Machines (PMSM) working together with an Internal Combustion Engine (ICE). One of the machines is primarily used as a generator and for starting the ICE, whereas the other electrical machine is used primarily for propulsion of the vehicle able to cooperate with the ICE. The combination of these motors operations depend on the driving conditions as this is what sets the reference for both speed and torque. A Power Control Module (PCM) in the system controls the torque demand and provides appropriate amount of power to each unit in the system. In order to optimize the efficiency of the power distribution, the PCM relies on accurate inputs from several sensors.

For a safe and efficient operation of the DHT, accurate sensor measurements are required. Specifically, the current sensors measuring the PMSM stator current and the position sensor measuring the rotor angle are both necessary components for the control of the PMSM. In regards to the DHT project at CEVT, it is known that the specifications of these sensors are of importance in a well functioning vehicle. Before setting the specifications however, the sensor properties and the effects of inaccurate measurements shall be understood. Thus a developed understanding of how quality can be improved and cost of the sensors possibly can be reduced is needed. By improving quality and reducing cost, a more efficient and environmentally friendly vehicle that is also more affordable can be produced.

## **1.2 Aim**

This thesis aims to evaluate the impact of measurement errors from the stator current sensors and the rotor position sensor on a PMSM drive system. The thesis also aims to deliver knowledge on applicable sensor technologies. It also compares different current and position sensor technologies in regards to performance and cost while keeping ethical and environmental aspects in mind. After such investigation has been conducted, a recommendation of a most suitable sensor technology for the DHT is suggested to CEVT.

## **1.3 Scope and limitations**

This report presents the master thesis project carried out at the company CEVT with supervision from the department of Electrical Engineering at Chalmers University of Technology. As the thesis is carried out at CEVT, this puts some predefined limitations and restrictions on the thesis scope. Well defined areas of focus but also limitations must be established. This is to ensure that the intended time schedule for the project is followed and also respect the company's desired goals of the project. The following list presents the scope and limitations for this thesis:

- Errors found in current and position sensor technologies will be investigated through simulations and an extensive literature study.
- Since CEVT is using PMSM's in their DHT project, this will be the machine type which the sensors will be investigated for. The DHT consists of two PMSM's but due to their similarities and time constraints, only the traction PMSM will be modelled. This is chosen because it is considered to show biggest effect of the sensor errors due to its higher power capability.
- In vehicle operation, the PMSM operates in a variety of operating points. To take all these into consideration complicates the sensor specification and would be too time consuming. Because of this, the thesis is limited to only evaluate errors at normal operation of the

PMSM.

- The power losses caused by sensor measurement errors will be investigated in order to better understand their significance. The goal is to minimize power losses and thus increase efficiency, allowing CEVT to build a more environmental friendly vehicle.
- Sensorless control is a control method where the rotor flux angle is estimated. However, the proposed project from CEVT was to investigate and evaluate sensor errors. This implies that CEVT intends to use a sensor controlled system, thus an investigation in sensorless control will not be extensive. This technology could however be presented as a suggestion for CEVT to look into for future projects.
- The simulation model of the PMSM does not consider nonlinear inductances. The inductance of the machine is instead a constant value. This is because a nonlinear system is complex and time consuming to model while it is considered to have a little impact of simulated sensor errors.
- The simulation model of the system does not include a battery model. The system voltage is therefore fed with an ideal DC source.
- Since both current and position sensors measurement errors are investigated, the test matrices quickly grow large. Thorough model of specific sensors are not modelled, instead specific sensor errors found in several sensor technologies are modelled.
- The attributes of a particular sensor depend on several factors such as different manufacturers or the operation of the rest of the system. Because of this, only main attributes of the investigated sensor technologies are compared and presented.
- It is possible to model more advanced control systems which can compensate for certain measurement errors. This thesis does not investigate different control algorithms that can be used to mitigate the effect of error measurements.
- The number of simulations of different error combinations is limited. This is because there are countless possible combinations of error parameter value combinations. In order to still present comprehensive results, parametric sweeps of the error parameters are conducted. These sweeps starts from error values resulting in negligible effects and grow until unacceptable effects on the system is observed.
- The specified torque constraint at CEVT is a continuous ripple no larger than  $\pm 5$  Nm and maximum peaks of  $\pm 10$  Nm. Regarding the current measurements, it is specified in the DHT project that the sensors should be able to measure currents up to 500 A. The acceptable accuracy of this measurement is 1% meaning  $\pm 5$  A. These specifications are seen as a reference value to compare with while performing parametric sweeps of measurement error parameters.

- Most type of sensor errors can be combined resulting in a total offset error which decides the accuracy. An error source which cannot be combined and does not decide the accuracy, is time delay. Therefore this thesis focuses on evaluation of offset errors and time delays in both the current and position sensors.

#### **1.4 Previous work on PMSM sensor measurement errors**

During the extensive literature study conducted throughout the thesis, several projects on this subject were found and analyzed. The authors of [6] and [7] presents a thorough investigation of rotor position sensors for measurements on a PMSM. Both reports highlights the resolver as the industry standard position sensor but also presents Hall effect sensors and inductive sensors as viable options. It is also in these sources presented that the current vector is suboptimal due to a position error which reduces the efficiency of the entire system.

Regarding current sensors it was found in [8] and [9] that errors in the measurements result in ripples in both the currents and the torque. The authors present several possible sensor technologies but both concludes that both Hall effect sensors as well as magnetoresistive sensors are promising technologies. However, other investigations such as [10] argues that shunt based current sensors are superior to magnetic field sensors.

Finding exceedingly amounts of sources with related work led to the realization that the challenge of this particular thesis is the investigation of both current and position sensors simultaneously. The related work generally looks at the effect of one specific type of sensor technology which reduces the complexity. In this thesis the combined effect of position and current measurement errors is examined and thus considered as the main challenge.

## 1.5 Sustainable, social and ethical aspects

The automotive industry constantly deal with difficult sustainable, social and ethical questions. This industry is a big contributor of green house gases and consequently moving towards more efficient and environmentally friendly vehicles. Inaccurate sensor measurements can result in increased power losses in the system. The wasted energy becomes significant in at large scale which is not sustainable for the environment as it increases energy consumption. Accurate readings are thus an important property of a sustainable system. An efficient system also adds to the driving range of the vehicle which adds value to the user experience. Regarding the choice of sensor, not only accuracy affects the sustainability. Properties such as size, power consumption of required electronics and maintainability also effects the efficiency of the system as a whole.

Another developing area within the vehicle industry is safety. It is of paramount importance to increase the safety of the vehicle and reduce the number of accidents. It is therefore important to choose a highly reliable sensor technology which is robust enough to handle the environment in which it is placed. Regarding current measurements of PMSMs as investigated in this thesis, only two currents are required to be measured as the third can be calculated. This means that only two sensors would be sufficient which would reduce cost, size and power consumption of the required electronics. However, in the automotive industry all three phases are usually measured for safety reasons by failure detection as safety is prioritized. A sum of the three phases that does not add up to zero indicates a that there is an error in the measured currents.

The cost of the sensor however also has to be considered, if too expensive it could lead to an increased price of the vehicle. This can result in customers being less prone to purchase this specific vehicle unless other benefits outweigh this downside. The cost of the sensors in a vehicle is however small in comparison to the total price of the vehicle. Thus the cost of a sensor should be compared to cost of the whole system when considering the significance of the added benefits of choosing a more expensive sensor.



# 2

## The Dedicated Hybrid Transmission system

The DHT investigated in this thesis is powered by three machines, one ICE and two PMSMs. One of the PMSMs is mainly used as a generator provided with torque from the ICE or regenerative braking while the other PMSM is used as a traction motor. The traction motor can work together with the ICE in order to maximize torque or find a more efficient operating point of both motors. All of the machines are controlled with the intent to optimize the efficiency of the system. This is achieved by letting the motors operate together in different combinations based on the torque and speed demand from the particular driving scenario. This can for example be solely ICE operation while the PMSMs are idle, or combined traction torque produced by the ICE and traction PMSM. A simple version of the system intended to illustrate the basic principle with block components for the motors, battery and transmission is presented in Figure 1. The main components of the DHT system relevant to this thesis and the theoretical background which these components are based on will be further described in the following chapters.

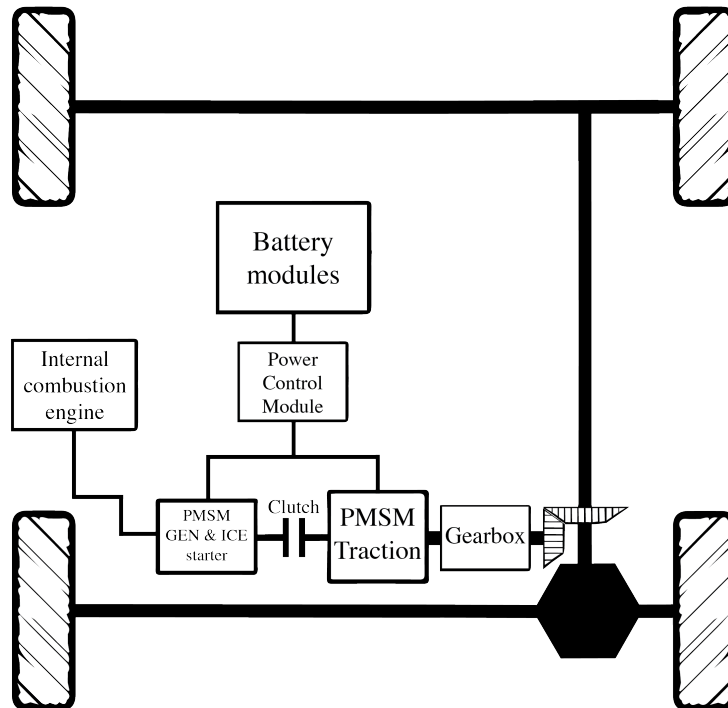


Figure 1: Simple version of the whole DHT system with two PMSMs.

## 2.1 The permanent magnet synchronous machine

The PMSM has during recent years grown rapidly in its usage, especially when it comes to its application in electric and hybrid vehicles [11]. These machines can deliver higher torque and have a higher efficiency of up to above 97% compared to similar types of motors of the same size [12],[4]. As the name implies the magnetization is produced by permanent magnets mounted inside or on the surface of the rotor. A simple version of a single pole pair PMSM with inset mounted magnets is presented in Figure 2. Usage of permanent magnets means that the rotor weight can be reduced as there is no need for rotor windings [4].

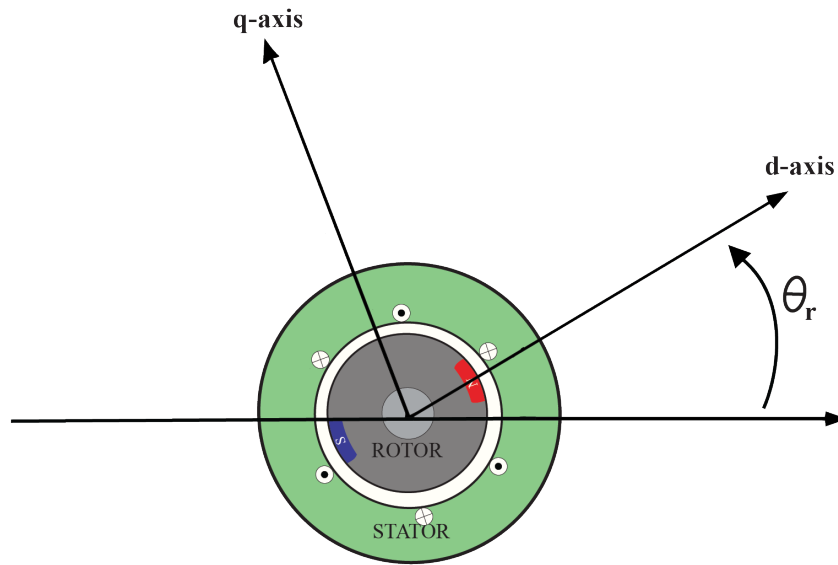


Figure 2: A simple cross section of a PMSM where the d-axis is oriented in the direction of the magnetic flux.

Field Oriented Control (FOC) is a method used to control a PMSM by transforming the AC signals into DC signals using a synchronous rotating coordinate system with the knowledge of the orientation of the magnetic flux [13]. This chapter will cover the theory behind necessary tools and knowledge used for controlling a PMSM.

### 2.1.1 Synchronous coordinate system transformation

A three-phase system, assuming there is no zero-sequence, can be described as

$$\begin{aligned} u_a &= V \cos(\omega t + \phi) \\ u_b &= V \cos(\omega t + \phi - \frac{2\pi}{3}) \\ u_c &= V \cos(\omega t + \phi - \frac{4\pi}{3}) \\ u_a + u_b + u_c &= 0, \end{aligned} \tag{1}$$

Where  $u_a, u_b, u_c$  are the phase voltages where  $V$  represents the voltage amplitude,  $\omega$  represents the electrical frequency,  $t$  represents time and  $\phi$  represents an angle offset. In a case with no zero-sequence, no information is lost when transforming the three-phase system into a two-phase system. This transformation is performed by usage of what is known as Clarke's transformation [13]. This transformation is expressed as

$$\begin{bmatrix} u_\alpha \\ u_\beta \end{bmatrix} = \frac{2K}{3} \begin{bmatrix} 1 & -\frac{1}{2} & -\frac{1}{2} \\ 0 & \frac{\sqrt{3}}{2} & -\frac{\sqrt{3}}{2} \end{bmatrix} \begin{bmatrix} u_a \\ u_b \\ u_c \end{bmatrix}. \quad (2)$$

Here the quantities  $u_{a,b,c}$  are three sinusoidal voltage signals 120° apart. The transformation yields two sinusoidal varying vectors  $u_{\alpha,\beta}$ . The scaling constant  $K$  can be selected arbitrarily depending on the desired quantity; commonly picked values are 1,  $\frac{1}{\sqrt{2}}$  or  $\sqrt{\frac{3}{2}}$  which corresponds to amplitude invariant scaling, RMS-value scaling, or power-invariant scaling. To make the implementation of control algorithms easier, a further step is taken by transforming these two sinusoidal quantities into constant DC signals by introducing a rotating reference frame which rotates at synchronous speed. This transformation is known as Park's transformation, or dq-transformation [13]. The transformation is expressed as

$$\begin{bmatrix} u_d \\ u_q \end{bmatrix} = \begin{bmatrix} \cos\theta & \sin\theta \\ -\sin\theta & \cos\theta \end{bmatrix} \begin{bmatrix} u_\alpha \\ u_\beta \end{bmatrix}. \quad (3)$$

In the dq-system, the d-axis is oriented in the direction of the rotor flux  $\psi_r$  which rotates at synchronous speed with the angle  $\theta$  relative to the stationary reference frame

$$\theta = \arctan \frac{\psi_{r\beta}}{\psi_{r\alpha}}. \quad (4)$$

Thus, a rotating coordinate system at synchronous speed is created. Using the dq-system, the signals are now DC-signals which are easier to use in control algorithms, rather than controlling the system with AC-signals. A visual representation of the transformation from a stationary three phase to a synchronous rotating coordinate system is presented in Figure 3.

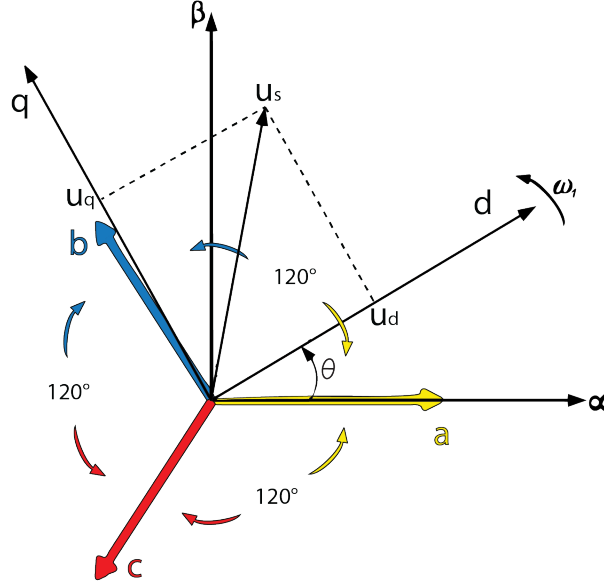


Figure 3: Stationary three phase to stationary two phase to rotating two phase reference frame presented in a vector diagram.

### 2.1.2 Dynamic model

The dynamic model of the PMSM can be expressed in the dq-coordinate system. The stator voltage is with this strategy divided into a d-component  $u_{sd}$  and a q-component  $u_{sq}$  as [13]

$$u_{sd} = \underbrace{R_s i_{sd}}_a + \underbrace{L_{sd} \frac{di_{sd}}{dt}}_b - \underbrace{\omega_r L_{sq} i_{sq}}_c \quad (5)$$

$$u_{sq} = \underbrace{R_s i_{sq}}_a + \underbrace{L_{sq} \frac{di_{sq}}{dt}}_b + \underbrace{\omega_r L_{sd} i_{sd}}_c + \underbrace{\omega_r \psi_m}_d \quad (6)$$

In these equations, the stator current  $i_s$  and stator voltage  $u_s$  is divided into d- and q-components.  $R_s$  represents the resistance in the stator windings,  $L_s$  is the stator inductance from the d- and q-component separately,  $\psi_m$  is the magnetic flux and  $\omega_r$  is the electrical rotor speed. The different terms of the equations represent a change in potential due to different physical phenomenas in the motor. The term denoted as "a" is the resistive voltage drop in the stator windings, "b" is the voltage needed to change the current since the machine has inductive properties, "c" is a cross coupling term, and "d" represents the back Electromotive Force (EMF). These parameters are schematically presented in Figure 4 which describes the dynamic model in both d- and q-axis.

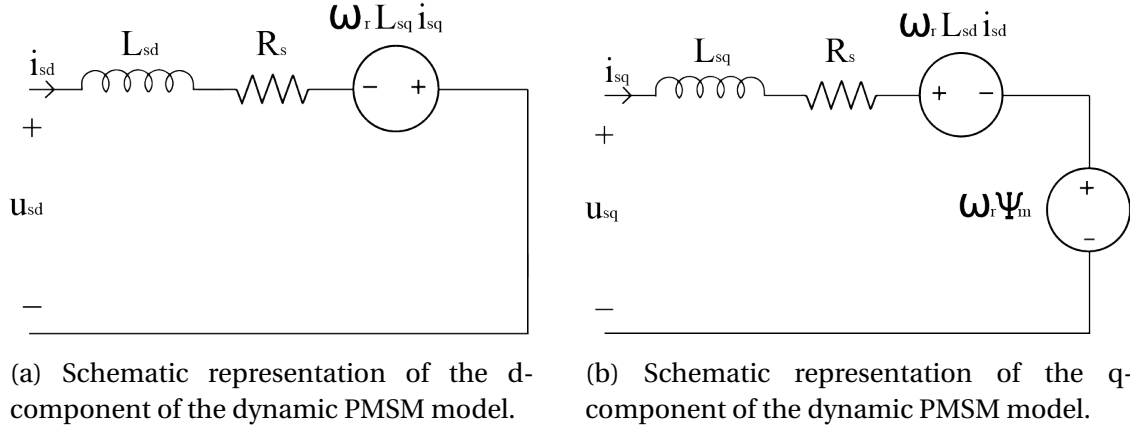


Figure 4: Schematic representation of the dynamic PMSM model.

### 2.1.3 Torque and speed characteristics

The electrodynamic torque produced by the PMSM can be calculated as

$$T_e = \frac{P_e}{\Omega_r} = \frac{n_p P_e}{\omega_r} = \frac{3}{2K^2} n_p [\Psi_r + (L_d - L_q) i_d] i_q, \quad (7)$$

where  $P_e$  is the electric power consumed in the voltage sources in Figure 4,  $\Omega_r$  is mechanical speed and  $n_p$  is the number of pole pairs [14]. For amplitude invariant scaling,  $K$  is equal to 1. The relationship between the electrical and mechanical rotor speed is expressed as

$$\Omega_r = \frac{\omega_r}{n_p} \quad (8)$$

The mechanical equation governing the motion of the rotor is known as the swing equation and can be expressed as

$$\frac{J}{n_p} \frac{d\omega_r}{dt} = T_e - T_{load} - B\Omega_r, \quad (9)$$

where  $J$  is the total moment of inertia of the rotor mass and  $B$  is the viscous friction constant [15]. A visual representation of how the torque acts on a body mass can be seen in Figure 5.

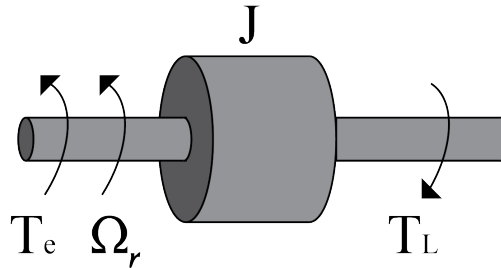


Figure 5: Visualization of torque mechanics

The output power for an electric machine can be calculated from the torque and angular speed as

$$P = T_e \cdot \Omega_r = T_e \cdot \frac{\omega_r}{n_p} \quad (10)$$

while the resistive power loss, due to solely applied current to the stator, can be calculated as

$$P_{loss} = \frac{3}{2K} |I_s|^2 R_s. \quad (11)$$

### 2.1.4 Saliency

As described in Section 2.1 the permanent magnets can be mounted inside or on the surface of a PMSM. In Figure 6 surface mounted magnets are displayed to the left while inset mounted magnets are displayed to the right. The magnets can also be interior mounted meaning mounted completely inside the rotor. The difference of mounting the magnets inside or on the surface of the rotor corresponds to a difference in the airgap. The magnets have approximately the same permeability as the surrounding air and can be viewed as an extension of the airgap in the d-direction when mounted inside the rotor. These machines are referred to as salient and have a non-uniform airgap which impacts the inductance. As the q-axis and d-axis have different inductance this results in a torque increase usually referred to as reluctance torque. Due to the difference in airgap length the mutual inductance is maximal at the poles and minimal in between as the mutual inductance is inversely proportional to the width of the air gap [13].

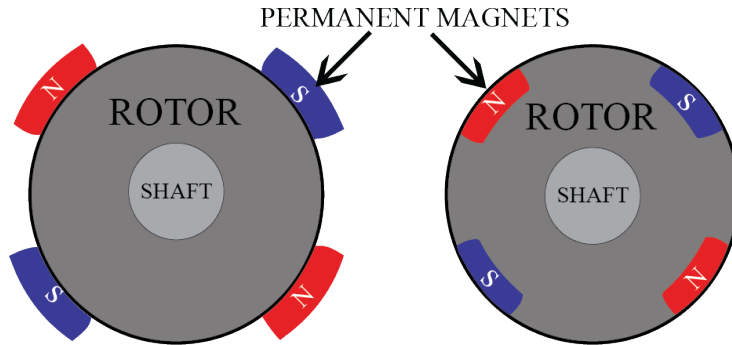


Figure 6: Non-salient PMSM to the left and a salient PMSM to the right.

## 2.2 Control of PMSM

A popular approach of controlling a PMSM is to base it on the magnetic field produced by the machine and this is typically known as Field Oriented Control (FOC). Here the Park and Clarke transformation, presented in Section 2.1.1, are used both as forward and reverse transformation in the control algorithm. The strategy of FOC is to utilize synchronous coordinates and place

the d-axis in the direction of the rotor flux [16]. A current and speed controller can be utilized in the system in order to reach and maintain the requested torque and speed as well as calculate the most efficient magnitudes of  $i_d$  and  $i_q$  currents. The reference value of the input currents to the current controller are decided through a Maximum Torque Per Ampere (MTPA) calculation further explained in 2.2.4. A block diagram of the control system for the PMSM can be seen in Figure 7 and the different controller blocks will be further explained in the following chapters.

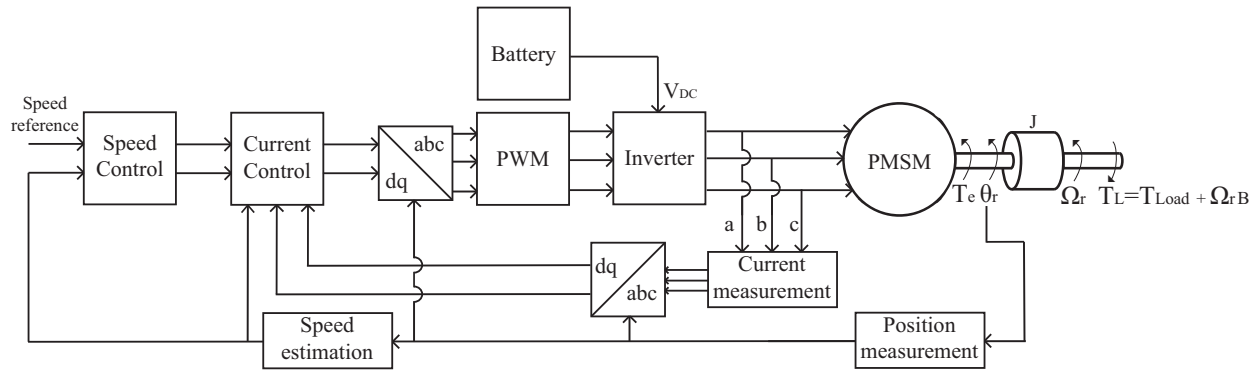


Figure 7: Block diagram of the PMSM control system.

### 2.2.1 PI Current controller

The control system which utilizes FOC attempts to regulate the current such that the current follows its reference value. This can be achieved by utilization of a Proportional-Integral (PI) controller which is widely used for PMSMs due to its simplicity [17]. Another alternative is to use a Proportional-Integral-Derivative (PID) controller. The derivative part can however have a negative impact on the system as it amplifies high frequencies. The input to the controller are measured quantities which always contains noise and will never be entirely accurate. This noise and other high frequency disturbances in the input signals will be amplified by the derivative part. A PI-controller is therefore the preferred choice. The controller has the d- and q-axis currents as input signals and calculates the corresponding  $u_{dq}$  voltages as its output [18].

The PMSM plant system transfer function is derived from rewriting the voltage equations (5) and (6) to expressions for the currents as

$$\begin{aligned}
 i_{sd} &= \frac{1}{L_{sd}s + R_s + R_{ad}} u_{sd} = G_{Cd}(s) u_{sd} \\
 i_{sq} &= \frac{1}{L_{sq}s + R_s + R_{aq}} u_{sq} = G_{Cq}(s) u_{sq} \quad .
 \end{aligned}
 \tag{12}$$

As the name PI-controller implies, the controller consists of a proportional gain and an integrator part. Its transfer function is expressed as [13]

$$F_e(s) = K_P + \frac{K_I}{s} \quad (13)$$

where  $K_P$  is the proportional gain and  $K_I$  is the integrator gain. These parameters are chosen such that the closed loop system becomes a first order low pass filter (LPF) with an amplification of 1 and the bandwidth  $\alpha_c$  [13]. The parameters are consequently chosen as [13]

$$\begin{aligned} K_{Pcc} &= \alpha_c L \\ K_{Icc} &= \alpha_c (R_s + R_a) . \end{aligned} \quad (14)$$

where  $R_a$  is a fictional resistance known as active damping. This added resistance reduces the control error. The selection of this parameter is done such that the inner feedback loop is as fast as the closed loop system [13]. This means that [13]

$$R_a = \alpha_c L - R_s \quad (15)$$

which yields

$$\begin{aligned} K_P &= \alpha_c L \\ K_I &= \alpha_c^2 L . \end{aligned} \quad (16)$$

Another addition to the regulator is to feed forward the back-EMF term denoted as "d" in (6) for the q-component as it is regarded as a disturbance entering the process [13]. Another term added to both d- and q-component is the cross-coupling term denoted as "c"

$$\begin{aligned} v_{d,add} &= -\omega_r L_{sq} i_{sq} \\ v_{q,add} &= \omega_r \Psi_m + \omega_r L_{sd} i_{sd} . \end{aligned} \quad (17)$$

In addition, anti-windup can be added to the system. This is presented in Figure 8 which also shows the active damping and feed forward of back EMF in the system. The anti-windup term removes the overshoot caused by integrator windup [13].

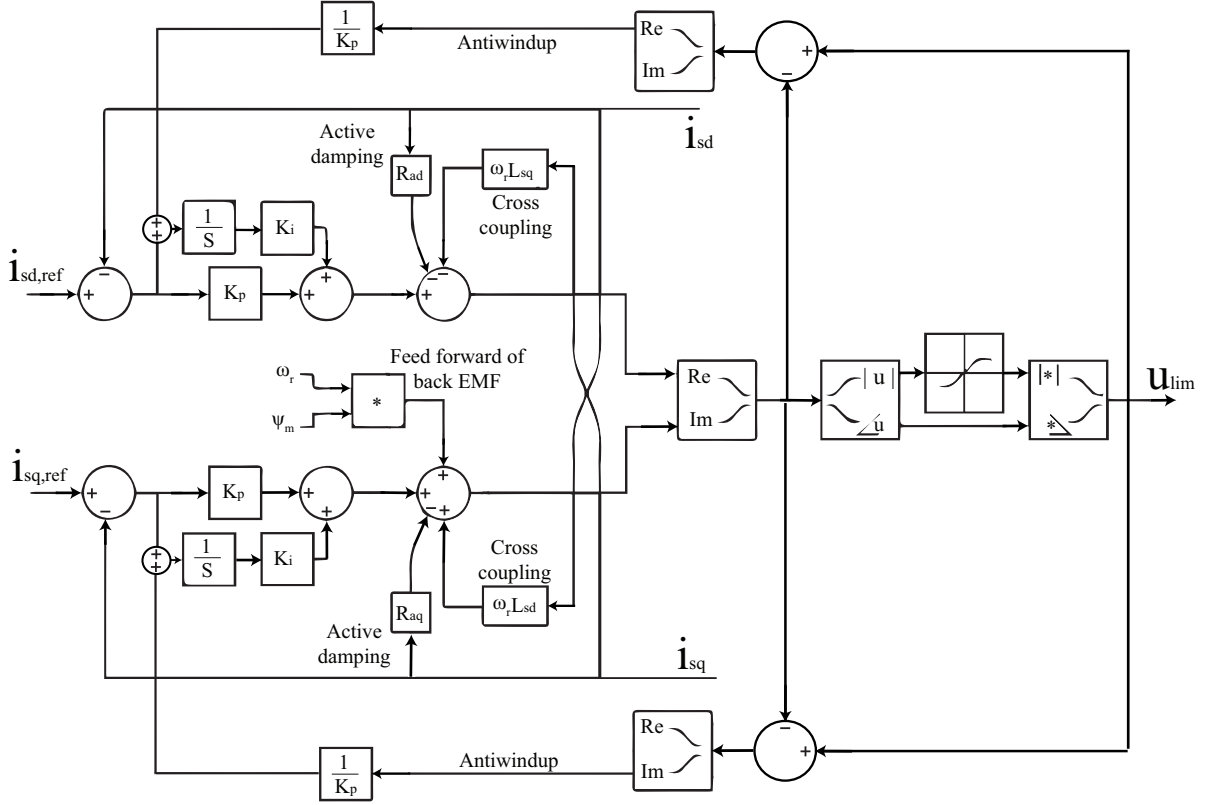


Figure 8: Illustration of the complete current controller.

The figure illustrates a complete continuous controller. However, in order to make this system more realistic, it is discretized. The equations is consequently rewritten for discrete systems and calculates the output voltage references according to [19]

$$\begin{aligned}
 v_d^{ref} &= (K_{p\_id} + K_{i\_id} \frac{T_s Z}{z-1})(i_d^{ref} - i_d) + v_{d,add} \\
 v_q^{ref} &= (K_{p\_iq} + K_{i\_iq} \frac{T_s Z}{z-1})(i_q^{ref} - i_q) + v_{q,add} .
 \end{aligned}
 \tag{18}$$

For the discretized system it is of high importance to consider the switching frequency when deciding the controller bandwidth  $\alpha_c$ . This is further discussed in Section 2.3.

## 2.2.2 PI speed controller

Similar to a current controller as described in Section 2.2.1, a speed controller can be implemented to the system. This controller is usually used together with a current controller and seen as the outer loop in the control system. The controller takes the desired reference speed as input and compares it with the actual speed of the machine. The output of the speed controller

is a torque reference which with a MTPA calculation provides a current controller with its reference currents. These are recalculated to reference voltages which results in an accelerating or decelerating machine. These three controller blocks working together is visualized in Figure 9 where  $\omega_e$  represents the real speed of the PMSM.

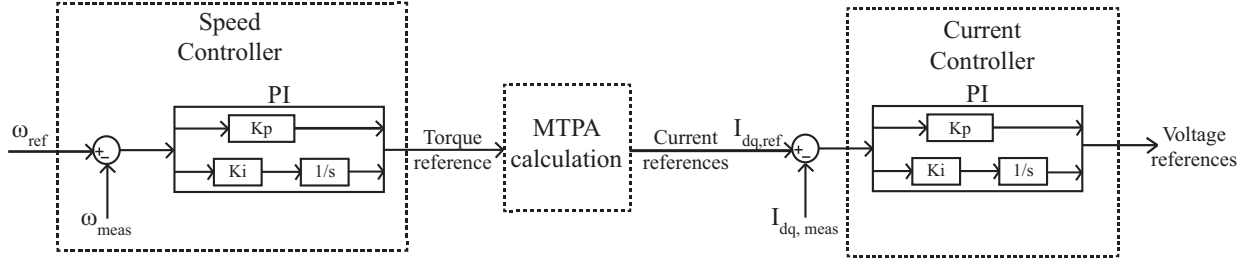


Figure 9: Controller loop block diagram.

Similar to the current controller in Section 2.2.1 the speed controller includes active damping and anti-windup. Its control parameters are chosen as [13]

$$\begin{aligned}
 B_a &= \alpha_w \cdot J - B \\
 K_{Pw} &= \alpha_w \cdot J \\
 K_{Iw} &= J \cdot \alpha_w^2 \quad .
 \end{aligned} \tag{19}$$

### 2.2.3 Speed estimation through a Phase Locked Loop

In order to obtain information of the mechanical speed of the machine, one could simply measure the position and take the derivative of the rotor angle. However, if the position sensor output contains inaccurate measurements with high frequency noise, this strategy does not work. This is because the high frequency noise will contribute to large derivatives which will result in incorrect speed readings.

Another strategy for obtaining the speed must therefore be used. One method of estimating the speed is to use the measured angle as an input signal to what is known as a Phase Locked Loop (PLL). This can be seen as a three parted block diagram which is used for automatic frequency control [20]. These three parts are the initial phase detector followed by a Low Pass Filter (LPF) which ends in a feedback to the phase detector through a voltage controlled oscillator (VCO). These three parts are visualized in Figure 10.

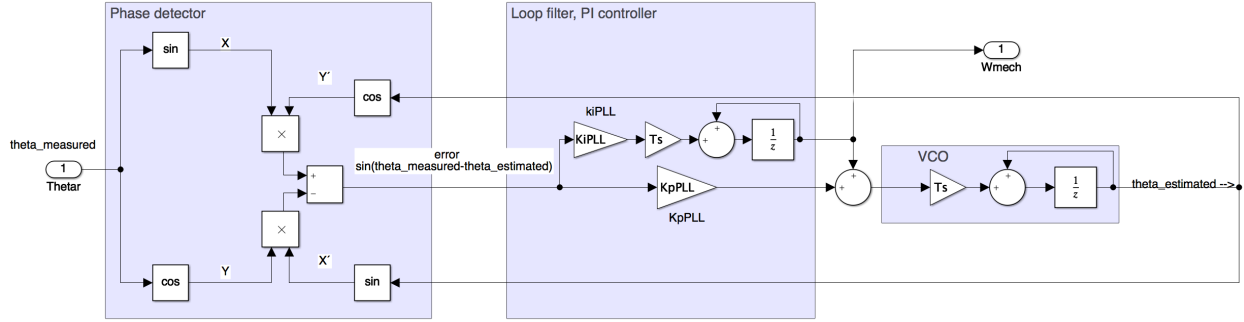


Figure 10: A Simulink model of the PLL.

The basic strategy of a PLL is to make sure that both input signals to the phase detectors have equal frequency and to bring the error in the estimated angle to zero [20]. The gain and integral control parameters are chosen as [13]

$$\begin{aligned} K_{I_{PLL}} &= \alpha_{PLL}^2 \\ K_{P_{PLL}} &= 2 \cdot \alpha_{PLL} \end{aligned} \quad (20)$$

where  $\alpha_{PLL}$  is the bandwidth of the PLL.

#### 2.2.4 Maximum Torque Per Ampere

According to (7), a combination of  $i_d$  and  $i_q$  currents produces a specific torque. For a salient PMSM, see Section 2.1.4, the equation is divided into a magnetic and a reluctance torque according to [14]

$$T_{magnetic} = \frac{3}{2K^2} n_p \Psi_r i_q \quad (21)$$

$$T_{reluctance} = \frac{3}{2K^2} n_p (L_d - L_q) i_d i_q \quad (22)$$

As described in Section 2.1.4,  $L_d$  is smaller than  $L_q$  in salient machines. According to (21) and (22), negative d-axis current must thus be applied in order to produce positive torque. The torque is consequently specified by the current vector and especially the current vector angle which specifies the d- and q-axis current magnitudes. It is from this fact the commonly known MTPA current has its origin. It is with other words the minimum current vector necessary to produce a specific torque. This is directly related to the entire copper loss of the machine as the rotor in a PMSM does not contain any windings. This means that the copper losses only depend on the magnitude of the stator current vector according to (11). Furthermore, the iron

losses of a PMSM is negligible at low speeds but it is in reality also slightly affected by the current angle. These facts added together yields the conclusion that operating at MTPA results in optimal efficiency [14].

The MTPA currents in their synchronous reference plane can be expressed as

$$\begin{aligned} i_{sd|MTPA} &= I_S \cdot \cos(\beta_{MTPA}) \\ i_{sq|MTPA} &= I_S \cdot \sin(\beta_{MTPA}), \end{aligned} \quad (23)$$

where  $\beta_{MTPA}$  is the optimal angle between  $i_d$  and  $i_q$ . The MTPA operating point for a constant torque line is that of which the current vector is closest to its origin in the dq-current plane. In other words, the shortest possible current vector from origo that reaches the torque line. This means that the differentiation of torque with respect to current angle is zero for the MTPA point. This can be expressed as [14]

$$\frac{dT_e}{d\beta} = \frac{3n_p}{2} (\Psi_m I_S \cos(\beta) + (L_{sd} - L_{sq}) I_S^2 \cos(2\beta)) = 0 \quad (24)$$

and the  $\beta$ -angle can consequently be expressed as [14]

$$\beta_{MTPA} = \cos^{-1} \left( \frac{-\Psi_m}{4(L_{sd} - L_{sq}) I_S} - \sqrt{\frac{1}{2} + \left( \frac{\Psi_m}{4(L_{sd} - L_{sq}) I_S} \right)^2} \right). \quad (25)$$

This is visualized in Figure 11 where the torque increases with the speed according to (9). It can be observed that the torque follows the black dashed MTPA curve. Eventually the speed has increased to a point, denoted as "a" in the figure, where the voltage contribution from back-EMF has become too large. In order to allow further increase of the speed, it is required that the flux decreases which counteracts the back-EMF contribution. This is referred to as field weakening and further discussed in the following section.

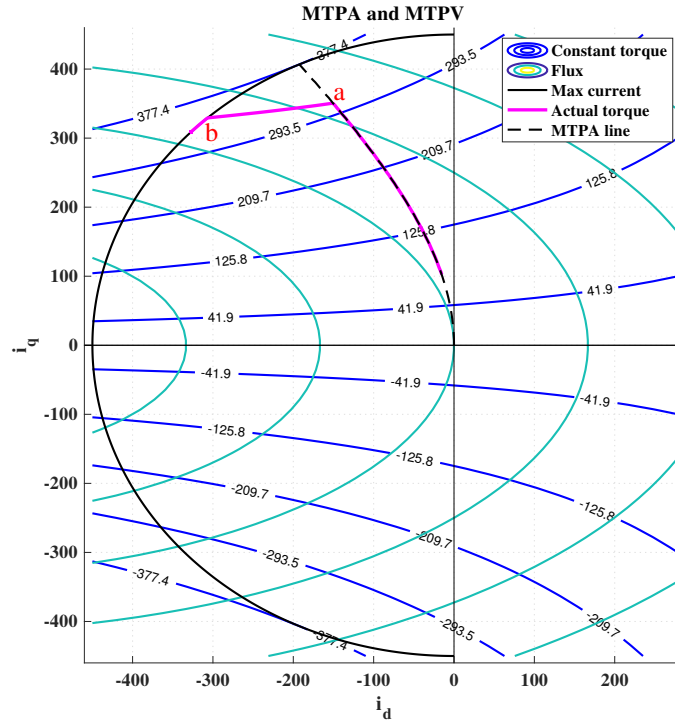


Figure 11: Visualization of MTPA operation. Increasing speed and resulting optimal currents.

### 2.2.5 Maximum Torque Per Voltage and Field weakening

The voltage in the PMSM can be expressed as described in (5) and (6). A particular important part of these equations is the voltage contribution from back EMF denoted as "d" in (6). It can be observed that this voltage contribution is dependent on the speed and the flux. As this back EMF term increases it causes overvoltages at high speeds which limits the PMSM. In order to allow higher speeds, a strategy known as field weakening or Maximum Torque Per Voltage (MTPV) is utilized [21]. Field weakening means that the contribution from back EMF is reduced by applying a negative d-axis current which reduces the flux and thus allows higher speeds. This is visualized in Figure 11 between the denoted point "a" and "b". Once the speed has increased to the level of which the voltage is maximized due to back EMF, increased negative d-current is applied. As a result, the speed can continue to increase. Eventually the point denoted as "b" is reached where the current has reached its maximum. Further negative d-current is needed in order to reach higher speeds but as this increases the current vector while maximum current already is applied, the q-current will have to decrease which in turn will reduce the torque.

Another way of visualizing this for a PMSM is presented in Figure 12. It can be observed that the blue voltage curve increases with the increasing speed while the torque is kept constant. Once the voltage has reached its maximum, negative d-current is applied and field weakening starts in order to allow further increase of the speed. As previously explained this reduces the q-current which in turn reduces the torque. During this time the power is kept constant as the

voltage and current is constant. This is because the q-current is reduced as much as the increased negative d-current and the voltage contribution from back EMF is as big as the reduced voltage due to negative d-current. This area is consequently usually referred to as the constant power area [7].

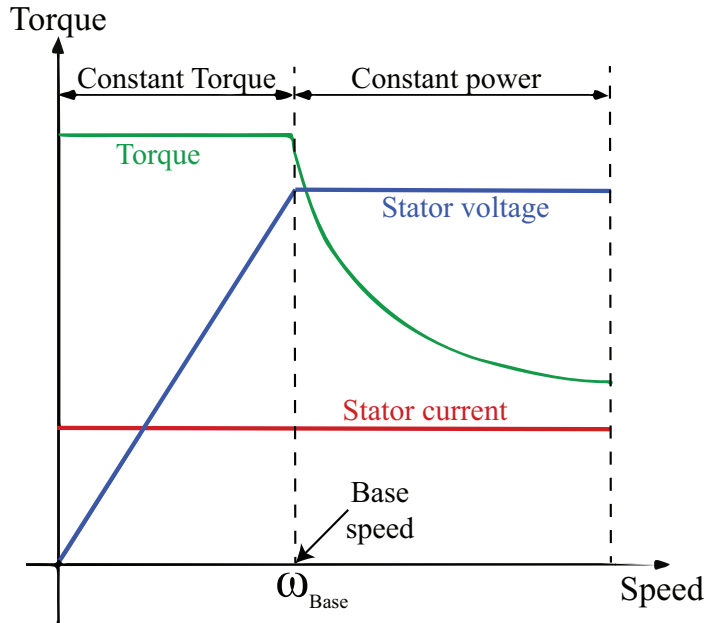


Figure 12: Torque and speed in relation to power for a PMSM.

## 2.3 Bandwidth

Regarding the current and speed controller as well as the PLL, the bandwidth is of high importance. Since the speed controller is seen as the outer control part in the control loop, the current controller should be much faster than the speed controller. In other words, the bandwidth of the speed controller should be chosen such that it is much lower than the current controller. Additionally the PLL has to be much faster than the speed controller since the speed controller relies on inputs from the PLL.

For a discrete system, the switching frequency of the converter has to be considered when deciding controller bandwidths. The controller has to be slower than the converter so that it updates the signals quicker than the controller regulates them.

The current controller is fed currents measured by a current sensor and the PLL is fed the position measured by a position sensor. The bandwidth of these sensors are also of importance and need to be considered. The sensors have to be faster than the controller as it needs to feed updated input signals quicker than the controllers tries to regulate them.

# 3

## Current sensor technologies

Current measuring in electrical machine operation is a challenging task regarding construction of precise control systems. This is because it requires understanding of both the system hardware as well as the system control software [22]. The theory behind a particular sensing technology have to be analyzed together with the control system commands and the rest of the system containing components such as PWM and A/D conversions [22]. For AC three phase measurements all three phases can be measured. It is also possible to use Kirchhoff's current law (KCL) and only measure two phases as the third can be calculated. This is however not common for automotive applications since KCL of all three currents is used for failure detection. Summation of three phase currents that does not result in zero indicates errors in the measured currents.

The main strategies used for current measurements are based on Ohm's and Faraday's law as well as Faraday's Effect and magnetic fields. Among these, most technologies can be categorized as resistive or electromagnetic based [9]. This section will present the working principle of the most common current sensor technologies used for automotive applications.

### 3.1 Shunt based current sensors

Shunt based current sensors are resistive sensors widely used because of their simplicity and high reliability reaching accuracies up to 0.2% [9]. The work by amplifying the voltage drop which is proportional to the current flowing through the shunt. With other words they are based on Ohm's law according to

$$J = \sigma E . \tag{26}$$

The current density is represented by  $J$  while  $\sigma$  is the material conductivity and  $E$  is the electric field. Shunt resistors are commonly placed in the current path and the voltage drop over the resistor is proportional to the current flow. These sensors can be used to measure both AC and DC currents, however as the device is introduced in the path of the current these sensors causes significant power losses [9]. These are resistive power losses calculated as (11). This means that these sensors do not provide galvanic isolation, see Section 3.2.3, and the corresponding power loss are their mayor drawback for high current applications. Isolation can be added by introducing isolation amplifiers but these are usually expensive [9].

The equivalent circuit of a shunt based current sensor can be represented by three simple circuit components. A parasitic inductance representing the mutual inductance between the main current and sensing wires, a resistor representing the nominal resistance as well as a resistor

representing the skin effect [9]. The bandwidth of these current sensors is determined by the parasitic inductance or at large currents, the skin effect. As previously stated shunt current sensors provide no galvanic isolation which means that their temperature dependency, especially at the mounting connection, is a considerable drawback [9].

### 3.2 The Hall effect utilized for sensor technologies

When a current flows through a conductor in the presence of a magnetic field, a force acts on the conducting wire. If the charge of the mobile charges are denoted as  $q$  and their velocity as  $\vec{v}$  the acting force can be described as

$$\vec{F} = q(\vec{E} + \vec{v} \times \vec{B}) \quad (27)$$

where  $\vec{E}$  and  $\vec{B}$  denotes the electric and magnetic field vectors [23]. The acting force is commonly known as the Lorentz force and it is the foundation on which Hall sensor technologies are based on. As the force acts on the conducting wire the current distribution is disrupted which results in a voltage drop [24]. This voltage drop is known as the Hall voltage  $V_H$  and is proportional to current, denoted  $I$ , and magnetic field according to

$$V_H \propto I \times B \quad . \quad (28)$$

The principle behind this generated voltage is generally what is known as the Hall effect [24].

#### 3.2.1 Basic strategy of Hall sensor technology

As Hall effect sensors outputs a small voltage response directly proportional to the magnetic field they are subjected to, they can be used in a variety of sensor technologies. This is possible by using different combinations of mathematical calculations based on the parameters in (28). The specific combinations of this equation depends on the measured quantity that is of interest. In other words, as long as the quantity to be measured incorporates magnetic fields, which is common in electrical applications, a Hall sensor can be utilized [24]. A concept of the working principle for a Hall effect sensor is presented in Figure 13. In this figure a current flows perpendicular to a ferromagnetic ring which concentrates the induced magnetic field around the conductor. This means that the influence of external magnetic fields is significantly reduced [9]. The ring has an air gap of which a Hall element is placed which is made out of semiconductor material and supplied with a continuous small external current [25]. This means that the Lorentz force explained in (27), where an active force arises from a current flowing perpendicular to a magnetic field, causes a voltage drop over the Hall element. This voltage drop is in the range of 30  $\mu\text{V}$  when the surrounding magnetic field is around 1 Gauss. A differential amplifier is consequently needed in order to measure the voltage drop [24].

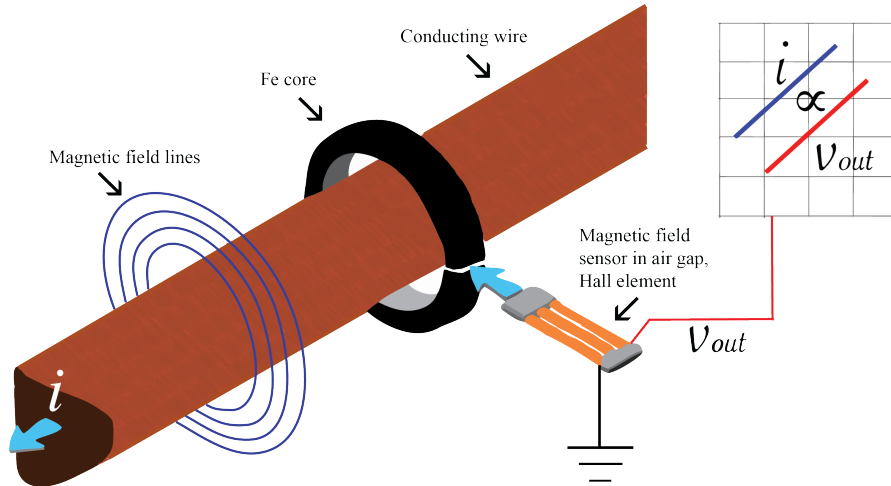


Figure 13: The working principle of a Hall effect sensor.

Hall effect sensors can have both analog or digital output signals where the difference is the characteristics of the output. For the analog case the magnitude of the magnetic field decides the output voltage signal as these are proportional according to (28). For the digital case the output is either on or off and acts more like a switch.

The magnetic field seen from the Hall element can be both negative or positive depending on the direction of the current in the main conductor. This means that the output voltage observed in the Hall element can be either positive or negative. Two power supplies are therefore needed. This problem can be fixed by introducing an offset to the zero voltage such that a new reference "null-voltage" level is reached. This allows the voltage to always stay positive and consequently only one power supply is needed [24]. The output for an analog Hall sensor can be expressed by its input together with the transfer function according to

$$V_{out} = (KV_s)B + (0.5 \cdot V_s) . \quad (29)$$

Here the first term expresses the sensitivity of the sensor where  $K$  is a constant depending on the particular sensor and  $B$  is the magnetic field [24].

A digital Hall effect sensor's output is either in an ON state or an OFF state. This is done by comparing the output of the differential amplifier described in Section 3.2.1 with a reference. A Schmitt trigger is turned on and off depending on the output versus the reference value. A strength with this method is that hysteresis can be implemented within the Schmitt trigger which reduces the effect of disturbances and variations of the magnetic field [24].

### 3.2.2 Hall based current sensors

The strategy for current measurements with Hall sensors can be explained with Figure 13 in mind. The force explained in Section 3.2 acts on the Hall element placed in the air gap of the ferromagnetic ring as visualized in the figure. The output voltage is amplified and proportionally recalculated as a current as explained in Section 3.2.1. As explained in Section 3.2.1, these sensors have either analog or digital output signals and they can also be installed in open- or closed loop configuration. These come with configurations possesses different advantages and disadvantages.

Other than their analog and digital output, Hall effect sensors can be installed in either open- or closed-loop configurations. An example of an open loop sensor configuration is displayed in the previously presented Figure 13. This configuration is the simplest and cheapest as it assumes that the magnetic field around the conductor always is proportional to the current. The bandwidth is limited to the output amplification which is dependant on the distance to the conductor. At close distances and high frequencies the skin effect becomes a limiting factor for this configuration. Typical measurement accuracy for this configuration is around 2-3% and with a bandwidth of around 25 kHz [26], [27].

Magnetic field sensors based on the closed loop strategy utilizes an additional winding around the ferromagnetic ring. This is visualized in Figure 14 and represented by the orange winding. A current is amplified and forced in the direction such that an opposed magnetic field is generated to that generated by the conductor. If the magnetic flux in the ferromagnetic ring is perfectly compensated by this secondary winding, the applied current will be proportional to the current in the main conductor [9].

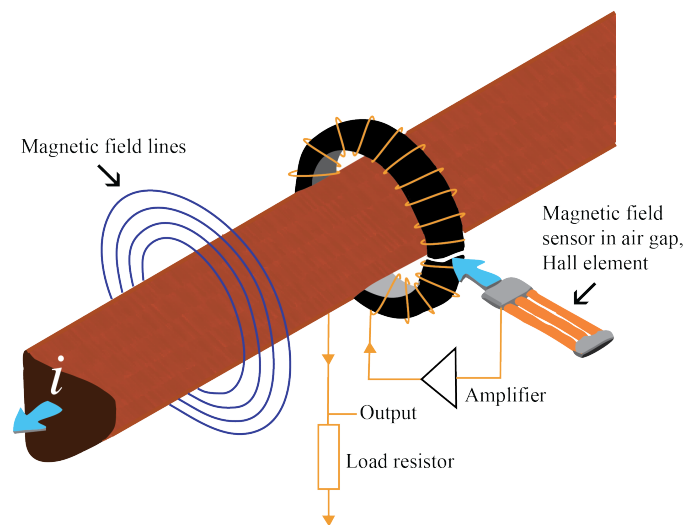


Figure 14: Closed-loop strategy of a Hall effect sensor.

This strategy drastically reduces the temperature dependency and also increases the bandwidth of the magnetic field sensor [9]. The bandwidth for an open loop Hall sensor can be increased to around 200 kHz with the closed loop strategy [27]. Another advantage of the closed loop configuration is an increased accuracy which can reach 0.5% [28]. Since the external circuit compensates the magnetic flux the effect of eddy currents and hysteresis is significantly reduced. The external circuit does however increase the complexity, weight, cost and higher external current is required due to the compensation circuit[9].

### 3.2.3 Galvanic isolation

The previously explained strategy of utilizing the Hall effect for measurements is one example of what is known as galvanic isolation. The principle of galvanic isolation is separation of functional electrical systems, which can have different ground potentials. This is achieved by making sure non direct current can flow between the systems[29]. This principle can be of high importance when comparing sensor technologies as it can have a significant impact on the losses [30].

## 3.3 Rogowski Coil

The Rogowski coil is a current measurement technology that is based on Faraday's law of induction. This law states that a voltage is induced in a coil of wire due to a change in the magnetic field. This entails that this technology provides galvanic isolation but also that it requires a change in the magnetic field and thus a change in the current. This makes this technology unsuitable for low-frequency current measurements such as low speed electric machine operation as this resembles DC operation with a constant current.

## 3.4 Anisotropic Magnetoresistive current sensors

Anisotropic Magnetoresistive (AMR) current sensors are based on the Magnetoresistive effect. They are capable of measuring both DC, AC and pulsing currents with galvanic isolation[31]. The Magnetoresistive effect states that the resistivity of a ferromagnetic material can change in the presence of an external magnetic field. Meaning when current induces a magnetic field as it flows through a conductor it will effect the resistivity of a ferromagnetic material if it is placed in the conductors vicinity. It can also be described accordingly, the electrical resistance of a ferromagnetic material is dependant of the angle between the direction of magnetization and the direction of a passing current [31]. This can be described as

$$\rho(\theta) = \rho_{\perp} + (\rho_{\parallel} - \rho_{\perp})\cos^2\theta \quad (30)$$

where  $\theta$  is the angle between the current direction and the magnetization and  $\rho$  is the resistivity. This means that the resistivity gets a contribution both when the current direction and magnetization are parallel as well as when they are perpendicular.

The working principle of these sensors is that the current to be measured is fed in the path of the sensor. The sensor resistance decreases with the increased magnetic field strength which in turn is dependant on the primary current magnitude. The current path is fed to a current bar which usually is formed as an U-shape feeding the current directly below the sensor [32]. The sensor system contains a Wheatstone bridge which experiences an imbalance caused by the change of resistivity which in turn results in a differential voltage. This voltage is proportional to a current which is the output. This current is amplified and induces a magnetic field of the same magnitude. This means that the magnetic field is compensated and a closed-loop system similar to the Hall effect closed-loop system is created [33]. This described basic principle is illustrated in Figure 15 which displays the U-shaped current bar under a Wheatstone bridge together with the primary and compensation current.

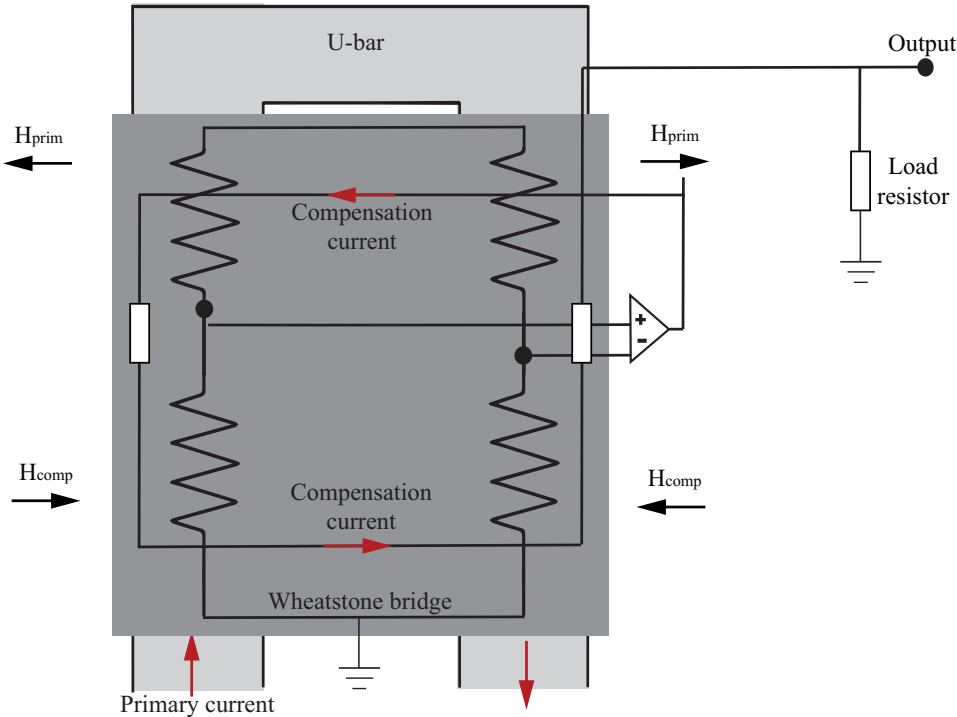


Figure 15: Basic principle of an AMR current sensor.

With these sensors high sensitivity in comparison to the previously presented Hall effect sensors, no iron core surrounding the conductor is needed in order to concentrate the magnetic field. The advantage concluded from this fact is that no hysteresis is observed with the AMR sensors as no iron core is needed [32]. This does however make the closed loop AMR sensors more susceptible to external magnetic fields than other magnetic field sensors with a magnetic

core. Another disadvantage is that the losses become significant at currents above 100 A as best precision is provided when the primary current is part of the sensor module [9]. Depending on the current magnitude and temperatures these sensors reach an accuracy between 0.5-2 % [9], [31].

### 3.5 Effect and causes of current measurement errors

The most typical error caused by inaccurate current measurements in the presented sensor technologies are offset errors. The errors are as the name implies, magnitude errors in either positive or negative direction. These can have their origin in an imbalance between the sensor and the measurement path containing components such as a LPF and an A/D converter. Other error causes can be drift or residual current of the sensors [8]. In synchronous coordinates an offset error can be expressed as

$$\begin{aligned} I_{d_{sensed}} &= I_d + \Delta I_d^e \\ I_{q_{sensed}} &= I_q + \Delta I_q^e, \end{aligned} \quad (31)$$

where  $\Delta I_d^e$  and  $\Delta I_q^e$  is the error. The transformation to synchronous coordinates have taken place according to (2) and (3). This means that the error is related to the electrical frequency and the three phase system of the machine according to

$$\begin{aligned} \Delta I_d^e &= \Delta I_a \cos \theta_e + \frac{1}{\sqrt{3}}(2\Delta I_b - (\Delta I_c + \Delta I_b)) \sin \theta_e \\ \Delta I_q^e &= -\Delta I_a \sin \theta_e + \frac{1}{\sqrt{3}}(2\Delta I_b - (\Delta I_c + \Delta I_b)) \cos \theta_e \quad . \end{aligned} \quad (32)$$

This means that a DC offset error results in sinusoidal torque oscillations at the stator electrical frequency when transformed to the synchronous plane [34].

The cause of the oscillations is visualized in Figure 16. It can be observed that the origo of the dq current vector is displaced due to the offset. Consequently, the current vector experiences oscillations. It should be mentioned that the offset vector is incorrectly scaled as it is enlarged in order to easier visualize the effect of the error.

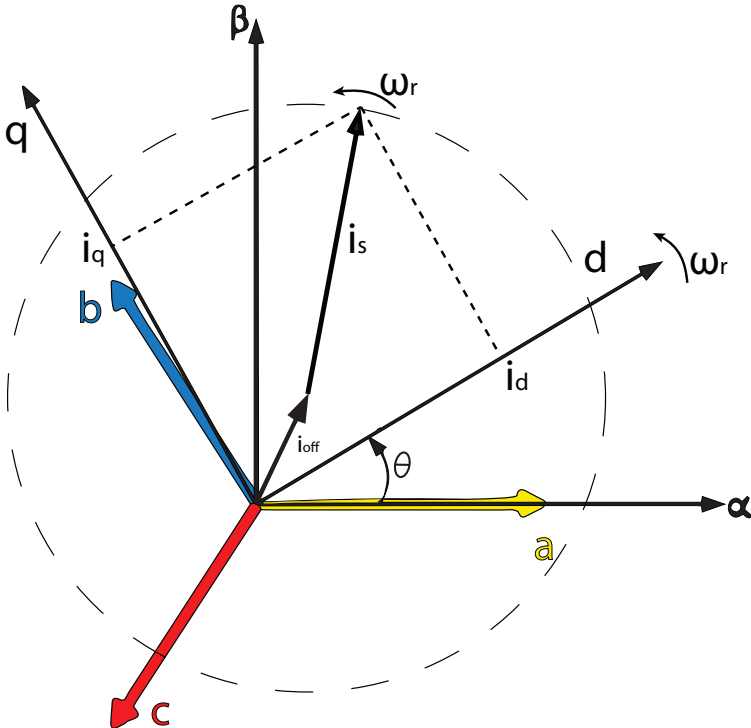


Figure 16: DC offset error in the synchronous plane.

# 4

## Position sensor technologies

FOC, as described in Section 2.1.1, is widely used in control of PMSM in which information of the rotor position is required. The position of the rotor is important because the flux orientation is used in the control algorithms designed to maximize the efficiency of the PMSM. There are different methods to keep track of the rotor position; the position can be measured with a sensor, of which there are different topologies. Alternatively one can implement sensorless control which estimates the rotor position through clever algorithms. In the following sections, different position sensor topologies will be presented in order to understand their advantages and disadvantages.

### 4.1 Resolver

The resolver is a sensor which can be used to obtain information about the absolute rotor position. A typical resolver consists of three windings as illustrated in Figure 17. The primary winding is energized with a high frequency reference signal  $U_{ref}$  which in turn induces voltage in the other two secondary windings. The two secondary windings are placed  $90^\circ$  apart, thus their output signal will be a cosine  $U_{cos}$  and sine signal  $U_{sin}$  respectively. The rotor angle can be calculated as the arctangent of the sine and cosine signal [35].

The primary winding does not have to be in the rotor as it also can be placed in the stator along with the output windings. This type of resolver is known as a Variable Reluctance (VR) resolver, compared to the previous resolver technology which is known as Wound Field (WF) resolver. The VR resolver utilizes a difference in reluctance in the rotor. The sinusoidal output signals come from the resolver's sinusoidal air-gap permeability. This sinusoidally varying permeability comes from the shape of the rotor. The benefits of VR resolver compared to WF is that the VR resolver has a shorter axial length and it is easier to integrate. The VR resolver has a simpler structure and is more robust to external field distortions and varying temperatures [7].

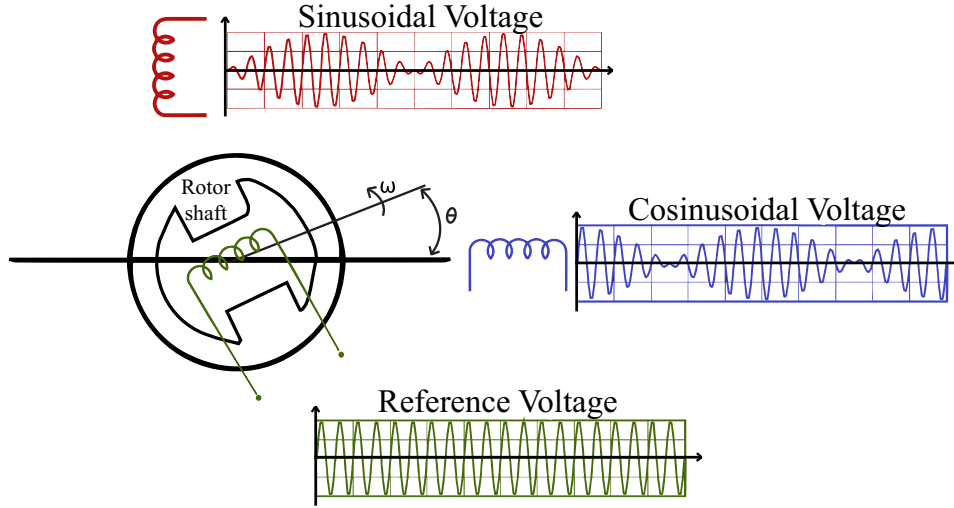


Figure 17: The working concept of a wound field resolver.

The voltage across the windings in the resolver can be described as

$$\begin{aligned}
 U_{ref} &= A \sin(\omega_{exc} t) \\
 U_{sin} &= K A \sin(\omega_{exc} t) \sin \theta \\
 U_{cos} &= K A \sin(\omega_{exc} t) \cos \theta
 \end{aligned}
 \tag{33}$$

where  $A$  is the amplitude of the excitation signal,  $K$  is the transformer ratio,  $\omega_{exc}$  is the frequency of the excitation signal, and  $\theta$  is the rotor angle. In reality however, the signals are not ideal. Errors such as amplitude imbalance, harmonics, imperfect quadrature, excitation signal distortion and disturbance signals can occur. Position errors can however be reduced by using clever compensation algorithms [35]. The amplitude imbalance can occur due to the fact that the transformer ratio between the primary winding and the two output windings are not exactly the same. Imperfect quadrature is another source of errors and caused by the difficulty to assemble the windings into a perfect quadrature. These errors are thus important to consider as they could be responsible for errors in the angle measurements [35].

The resolver is frequently used in many applications where it is required that the sensor has a high accuracy and rugged property [35]. The resolver can normally have an accuracy down towards  $\sim 0.1^\circ$  and can work in a temperature range between  $-40^\circ$  to  $+220^\circ$  [36], [6]. However, along with these properties comes the fact that they require additional electronics to power the excitation winding. It also requires an additional analogue to digital conversion unit to convert the measurement data into digital signals. Resolvers are generally bulky and heavy, consequently they require a large installation space. They are also rather expensive relative to other sensor technologies [37].

### 4.2 Incremental and Absolute Encoder

An encoder is a type of sensor that tracks the position of a rotor by reading a pattern on an encoded disc. A typical incremental encoder works by having an encoded disc mounted on the rotor with equally spaced sections. Two square wave pulses displaced 90 electrical degrees are generated as the disc rotates. It is common that the pulses are generated from photo-detectors by using the pattern on the disc to interrupt a light source. Depending on which pulse that is ahead of the other, the direction of rotation is found. Information of the velocity and position relative to a reference can be measured by measuring the time between pulses. The benefits of an incremental encoder is that it is simple and cheap, however a quite significant disadvantage with is that it is required to start from its reference point. This entails that a power down or a misread pulse by the encoder due to dirty environment or noise, results in an error in the angle reading. This makes this type of sensor impractical for usage in vehicles where the environment can be harsh [6].

An absolute encoder has the ability to maintain and read the position information after the power has been shutdown. This is done by reading a binary encoded pattern on the rotor which it decodes into a position. The segmented patterns are on multiple concentric tracks. The resolution of the absolute encoder depends on the number of tracks on the disc, if the absolute encoder has 10 tracks, then this corresponds to a 10-bit resolution [6].

### 4.3 Optical Encoder

The encoder can also use different sensing methods; one common method is the optical encoder which has a light source that emits light through a encoded disc as illustrated in Figure 18.

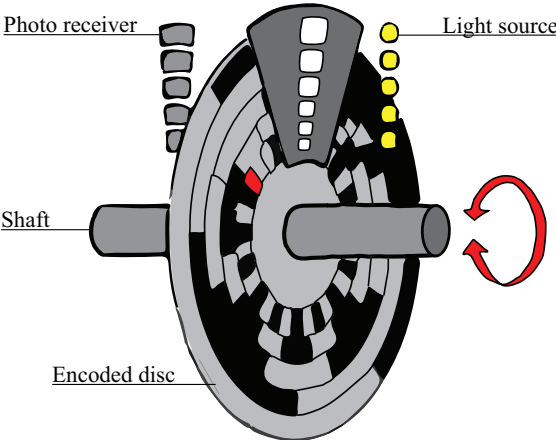


Figure 18: An illustration of an absolute optical encoder.

An optical encoder can offer a high resolution and accuracy. A high accuracy encoder can have an accuracy down towards  $\sim 0.0014^\circ$  [38]. However, it has some weaknesses that need to be considered. It only works in the limited temperature range between  $-20^\circ\text{C}$  to  $+70^\circ\text{C}$ . Another significant disadvantage is that it cannot cope with harsh environments which subjects the sensor to shock and vibrations. The encoder is also susceptible to foreign matter such as dust particles which makes it unreliable in such environments. The sensor could give erroneous readings if objects such as a dust particles gets attached to the disc which reflects or blocks light [37]. The red colored bit on the encoded disc in Figure 18 signifies that a dust particle is covering it. As an example, this could mean that the measurement reading of that bit could end highly erroneous where it measures a bit pattern that is totally off.

#### 4.4 Capacitive Encoder

Another type of encoder is a capacitive encoder which senses the pattern through changes in capacitance. A transmitter sends a high frequency signal through the rotor disc mounted on the rotor. This signal is received by a receiver which detects sinusoidal changes in capacitance as a pattern as illustrated in Figure 19. The shape of the sinusoidal signal will change depending on the rotor speed and position [6].

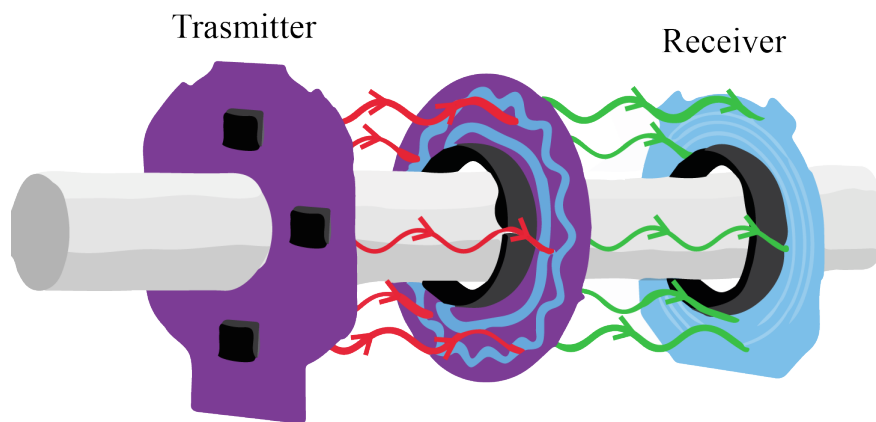


Figure 19: An illustration of a capacitive encoder.

The capacitive encoder provides high resolution and accurate position measurements. Typical high accuracy values of this type of encoder is around  $\sim 0.2^\circ$ , and it has a working temperature range between  $-40^\circ\text{C}$  to  $+125^\circ\text{C}$  [39]. The capacitive encoder is less affected by dusty and harsh environments than the optical encoder which makes the capacitive encoder more reliable. They are however still sensitive to foreign matter, changes in temperature and humidity as these things can affect the capacitance by changing the permittivity which may result in faulty readings. These typical error sources therefore result in an error similar to the optical encoder where a bit pattern could be affected, which would result in a jump in the measurement signal. For the sensor to work properly in a vehicle applications, the surrounding environment of the

capacitive encoder needs to be sealed or tightly controlled [40]. It is however not an easy solution as it is difficult to completely eliminate the exposure to environmental contaminants such as condensation. The housing can also introduce new factors such as elevated temperature and an increase in cost [41].

Relative to the size of the capacitor plates, the distance between the sensor's plates must be small. Mechanical installation of these sensors can consequently be difficult. This also makes them sensitive to mechanical vibrations and thermal expansion which introduces noise to the measurements [40].

## **4.5 Inductive Position Sensor**

The main principle behind inductive position sensors is Faraday's law of induction which states that a varying magnetic field will induce a current. A typical inductive sensor is the Resolver which has been mentioned in an earlier chapter. The inductive position sensor measures the induced voltage signal on the receiving end which is affected by displacement and geometrical factors between the transmitting and receiving coil.

An inductive sensor can handle harsh environments much better than e.g. a capacitive encoder. This is because inductive sensors are less sensitive to foreign matter such as dust particles or water. The coils in the sensor are also not required to be installed closely to each other relative to a capacitive encoder as their operation still works well at a distance. This fact entails that there is less requirements on precise installation of the sensors which minimizes cost and makes the sensor more robust when installed [42].

The disadvantage of traditional inductive sensors however is that their construction requires accurately wound coils in order to accurately measure the position. These coils which are essential parts of the sensors construction make the sensors heavy, bulky and expensive [42].

## **4.6 Inductive Encoder**

An approach different to the traditional inductive sensors is the Inductive Encoder [43]. This sensor uses printed circuit boards and modern digital electronics compared to the traditional inductive sensor which uses analogue electronics and bulky wire wound spools as transformers [42]. Although the sensors are of different technology, they are based on the same physical principles of Faraday's law, and thus share similar error sources such as amplitude imbalance and imperfect quadrature. However, because the sensor coils and the electronics are integrated in a silicone chip, the Inductive Encoder is more compact [44]. This sensor technology offers similar properties as the traditional inductive sensors such as reliability and precision in harsh environments. This new generation of inductive sensing also has improved advantages which are [45]

- Improved accuracy;
- Reduced weight;
- Reduced cost;
- Eradication of bearings, seals & brushes resulting in simplified mechanical installation;
- Compact size.

The accuracy of the Inductive Encoder can be as good as  $\sim 0.02^\circ$  which is an improvement from the resolver [46]. The Inductive Encoder has however a temperature range between  $-100^\circ\text{C}$  to  $+125^\circ\text{C}$  which is less than what the resolver is capable of [47].

The inductive sensor has a simple electrical interface as it requires only a DC power supply. Compared to e.g. a resolver, the inductive encoder does also not need an analogue to digital conversion unit. This is because the sensor already outputs the digital signal representing the absolute angle as all the electronics are integrated in the inductive encoder. Regarding the working temperature range, there are instances where the inductive encoder has been used in environments up to  $230^\circ\text{C}$  [37].

## 4.7 Sensorless control

The possibility of sensorless control for a PMSM can be of high interest since it removes the cost of buying sensors and the challenges that come with their implementation into the system. The sensors however need to be replaced with clever algorithms that can estimate the rotor position as it is essential information for the control system. There are different methods of creating an observer structure which can estimate the rotor position [48]. Sensorless algorithms typically uses the back-EMF of the PMSM to estimate the speed and rotor position since they are proportional to each other according to

$$U_{EMF} = \omega_r \psi. \quad (34)$$

The back-EMF  $V_{EMF}$  is proportional to the electrical speed  $\omega_r$  and the flux  $\psi$ . The estimation of the rotor angle can be accurate when the machine operates at nominal speeds. It is however difficult in practice to estimate the rotor position at low or zero speed while guaranteeing stability and accuracy [13]. This is a big issue with sensorless control, as these factors are important aspects of for a well functioning vehicle operating over all speeds.

# 5

## Drive system modelling

In order to evaluate sensor technologies for usage in CEVT's new DHT, the impact of measurement errors needed to be understood. Simulated sensors blocks were implemented with offsets and time delays to both the measured currents and rotor angle in a PMSM Simulink model. This chapter presents how this Simulink model was built together with the strategy used to present a perspicuous comparison of applicable sensor technologies. Due to the nature of confidentiality of the specifications currently being developed, the system properties presented in this report are not identical to the real system used by CEVT.

The area of focus for this thesis was the electrical subsystem in Figure 1. This subsystem includes the transmission, PCM and two PMSMs together with a battery pack. Current and position measurement signals are fed into the control system which besides controlling, strives to optimize the efficiency of the system. As described in Section 2.1.1 and Section 2.2.4, the rotor angle measurement is essential for FOC and the current measurement is essential for finding the optimal MTPA currents. The FOC strategy for the PMSM is presented in Figure 7. The figure presents both the speed and current control blocks which are fed with dq-transformed quantities. The current control output is fed to the PWM and then to the inverter which feeds the PMSM with calculated magnitudes of three phase voltages. The PMSM drive system was modelled using the theory presented in Section 2.1 and Section 2.2. The model was built using the Simulink extension in the calculation software MATLAB. An overview of the constructed Simulink model is presented in Figure 20.

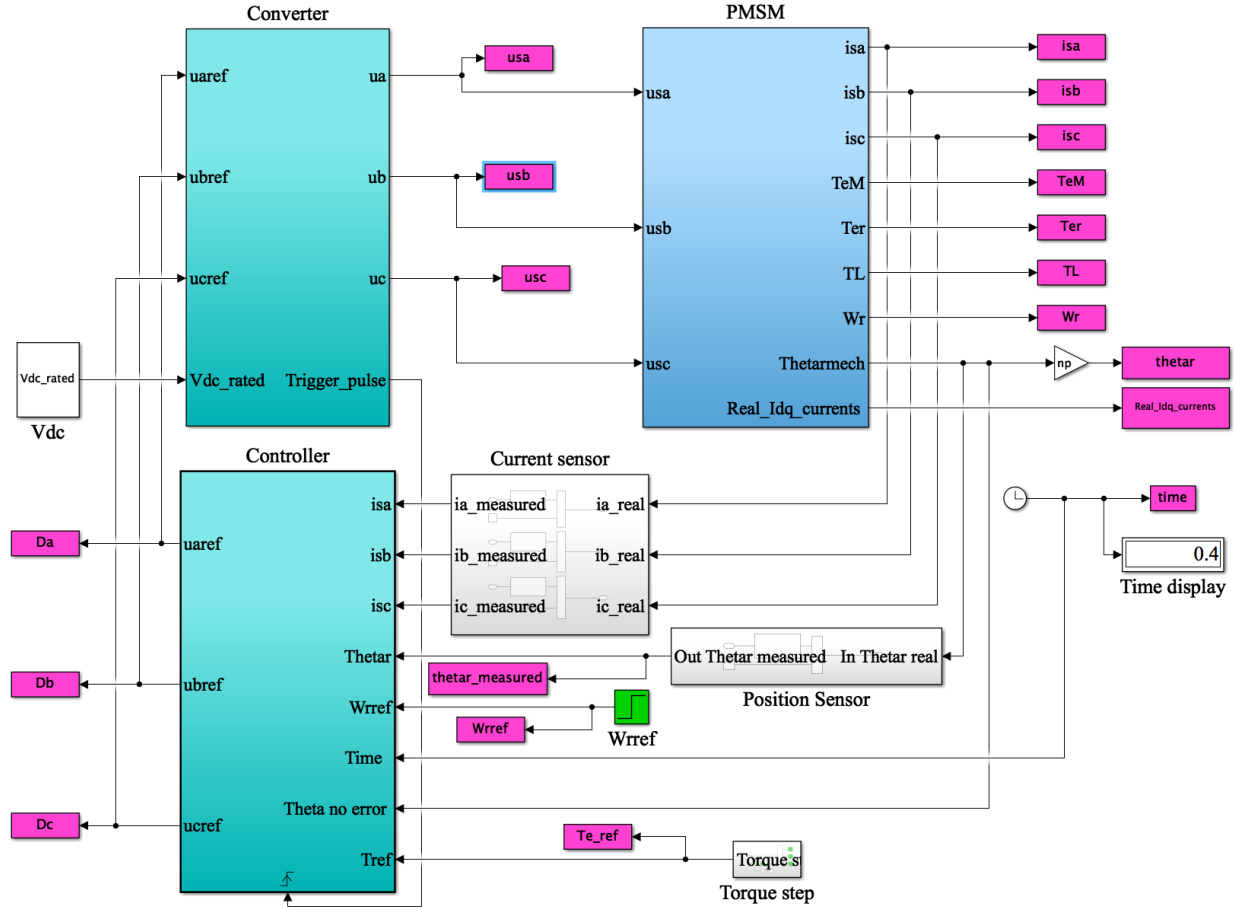


Figure 20: Simulink model of the PMSM system consisting of the PMSM, control system, converter and measurement sensors.

The simulink model consists of a blocks representing the different subsystems. The subsystem block which models the PMSM is shown in Appendix 2, the subsystem block representing the converter can be found in Appendix 4, the block representing the controller can be found in Appendix 1.

## 5.1 PMSM model

In Simulink, the PMSM was modelled as a S-function built up by state space equations for the PMSM. The state variables were  $I_{sd}$ ,  $I_{sq}$ ,  $\omega_r$  and  $\theta$ . The state space equations for the current components were rewritten from (5) and (6) as

$$\frac{di_{sd}}{dt} = \frac{1}{L_{sd}}(u_{sd} - R_s i_{sd} + \omega_r L_{sq} i_{sq}) \quad (35)$$

$$\frac{di_{sq}}{dt} = \frac{1}{L_{sq}}(u_{sq} - R_s i_{sq} - \omega_r L_{sd} i_{sd} - \omega_r \psi_m) \quad (36)$$

The electrodynamical torque was calculated according to (7) and the load torque modelled as

$$T_{load} = B \frac{\omega_r}{n_p} + T_{L_{extra}}, \quad (37)$$

where B is the viscous damping coefficient. The mechanical equation which describes the behavior of the rotor is the swing equation (9) which also was the third state equation. The fourth state equation describes that the derivative of the rotor angle is the rotor speed

$$\frac{d\theta}{dt} = \omega_r. \quad (38)$$

As previously mentioned the DHT consists of two PMSMs responsible for different types of driving situations. This means that the machines are of different design, size and build up by different parameter values. As CEVT's real machines are in a pre-production stage, the original parameters of the machines are of sensitive character and therefore confidential. With this considered, parameters of similar kind were provided by CEVT and implemented into the system and are presented below in Table 1. As stated in Section 1.3 this thesis is limited to only design the traction PMSM of the system and accordingly only parameters for this motor is presented.

Table 1: Parameters used to simulate a PMSM.

Parameter	Dimension	Value	Description
$n_p$	N/A	12	Number of pole pairs
$R_s$	[ $\Omega$ ]	0.015	Resistance of one motor phase
$L_d$	[ $\mu$ H]	60	d-axis inductance of one motor phase
$L_q$	[ $\mu$ H]	120	q-axis inductance of one motor phase
J	[ $kg/m^2$ ]	0.8	Moment of inertia
B	[Nm.s]	0.318	Viscous friction coefficient
$I_{Rated}^{Stator}$	[A]	450	Rated stator current
$V_{Rated}^{Dc}$	[V]	360	Rated Dc bus voltage
$n_{Rated}$	[rpm]	3600	Rated speed
$T_{Rated}$	[Nm]	120	Rated Torque
$n_{Max}$	[rpm]	9000	Max speed
$T_{Max}$	[Nm]	377	Maximum Torque

A rated operation point of a specific speed and torque combination was provided by CEVT as presented in Table 1. In order to operate at this point, the viscosity coefficient was calculated according to (9) and resulted in the value presented in Table 1. The inertia was chosen to its particular value such that it allowed for shorter computation time while representing a close to realistic acceleration.

The output power can be calculated according to (10) and is usually presented by the usage of a torque and speed map as presented in Figure 21. These particular maps visualizes the motor size and additional motor information for the machine presented in Table 1. The operating area of the machine depending on specifications of maximum output power, torque and speed can be observed in the figure. The maximum torque is calculated from the motor parameters according to Section 2.2.4 and the maximum power can be calculated from the current and voltage. By increasing the speed, the maximum torque will according to (10) be limited by the maximum power.

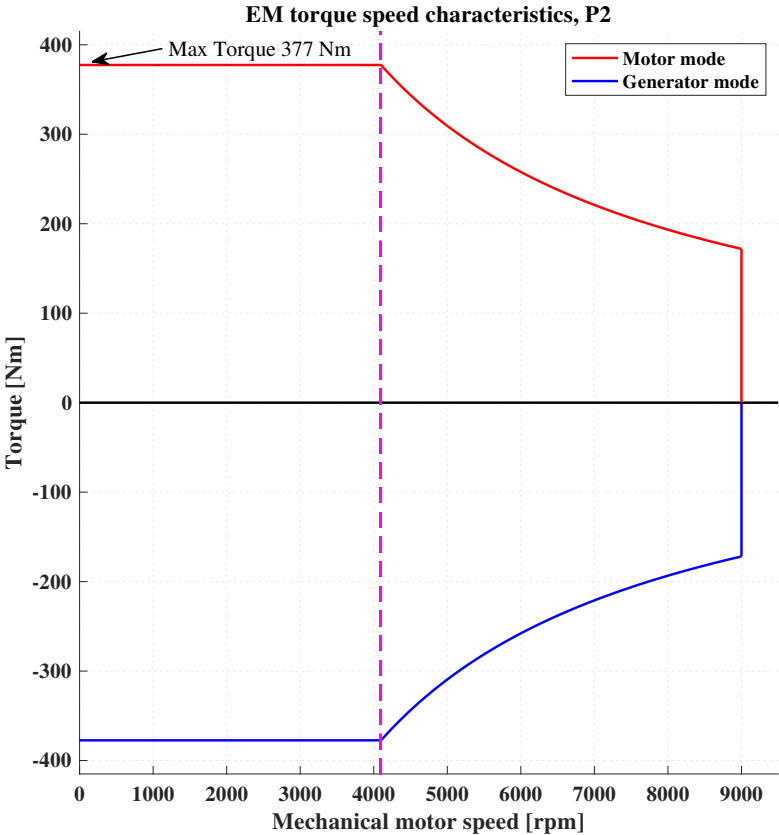


Figure 21: Torque speed characteristics of the simulated PMSM.

## 5.2 Field oriented controlled PMSM Simulink implementation

As described in Section 2.1 FOC is an effective way of creating an efficient control system. This was implemented as presented in Figure 7 where Clarke and Park transformations are used in both directions. This figure visualizes the importance of accurate measurements as the errors will have a big negative impact due to the number of transformations. This section further describes the method used to model and simulate the controller block which regulates the drive system. A continuous system is much simpler than a discrete system and was consequently modelled initially. This allowed for easier understanding and visualization of the system response.

### 5.2.1 Implementation of the current controller

A current controller was built according to Section 2.2.1 and is visualized in Figure 8. Once the current controller was implemented a simulation with a torque reference step was performed. The torque reference was sent as an input to a controller block, representing the PCM in the DHT system. The previously discussed operating point provided by CEVT with a speed of 3600 rpm and torque of 120 Nm was used throughout the thesis. This simulation verified that the step response looked as expected and also allowed evaluation of suitable controller parameters. The bandwidth was set according to previous knowledge of suitable values strengthened by observations of varying values in simulations until a first order step response without overshoots was observed. The switching frequency of the PCM was specified by CEVT to be 10 kHz which also was taken into consideration during the determination of controller bandwidth.

The final bandwidth was chosen as 6000 rad/s and the control parameters set as (14) and (15) in Section 2.2.1 with the machine parameters in Table 1. This resulted in

$$\begin{aligned}K_{Pcd} &= 0.36 \\K_{Pcq} &= 0.72 \\K_{Icd} &= 2160 \\K_{Icq} &= 4320 .\end{aligned}\tag{39}$$

### 5.2.2 Implementation of the speed controller

Once the system worked as expected, the torque reference was replaced by a speed reference as a speed controller was implemented in the controller block. One of the final goals of the thesis was to highlight increased currents for a specific operating point due to measurement errors. It

was concluded that a speed reference would be the most optimal method for this purpose and thus this method was used throughout the rest of the simulations.

Similar to the current controller bandwidth argumentation, the speed controller bandwidth was decided but with an additional important fact in mind. As discussed in Section 2.2.2 the speed controller is the outer control loop in the system while the current controller is the inner control loop. This implies that the current controller must be faster than the speed controller and the bandwidth of the speed controller was chosen to be at least 10 times smaller than the current controller. After performed simulations the final value was set as 60 rad/sec and the control parameters decided according to (19) with the machine parameters in Table 1. This resulted in

$$\begin{aligned} K_{Pw} &= 0.12 \\ K_{Iw} &= 7.2 . \end{aligned} \tag{40}$$

### 5.2.3 Implementation of MTPA/MTPV

The speed controller delivered a torque reference which in turn was sent as an input to a MTPA/MTPV calculation block as described in Section 2.2.4 and Section 2.2.5. This limited the torque with field weakening and also limited the currents to stay within their maximum value. The MTPA block delivered calculated reference currents to the current controller.

### 5.2.4 Phase locked loop

As explained in Section 2.2.3, the mechanical speed cannot simply be calculated as the derivative of the measured angle because of high frequency noise. This was instead calculated by the usage of a PLL as explained in Section 2.2.3. The PLL block was implemented in the controller block and estimated the speed of the machine. The PLL has to be much faster than the speed controller as described in Section 2.2.3. The later simulations which were performed on a discrete system required a long computation time, consequently the inertia was reduced in order to increase acceleration and allow for a shorter simulation time by reaching steady state faster. Thus the bandwidth of the PLL was chosen to be as high as 2000 rad/s which was obtained from test simulations where a well operating system was observed. This bandwidth used in (20) resulted in

$$\begin{aligned} K_{PPLL} &= 4000 \\ K_{IPLL} &= 4 \cdot 10^6 . \end{aligned} \tag{41}$$

### 5.3 Discretization of the simulink model

In order to create a more realistic PMSM model, the system was discretized by substituting all continuous integration blocks with discrete integration based on the Forward Euler approximation as presented in Figure 22.

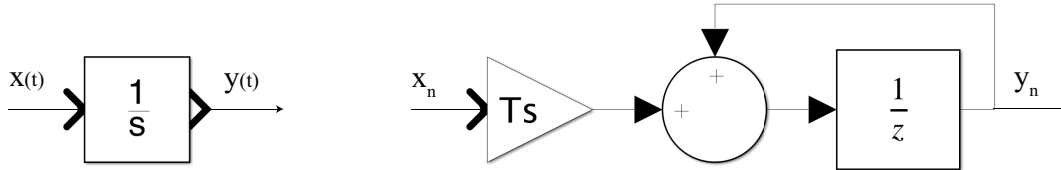


Figure 22: Continuous integration versus discrete integration.

Further a duty cycle block was added which calculated the ratio between the pulse duration and the time period of the controller output reference voltages. A PWM block sent a trigger pulse to the controller block in order to sample according to the previous mentioned switching frequency.

The method towards building a working model was continued by performing simulations verifying that the sampling worked as intended. The duty cycle was compared with the sampling points, PWM carrier wave and resulting phase voltage in a simulation presented in the upcoming result chapter. Once correct sampling was verified a simulation of the entire system was performed. This simulation confirmed that the speed and current controller worked together with the speed estimation from the PLL. Discretization of the controller block meant that a phase shift in reference voltages was added, usually referred to as half a cycle delay, since there is a delay between two sampling points. This was done by feeding forward a delay angle by adding the phase shift  $\frac{\omega T_s}{2}$  radians. Without compensating for the delay, the sampling follows the desired signal with a delay as illustrated to the left in Figure 23. The signal to the right shows how the sampling more accurately follows the desired signal when the phase shift is added.

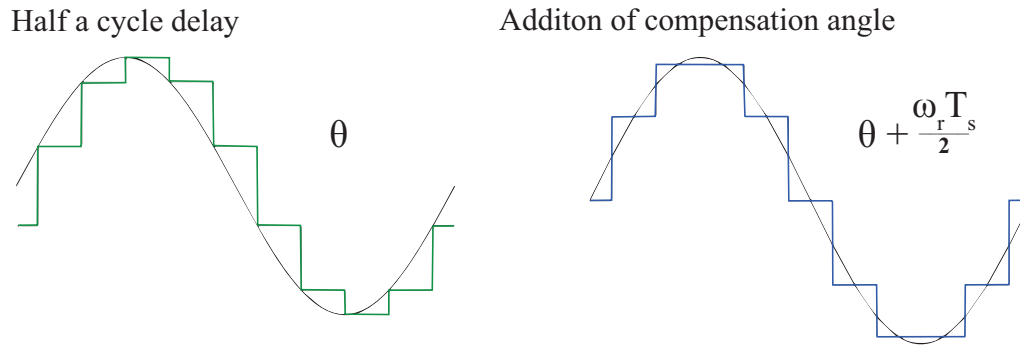


Figure 23: Left figure showing the effect of half cycle delay due to the sampling time. The figure to the right shows how the sampling better follows the sine function with feed forward of the compensation angle.

## 5.4 Implementation of sensor measurement errors in Simulink model

Once expected results of a working PMSM system was observed for the model presented in Section 5.2 and Section 5.3, sensor models with implemented measurement errors could be added. Since the scope of the thesis included both current and position measurement errors, the strategy was to implement one sensor with errors at a time. After that had been done, combinations of measurement errors were implemented. This section further discusses the method used to implement measurement sensors with different errors.

In order to implement typically occurring errors in the intended application with reasonable magnitudes, a literature study of sensor error characteristics was conducted. This literature study proved that the existing sensor technologies were associated with different types of errors of varying significance. In order to efficiently analyze the impact of the errors from several technologies simultaneously, the errors were implemented as their worst case scenario. The error parameters were swept and started as a value representing a small error which grew larger until critical system behavior was observed.

The continuous system was initially used to highlight the effect of the implemented errors and observe the system response. Subsequently, sensors were implemented in the discrete system which was a more realistic scenario to analyze.

### 5.4.1 Implementation of a current sensor

The method used to implement a current sensor was to add a block between the PMSM and the controller block as presented in Figure 20. The three phase currents were available for measurements and all three phases were also required by CEVT to be measured due to safety reasons as discussed in Section 3. These currents became the input signals to the modelled current sensor.

DC offsets were added to each of the three phase currents. As these were transformed into dq-quantities, according to (2) and (3), the resulting offset error became (32). A parametric sweep of the current offset magnitude in each of the three phases was performed. The requirement found in the DHT specifications stated that the current sensors should be able to measure  $\pm 500$  A with an accuracy of 1% resulting in  $\pm 5$  A. This means that the sensors being simulated for each phase has a maximum error of  $\pm 5$  A. With this in mind, the combination that results in the largest offset current vector is to implement a positive offset in the "a" and "b" phases and a negative offset in the "c" phase with magnitudes of 5 A which can be derived from (2).

This phase current offset combination does not sum up to zero and therefore leaves a zero-component. Thus the current sensor has introduced a DC offset with a zero-component to the phase currents. However, this zero-component does not affect the system as it does not follow into the dq-transformation since the transformation uses the assumption that the three phase system is balanced. The phase current offsets could be chosen such that the sum becomes zero resulting in no zero-component. However, in order to end up with  $\alpha\beta$  currents of the same magnitude as the previous current vector, one of the phase currents would have to be larger than 5 A thus exceeding the sensor requirement.

In order to simulate a time delay of the current sensor, a first order LPF was added to the sensor block which introduces a time delay. The initial bandwidth of the filter was set to match the bandwidth of state of the art sensors found in sensor manufacturer datasheets. The impact of different bandwidths was investigated by a parametric sweep with the bandwidth as the error parameter. The bandwidth of the LPF can be translated to different time delays as there is an inherent delay in the response of a LPF depending on its bandwidth. The introduced time delay can be approximated as the rise time of the LPF. This rise time is calculated as

$$t_{rise} = \frac{\ln(9)}{\alpha_{cs}} \quad (42)$$

where  $\alpha_{cs}$  represents the LPF bandwidth in radians in the current sensor. The transfer function of the chosen LPF is expressed as

$$H_{cs}(s) = \frac{\alpha_{cs}}{s + \alpha_{cs}} \quad (43)$$

### 5.4.2 Implementation of position sensor

Since the initial strategy was to simulate one error at the time, the current sensor was disabled once the effects of its measurement errors had been analyzed. Subsequently, a position sensor was modelled and placed between the PMSM and the controller block. The angle from the machine was sent as the input signal to the sensor block and the output was sent to the controller block as presented in Figure 20. This was followed by simulations of position measurement errors described in Section 4. It was concluded that most of the discussed errors resulted in a total error which could be translated to an angle offset. This error was consequently simulated by performing a parametric sweep with a position offset angle between  $\pm 0.25$  and  $\pm 3$  mechanical degrees. These particular values were chosen as this interval was considered to be the most interesting and relevant in regards to the system behavior.

The consequence of adding this offset angle affects the dq-transformation matrix in (3). The offset angle is added to  $\theta$  such that the angle becomes  $\theta + \phi_{offset}$ . From the simulations it was observed that an error larger than 3 mechanical degrees was not realistic as it resulted in a critical error, whereas an offset of 0.25 degrees yielded smooth results. This sensed angle with added offsets was fed into the PLL which estimated the speed of the machine and delivered it to the speed controller. The sensed angle was also fed as an input signal to the three phase current Clarke's transformation together with the current controller output voltage references reverse Clarke's transformation.

Similar to the current sensor in Section 5.4.1, a LPF was added to the modelled position sensor in order to simulate time delays. Once again a parametric sweep with the bandwidth as error parameter was performed in order to analyze the effect of this error. The transfer function for this LPF is expressed as

$$H_{ws}(s) = \frac{\alpha_{ps}}{s + \alpha_{ps}} . \quad (44)$$

### 5.4.3 Implementation of combined current and position errors.

The last interesting case to analyze was implementation of combined current and position sensor measurement errors. This case is more realistic as both sensors always operate simultaneously in the vehicle. The previously presented parametric sweeps of error parameters was therefore implemented together and simulated simultaneously. A limitation of this simulation scenario can be found in the scope of the thesis presented in Section 1.3. As described in the scope there are countless possible combinations of error parameters, thus only the most interesting combinations were simulated. The first interesting scenario was with the error parameters which individually yielded best performance. Another simulated scenario was the combination of error parameters which individually yielded the worst performance. The final simulation was performed with a combination of errors somewhere in between the best and

worst case parameter values. The corresponding parameter values for these scenarios are presented in Table 2.

Table 2: The implemented combinations of sensor error parameters that were of interest.

Scenario	DC offset magnitude [A]	Current sensor LPF bandwidth [kHz]	Time delay [ $\mu$ S]	Mechanical angle offset [degrees]	Position sensor LPF bandwidth [kHz]	Time delay [ $\mu$ S]
Optimal case	$\pm 1$	500	4.4	0.25	10	220
Realistic case	$\pm 3.5$	100	22	1	7.5	293
Worst case	$\pm 5$	25	88	3	2.5	880

## 5.5 Evaluation of applicable sensor technologies

Additional to analyzing the effects of sensor measurement errors for a PMSM, another goal of this thesis was to present a comparison of applicable sensor technologies. As presented in Chapter 3 and 4, several sensor technologies can be used for measuring the PMSM phase currents and the rotor position. In order to present a perspicuous comparison of the applicable sensor technologies, a gathering of knowledge of their attributes was conducted. Similar projects with deeper investigations into the individual sensors was examined through an extensive literature study. The technologies main advantages and disadvantages in Chapter 3 and 4 was later compiled into tables which provide an overview of the different sensor's main attributes.



# 6

## Results

The Simulink model of the PMSM with implemented measurement errors were simulated with regards to various conditions. This section demonstrates an initial continuous system with sensor errors implemented in order to highlight the effect of these particular errors. This is followed by simulated results of a discrete system with parametric sweeps of the error parameters. These results highlights critical error parameter values in a more realistic system than the continuous. Lastly a comparative overview of applicable sensor technologies is presented in the form of comparison matrices.

### 6.1 Simulation results of continuous system without errors

The first simulation was performed with an applied torque step of 120 Nm according to Section 5.2.1 in order to find suitable current controller parameters. This resulted in the first order step response presented in Figure 24. The figure contains six graphs showing the speed, torque and the currents both as full scale and zoomed in order to highlight the rise time. From (42) with a bandwidth of 6000 rad/s the rise time is expected to be 0.36 ms which is confirmed by the simulation. It can be observed that the torque reference is reached without overshoot or any oscillations which is expected from a first order response. The inertia of the machine was set to a relatively low value which reduces the time the machine is in the dynamic state and allows quicker computation time. This strategy was used throughout the rest of the simulations since it is the steady state performance which is of interest. As the rated operation point is reached the system works as expected and well performing control parameters have been implemented.

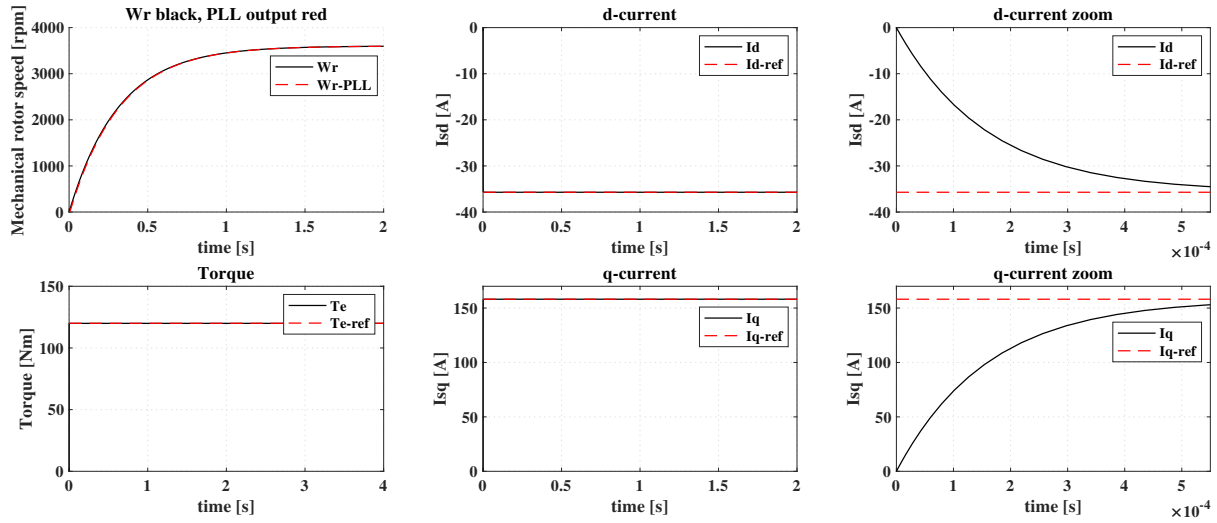


Figure 24: PMSM dynamics in a torque reference step response.

With a confirmed well performing current controller, the torque reference was replaced with a speed reference as explained in Section 5.2.2. The speed controller delivers a torque reference to a MTPA/MTPV block which was simulated in order to confirm that functions such as field weakening worked as expected. Parameters such as inertia, viscosity and the speed reference was set to reach a high torque and increasing speed. This resulted in Figure 25 which shows similar behavior as Figure 12 explained in Section 2.2.5. The torque stays at its maximum value until the base speed at around 3000 rpm is reached. Here the voltage contribution from back EMF have grown to large and in order to reach higher speeds field weakening as explained in 2.2.5 begins which leads to a reduction of the torque.

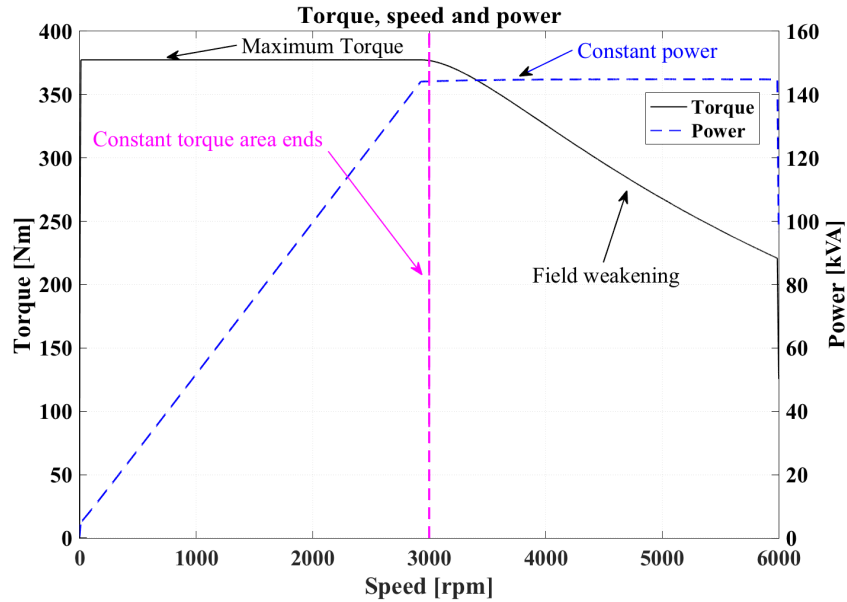
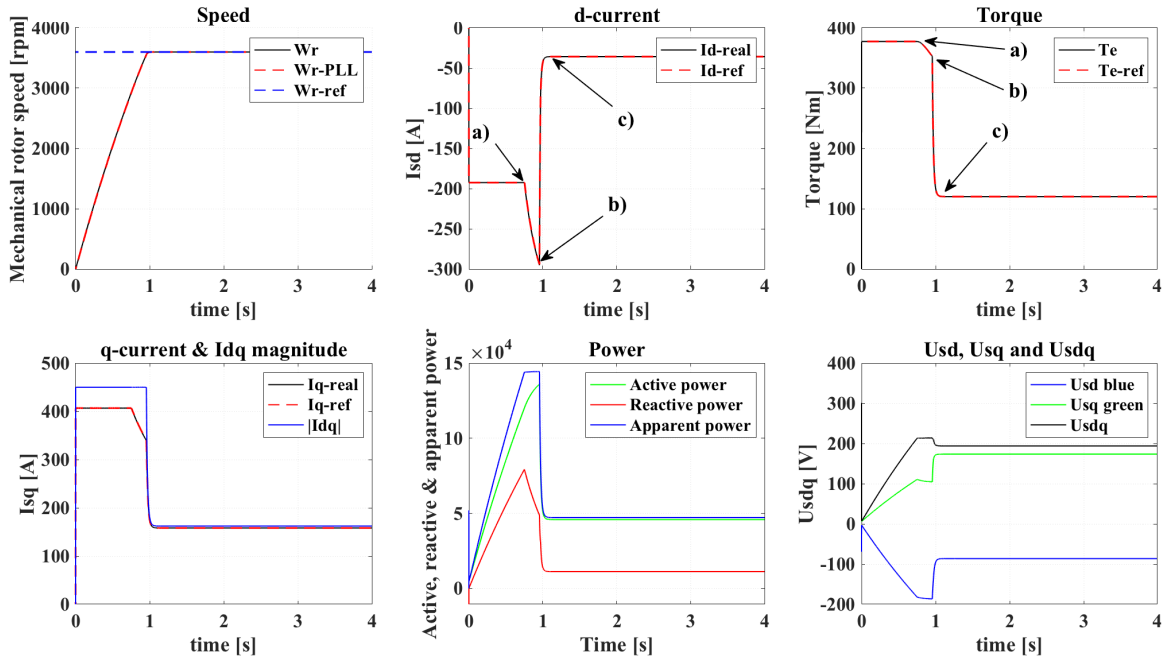
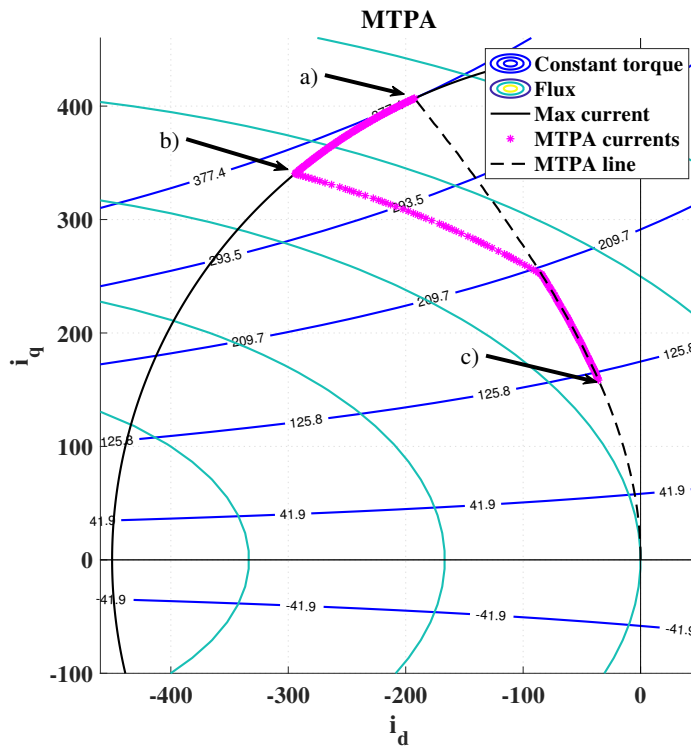


Figure 25: The relation between torque, speed and power together with demonstrated field weakening.

The operation of the speed controller was simulated with same operating point. The result of this simulation together with the corresponding MTPA plot is presented in Figure 26. It can be observed that the desired operating point once again is reached without overshoots which indicates a functioning speed controller. The torque starts at max in order to quickly reach the speed reference but as observed the current magnitude is limited to the rated current of 450 A. Consequently a first order step response is not observed in this case. At point "a" the speed has increased to a level which corresponds to a back EMF contribution resulting in maximum allowed voltage. At this point, field weakening starts by applying an increased negative d-current which is observed between point "a" and "b". During this field weakening the power is constant which is in accordance to Figure 12. Once the speed reference is reached the machine stops accelerating and the torque demand is consequently reduced according to (9). The currents now follow a constant flux path until reaching the MTPA curve which is followed down towards the rated operating point at "c".



(a) System response with implemented speed controller.



(b) Corresponding MTPA plot.

Figure 26: Verification of a working speed controller.

## 6.2 Continuous system sensor error simulation

The confirmed functional continuous system with implemented current and position sensors according to Section 5.4 was simulated in order to highlight and easier interpret the effect of specific errors.

### 6.2.1 Current sensor errors

The effect of having a 5 A DC-offset in phase "a" and "b", and -5 A offset in phase "c" as discussed in 5.4.1, is shown in Figure 27. It can be observed, as corroborated by Section 3.5, that a DC offset error in the phase currents becomes an AC ripple with the stator electrical frequency which is 720 Hz and a ripple amplitude of 6.66 A. Since the currents are directly related to the torque according to Section 7, a ripple is also observed in the torque with the same frequency and with an amplitude of 4.85 Nm. The effect of the torque ripple results in a ripple in the speed, but the inertia of the machine reduces the effect of this ripple to be close to negligible. The mechanical speed is observed to be 3600 rpm which corresponds to 60 Hz which in turn corresponds to an electrical frequency of 720 Hz.

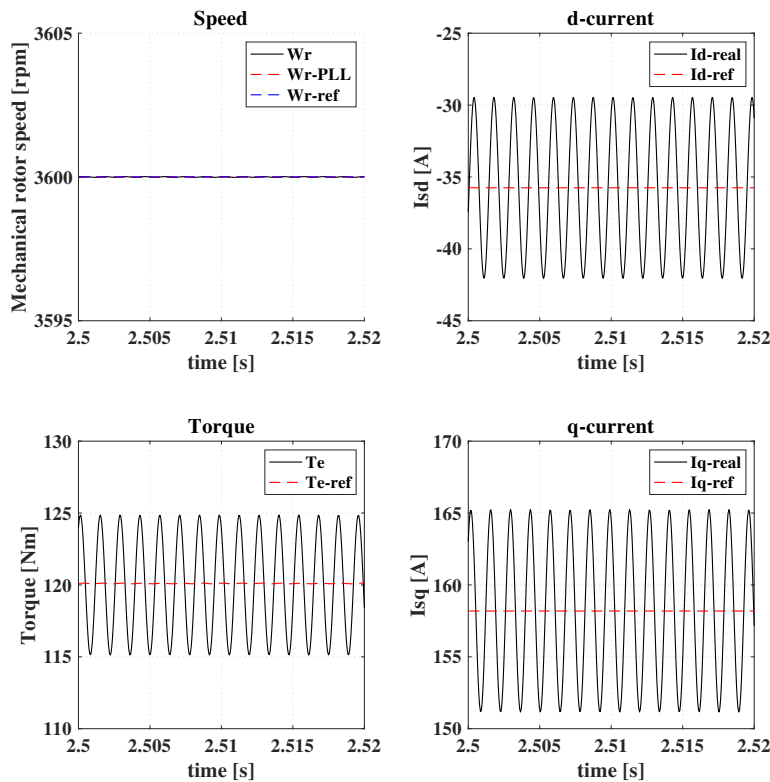


Figure 27: The effect of a 5 A DC-offset applied to phase "a" and "b" and -5 A to phase "c".

### 6.2.2 Position sensor error

A simulation of the previous mentioned operating point of 3600 rpm and 120 Nm with a offset of +0.5 degrees on the mechanical angle was performed. The purpose of this simulation was to highlight the effect of an measurement error that results in a offset of the mechanical angle in a continuous system in which it is easier to observe the effect. This resulted in Figure 28 where it can be observed that the operating point is reached but the current has increased due to the measurement error. The perceived dq-currents are the measured currents as perceived by the controller after an incorrect dq-transformation due to an erroneous angle reading. Due to this error, the speed controller believes it has to request a higher torque in order to reach the operating point which is the explanation to why the torque reference is larger than 120 Nm.

Another observation is that the error in d-direction is much bigger than the error in q-direction. This can simply be explained by the cosine and sine relation of the currents and that these have different impacts at different angles. If the current vector would be closer to 180 degrees than 90, the current in q-direction would experience a larger effect from the measurement error.

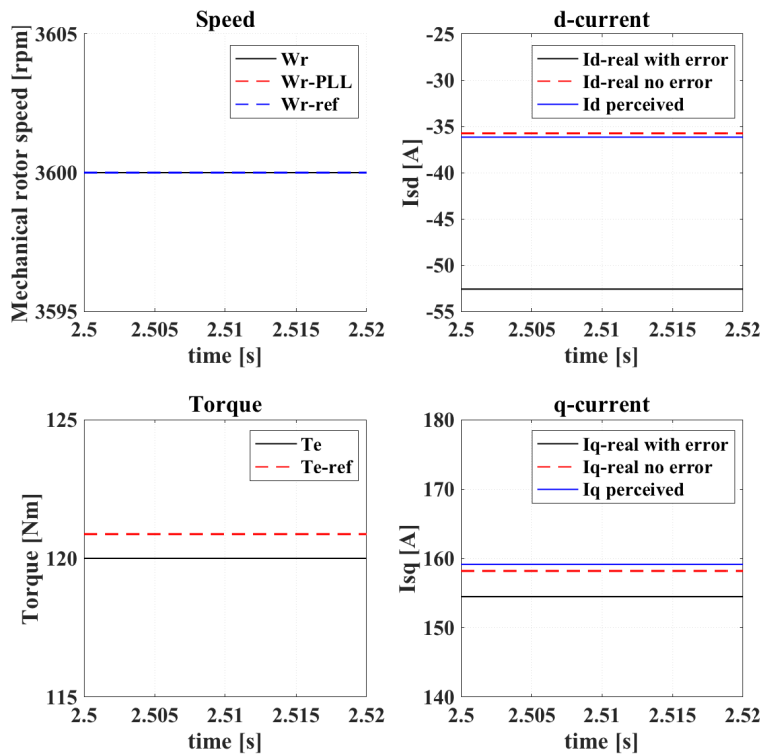


Figure 28: Simulation result of a 0.5 degree mechanical angle error offset.

In order to evaluate the effect of a negative angle offset, simulations with negative offsets were also performed. The resulting plot from a simulation with -0.5 mechanical degrees angle offset is presented in Figure 29. It can be observed that a negative offset result in the opposite case of a

positive offset and it was decided that simulations with only positive offsets would be sufficient for the offset error evaluation.

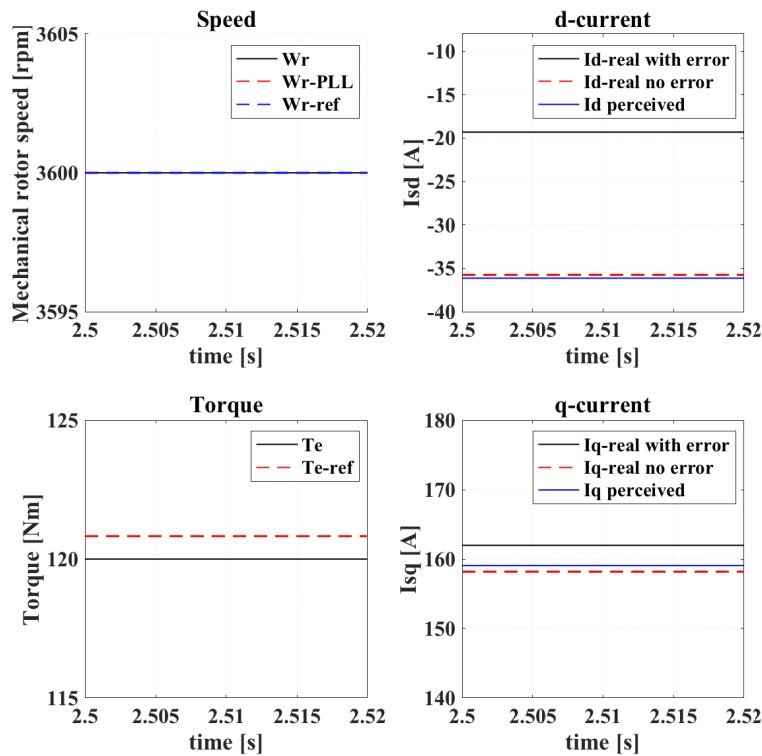
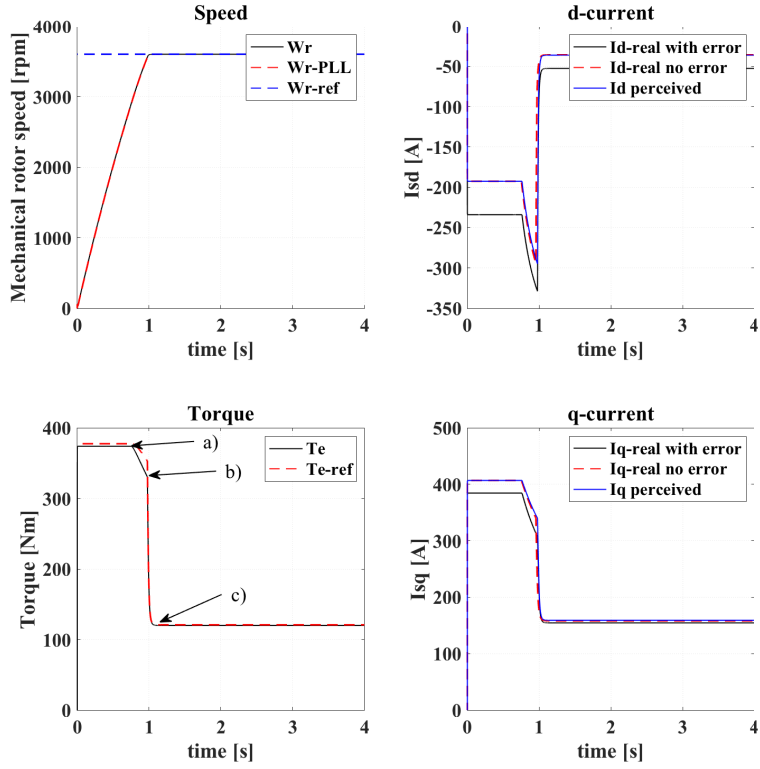
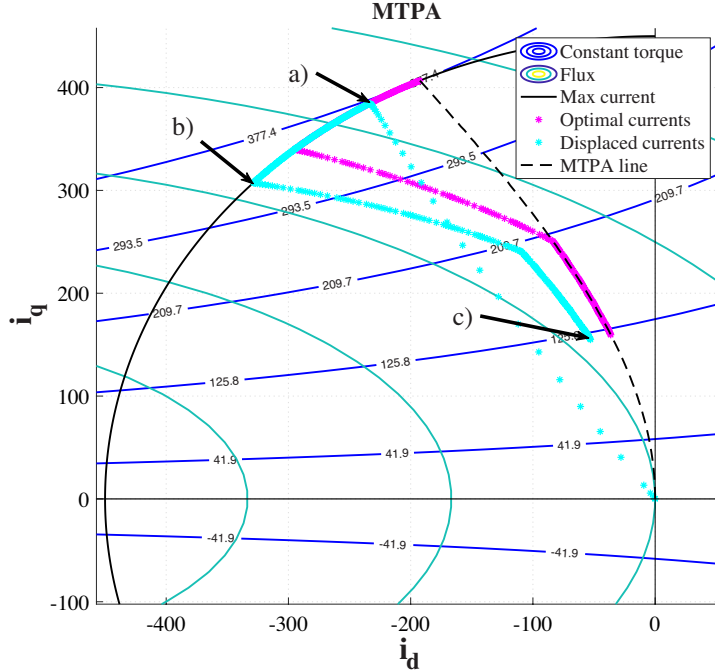


Figure 29: Simulation result of a -0.5 degree mechanical angle error offset.

The MTPA plot together with the full scale simulation for a 0.5 degree error angle is presented in Figure 30. The cyan colored asterisks are the displaced currents due to the 0.5 degree angle measurement error. It can be observed that especially the d-current is much higher than the optimal current represented by the magenta asterisks as previously discussed. Similar to the previous simulation without errors in Figure 26 the same control strategies decides the currents path from "a" to "c". The big difference however, is the displaced MTPA currents caused by the angle offset.



(a) System response with 0.5 degree mechanical angle error.



(b) Corresponding MTPA plot to the 0.5 degree mechanical angle error simulation.

Figure 30: System response and MTPA currents with 0.5 mechanical degrees angle error.

### 6.3 Discrete system measurement error effects

As the system was converted from continuous to discrete the simulation verifying correct sampling discussed in Section 5.3 resulted in Figure 31. This figure illustrates how the sampling is related to the duty cycle, carrier wave and the resulting phase voltage. It can be observed that the sampling is done every 0.1 ms which corresponds to a switching frequency of 10 kHz. The figure also verifies that once the carrier wave is bigger than the duty cycle, the output voltage is zero which indicates a working system.

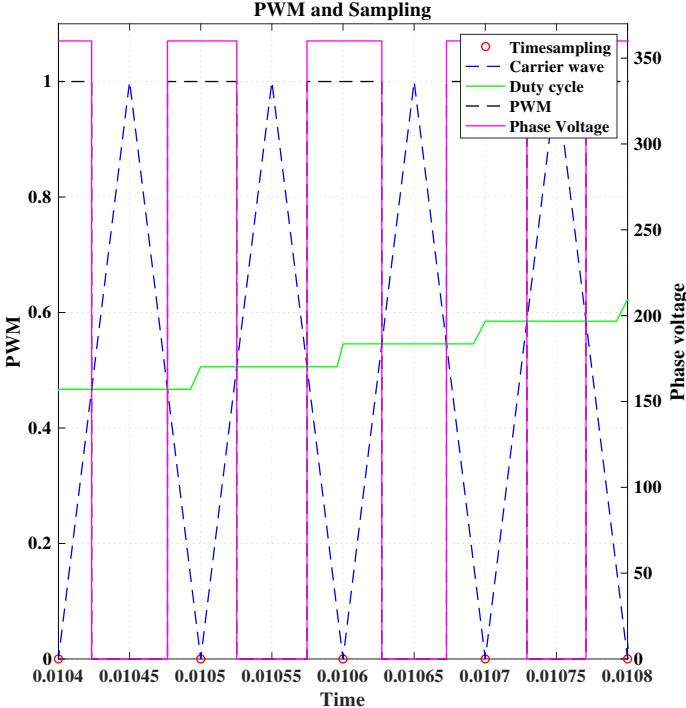


Figure 31: Sampling verification with a 10 kHz switching frequency.

With verified correct sampling, a simulation of the entire system was performed without implemented errors. This was done in order to verify the discrete system performance by comparing it to the continuous system performance. The result of the simulation is shown in Figure 32.

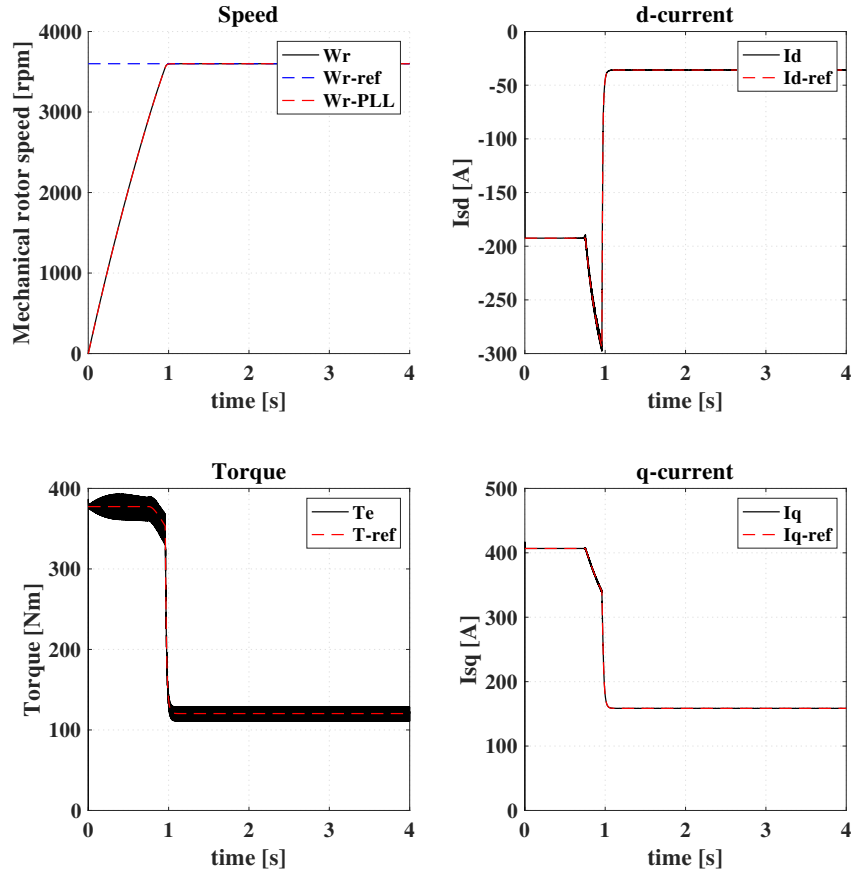


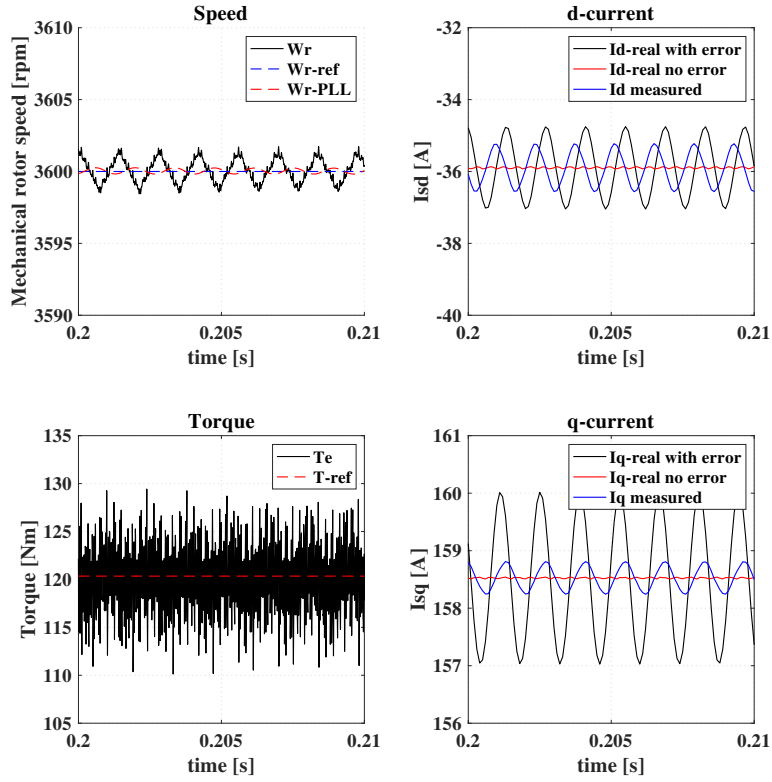
Figure 32: The response of the discrete system with a switching frequency of 10 kHz and without any error implementation.

It can be observed that the system operates similar to the continuous system in Figure 26 as it follows the references. This was an indication that the discrete system worked as expected and subsequently simulations with implemented errors could be performed. A first order step response was once again not observed due to the current limit. The presented currents in the figure are the sampled currents. It is observed that the discrete system without errors contains a torque ripple due to the PWM switching. The explanation for this is that the previously continuous AC signal being fed to the machine is a PWM DC-signal modulated with the switching frequency in the discrete system. The oscillations are observed as  $\pm 2.5$  Nm continuous with  $\pm 8$  Nm peaks during steady state operation. This does not however have the same effect on the speed because of the high frequency and in a sense filtering by the inertia of the machine. This is an acceptable torque ripple as it is below the constraint set by CEVT of  $\pm 5$  Nm with  $\pm 10$  Nm peaks.

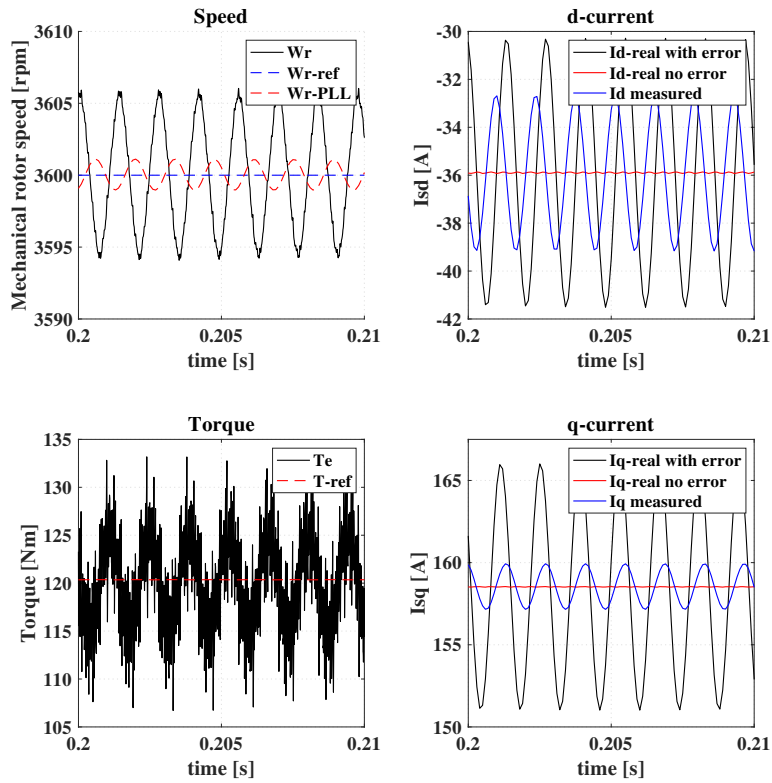
This simulation proved to be time demanding and thus the simulation time was reduced. It was at this point important to also reduce the inertia of the PMSM in order to reach steady state quicker because of the shorter simulation time. Because of this the value of the inertia was reduced to 0.002 for the upcoming simulations.

### 6.3.1 Current DC offset error effects in the discrete system

The parametric sweep of the phase current DC offset discussed in Section 5.4.1 was implemented and simulated. The result of the simulations for phase current DC offset magnitudes of 1 A and 5 A is presented in Figure 33. It can be observed that a phase current DC offset results in a torque ripple in the stator electrical frequency similar to the continuous system. It should also be mentioned that the artificially reduced inertia results in increased ripples in the speed. Another observation is that the measured current and the real current are phase shifted relative to each other. This shift is caused by the PI current controller as it is being fed a AC-signal since the DC offset becomes an AC signal when transformed into the dq-system.



(a) Phase a 1 A, Phase b 1 A, Phase c -1 A DC offset



(b) Phase a 5 A, Phase b 5 A, Phase c -5 A DC offset

Figure 33: System response of swept DC offset magnitude

The DC offset magnitude for the entire parametric sweep was plotted against the peak to peak (PTP) current and torque ripple. This presents a more perspicuous effect of the offset error. The plot is presented in Figure 34 where a linear relation between the DC offset and the resulting current and torque ripple can be observed. This is expected as the torque is directly proportional to the current magnitudes. It should be mentioned that the simulation without errors resulted in a PTP torque ripple of 5 Nm caused by the current ripple in the discrete system. However, the implemented DC offset causes a ripple in the electrical stator frequency thus introducing a different ripple than previously observed. Because of the fact that two ripples were observed, it was especially difficult to distinguish the torque ripple caused by the offset error for the 1 A offset case.

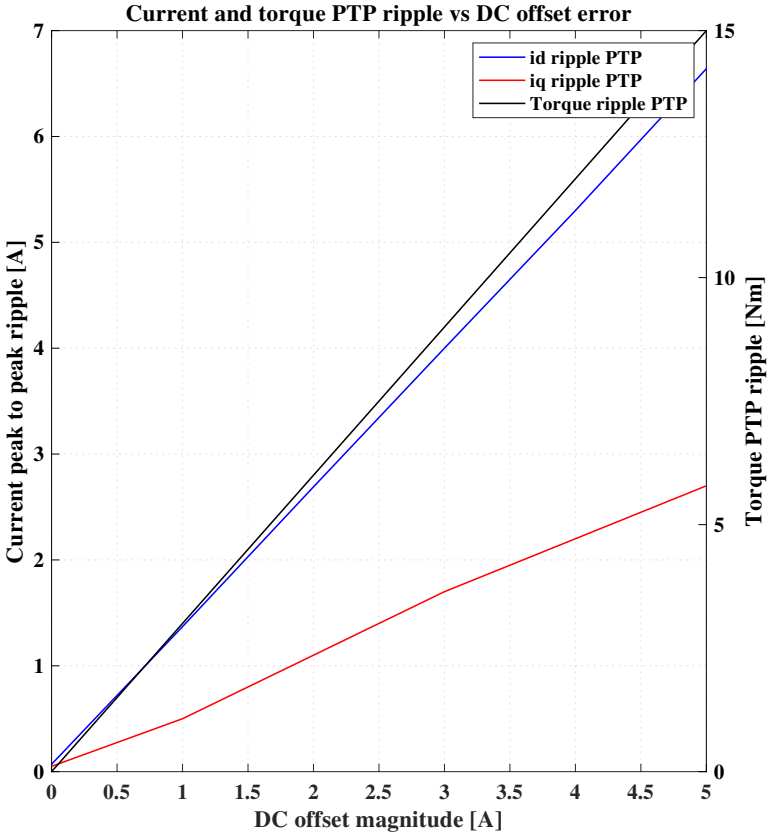
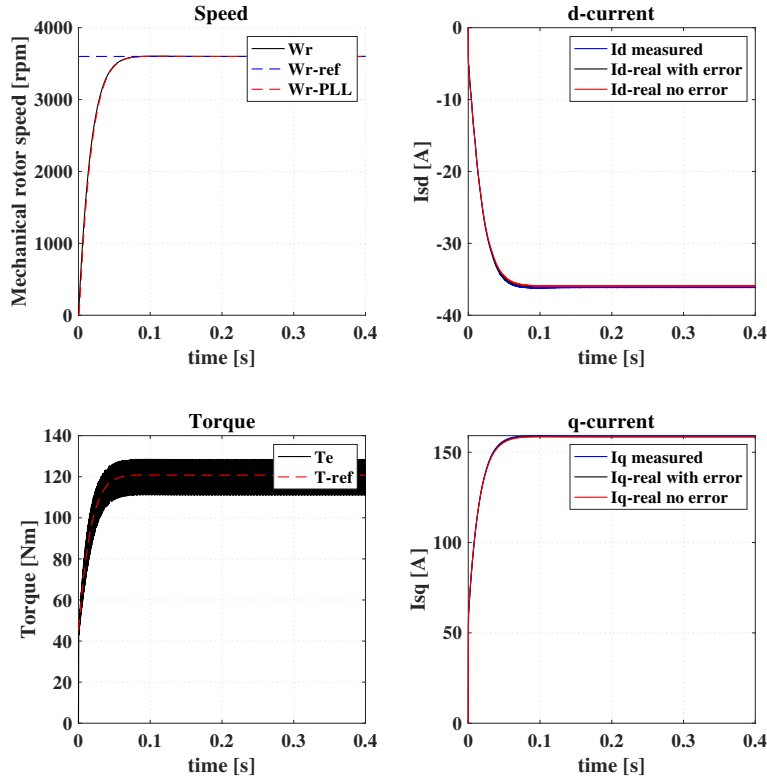


Figure 34: Current and torque ripple due to a DC current measurement offset.

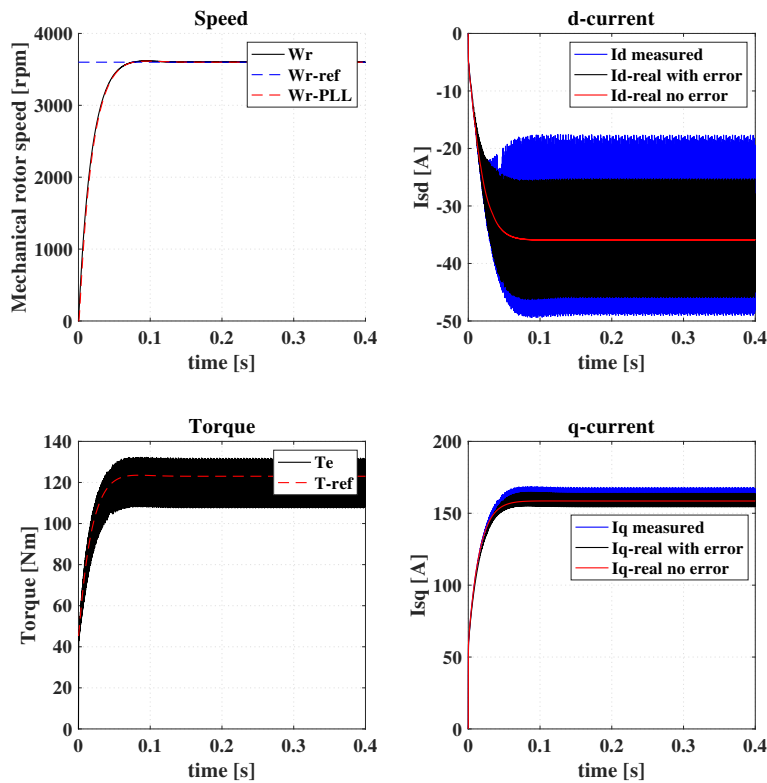
The resulting resistive power loss for the offset parametric sweep was calculated according to (11). However, since the DC offset only introduces a ripple in the currents the average current remains the same, and consequently no significant difference in power loss was observed.

### 6.3.2 Current sensor time delay effects

A simulation intended to visualize the effect of time delays in the current sensor was performed. This was done by sweeping the bandwidth of an implemented LPF according to Section 5.4.1. Figure 35 shows the simulation results with a LPF bandwidth of 25 kHz respectively 500 kHz. It can be observed that a lower LPF bandwidth in the current sensor, which corresponds to a increased time delay, increases the current ripple and consequently the ripple in the torque. This is caused by the current controller as it tries to drive the erroneous current signal caused by the time delay to the current reference. The controller does not know about this delay and sees it as a disturbance. As the controller tries to eliminate this disturbance, it results in a ripple which increases with increased time delay.



(a) Sensor LPF bandwidth of 500 kHz.



(b) Sensor LPF bandwidth of 25 kHz.

Figure 35: : Impact of different LPF bandwidths in the current sensor representing sensor time delays.

Once again the PTP ripple in currents and torque, caused by the error, was plotted against the bandwidth parameter sweep between 0-500 kHz. This resulted in Figure 36 which indicates that the effect of LPF bandwidths below 100 kHz have a significant impact on the torque ripple.

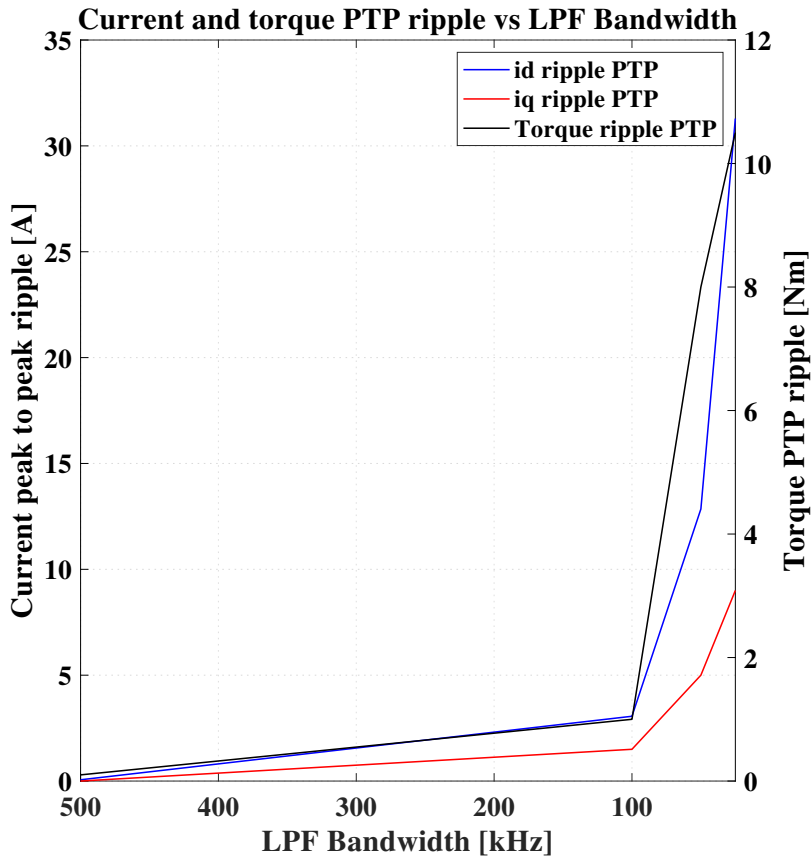
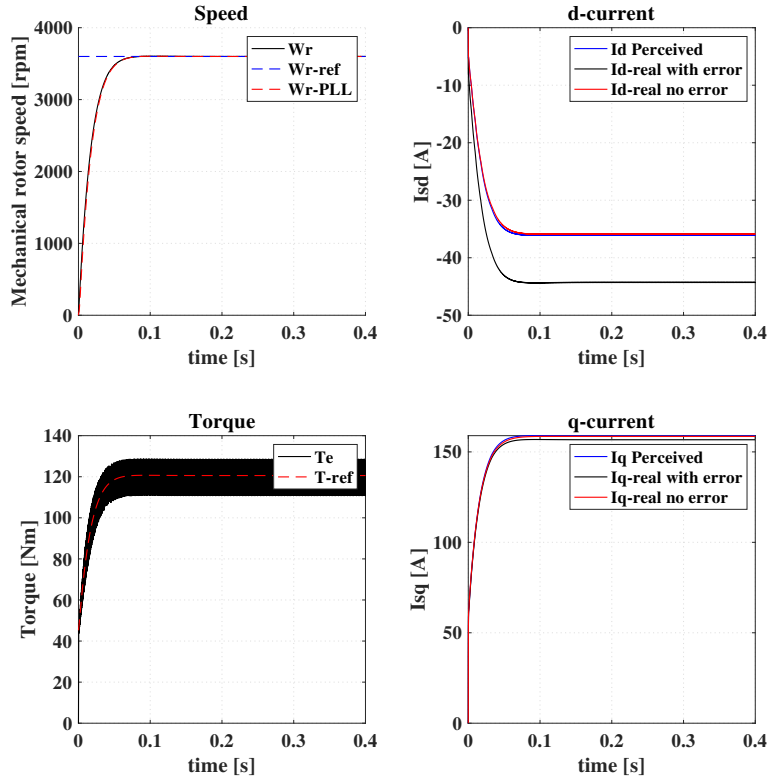


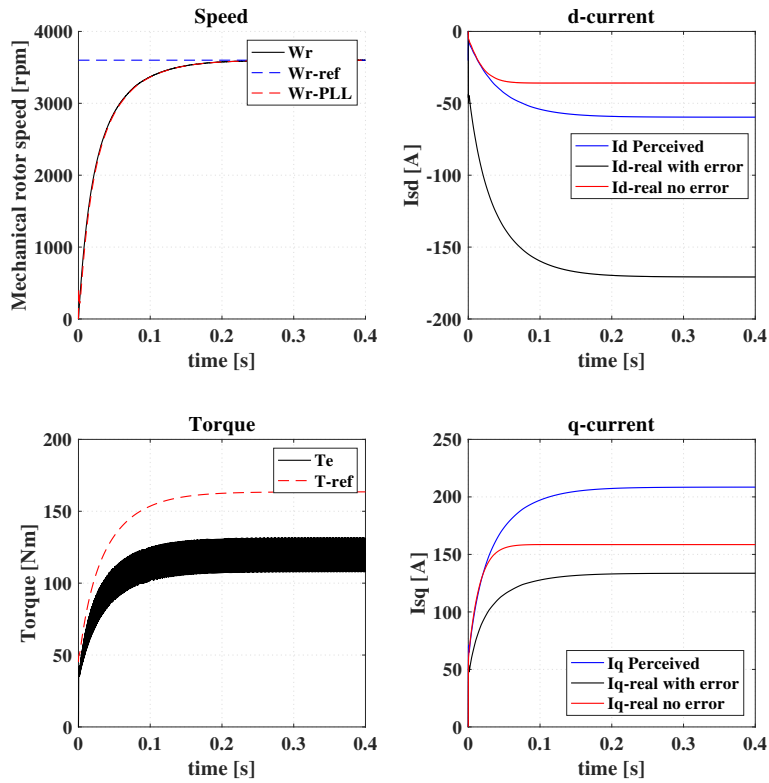
Figure 36: Current and torque PTP ripple due to current sensor time delays.

### 6.3.3 Effect of position angle offset error in the discrete system

The position sensor offset error was simulated according to Section 5.4.2. Simulations with 0.25 and 3 mechanical degrees offset resulted in Figure 37. These offset angles can be converted to 3 respectively 24 electrical degrees by multiplying with the number of pole pairs. It can be observed that a offset value in the position sensor increases the current vector. The currents are affected similarly to how the continuous system was affected. This is expected as discussed in 5.4.2 and according to (3) as the currents have increased for the same requested operating point.



(a) Position sensor offset error of 0.25 mechanical degrees.



(b) Position sensor offset error of 3 mechanical degrees.

Figure 37: Position sensor angle offset error of 0.25 respectively 3 mechanical degrees.

The parametric sweep of mechanical degrees offset error discussed in 5.4.2 resulted in Figure 38. Here the currents as a function of the offset error is plotted. It can be observed that increased magnitude of the dq-current vector, plotted in black, is the result of the increased position angle error. The figure also illustrates both  $i_d$  and  $i_q$  in blue and red respectively.

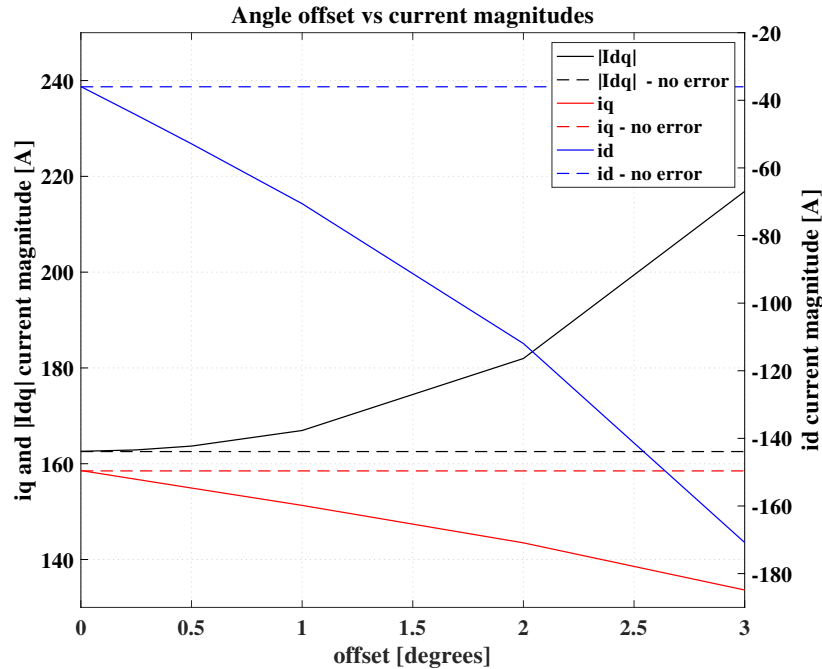


Figure 38: Increased current magnitude due to position angle offset error.

The resistive power loss in the machine was calculated according to (11). A simulation without errors resulted in a resistive power loss of 396 W. With implemented errors the power loss increases in accordance to Table 3. The table shows the increase in power loss in percentage for the parametric sweep of the angle offset error. As the current increases exponentially with the error and the power is calculated as (11) the impact of the error rapidly becomes critical with the increased error.

Table 3: The increased resistive power loss in the machine due to angle measurement offset errors.

Offset Error (Mechanical degrees)	Increased resistive power loss (Watt)	Percentally increased power loss (%)
0.25	2	0.5%
0.5	6	1.5%
1	22	5.5%
2	101	25.5%
3	309	78%

Similar to the continuous system, the MTPA currents can be plotted in order to visualize that the measurement error result in a less efficient current vector. The 1 mechanical degree error offset was once again simulated where the result this time is presented in a MTPA plot presented in Figure 39. The resulting Cyan colored currents are compared with the optimal magenta colored MTPA currents for the same operating point. It is observed that the error causes the current vector to be displaced from the the optimal values.

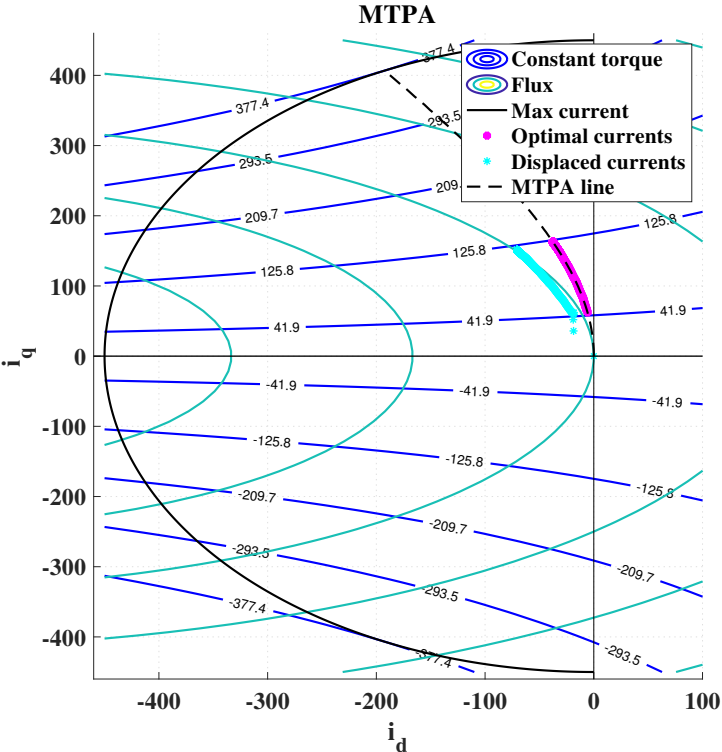
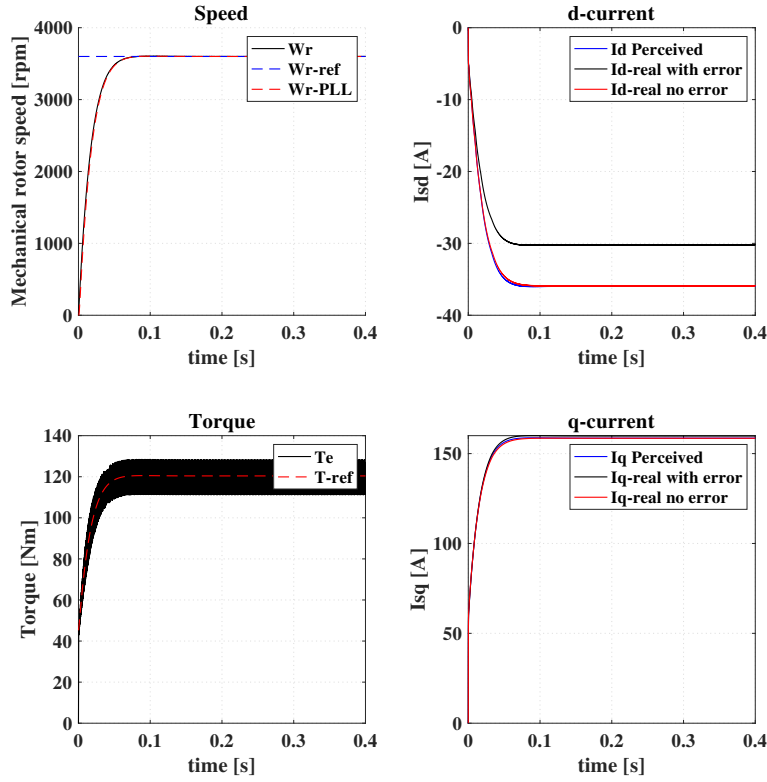


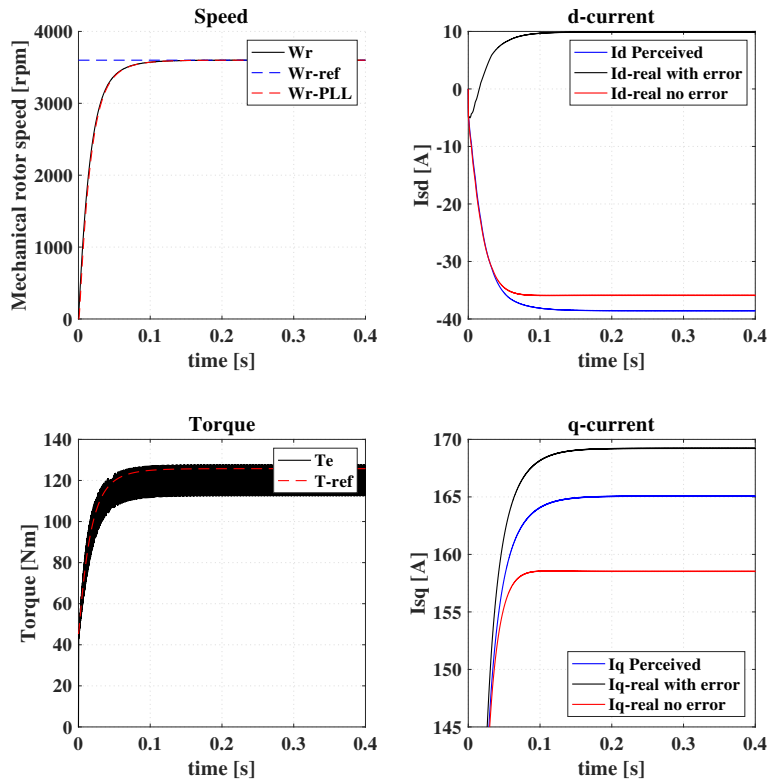
Figure 39: MTPA currents with a 1 mechanical degree position offset.

### 6.3.4 Position sensor time delay effects

Simulations showing the effect of time delays in the position sensor are presented in Figures 40a and 40b with LPF bandwidths of 20 and 2.5 kHz respectively. It can be observed that the effect of a low LPF bandwidth, representing a longer time delay, looks similar to a negative angle offset. The 20 kHz simulation correspond to -0.17 mechanical degrees angle offset whereas the 2.5 kHz simulation correspond to an angle offset of -1.38 mechanical degrees. The current vector deviates from the ideal MTPA current line, but this time in opposite direction to that of a positive angle offset.



(a) Position sensor LPF bandwidth of 20 kHz.



(b) Position sensor LPF bandwidth of 2.5 kHz.

Figure 40: Impact of different LPF bandwidths in the position sensor representing sensor time delays.

Similar to the parametric sweep of the angle offset error the sweep of different position sensor time delays was plotted against the resulting currents. This plot is presented in Figure 41 from which it easily can be concluded that an increased time delay, represented by a lower LPF bandwidth, results in increased current magnitudes.

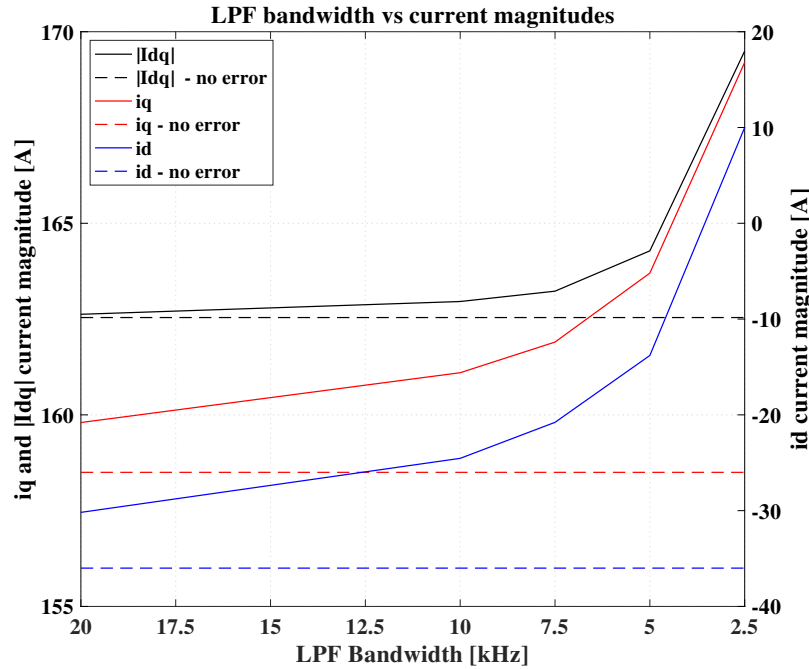


Figure 41: Increased currents due to position sensor time delays.

Since the result of a time delay in the position sensor translates to an offset in the current vector, the increased power losses was again calculated and is presented in Table 4. The current does once again increase exponentially with the error which with the power loss calculation rapidly makes the impact of the error critical.

Table 4: The increased resistive power loss in the machine for different position sensor LPF bandwidths representing time delays.

LPF bandwidth [kHz]	Time delay [ $\mu$ S]	Increased power loss [W]	Percentual increased power loss (%)
20	110	0.51	0.13%
10	220	2.3	0.58%
7.5	293	3.8	0.95%
5	440	8.4	2.1%
2.5	880	35.12	8.9%

As discussed the effect of an increasing time delay is similar to the effect of negative angle offset. This is easily observed in Figure 42 which shows the MTPA currents with the 2.5 kHz bandwidth LPF in the position sensor which now deviates in the opposite direction.

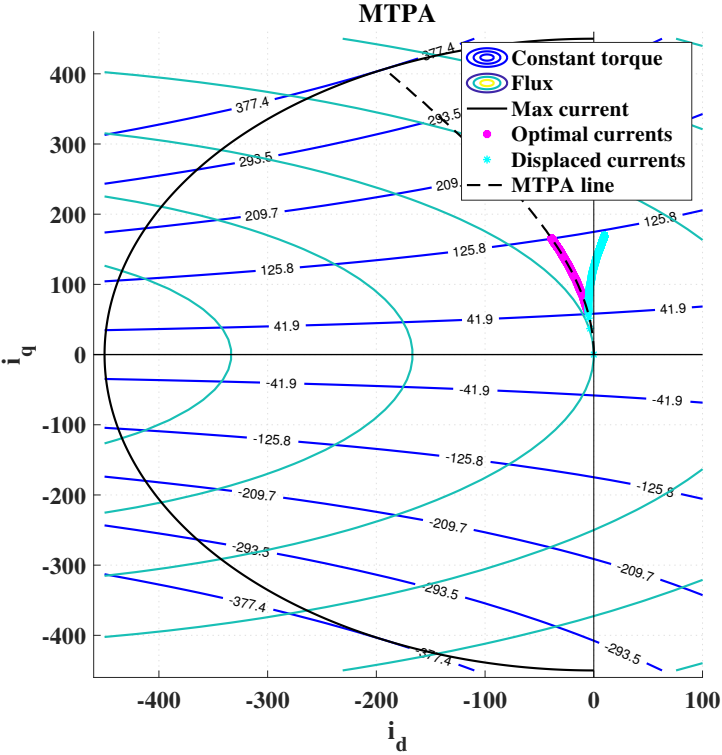


Figure 42: MTPA currents with a 2.5 kHz LPF in the position sensor.

### 6.3.5 Combined error effects in the discrete system

As discussed in Section 5.4.3, an implementation of combined sensor errors results in a more realistic system behavior. Simulations were performed according to Section 5.4.3 with the error parameters presented in Table 2. The first simulation was performed with the most optimal parameters and resulted in Figure 43. It can be observed that these error parameters result in a close to negligible increase of the current magnitude. However, the torque ripple increased close to the constraint with the combined optimal error parameters simulated simultaneously.

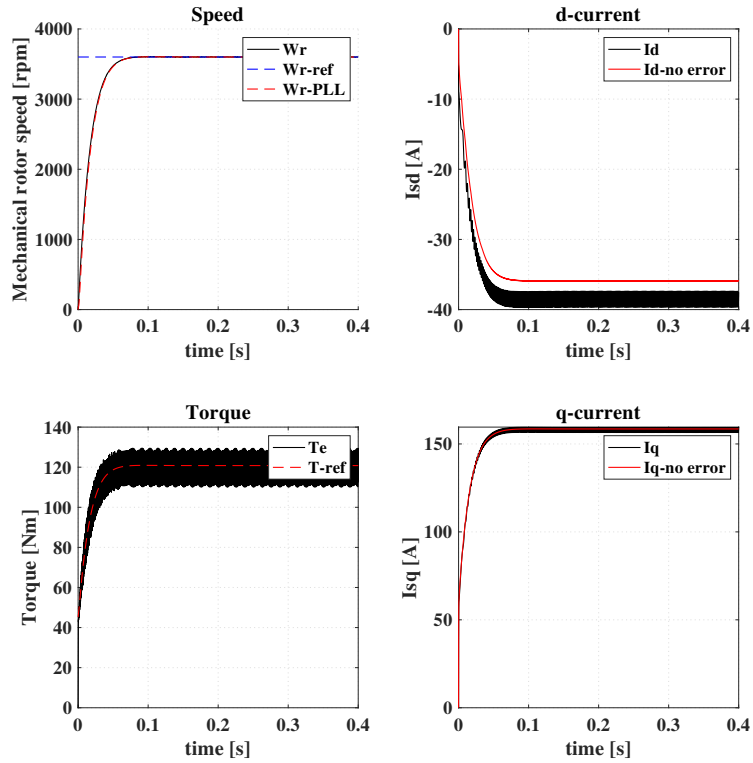


Figure 43: The optimal investigated error parameters implemented simultaneously.

Following simulation was the realistic case in Table 2 which resulted in Figure 44. It can be observed that the errors now start to have a noticeable impact on the system both regarding the torque ripple and increased current magnitude.

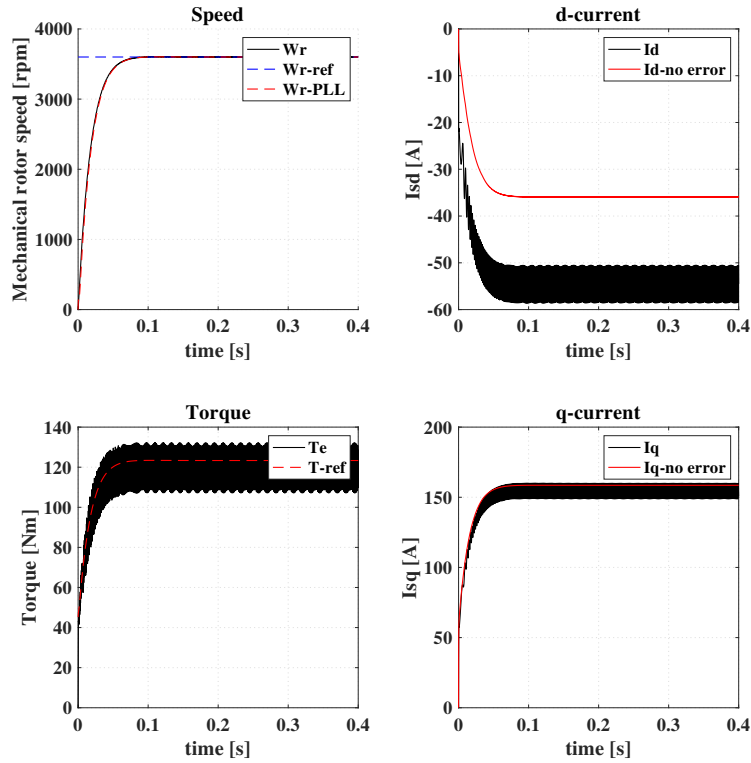


Figure 44: Scenario of acceptable errors with all investigated errors implemented simultaneously.

The simulation with the worst case parameters in Table 2 resulted in Figure 45. It can be observed that the system sees large ripples in the currents and consequently the torque. An important observation is that the currents are lower than the solely 3 degree angle offset simulation presented in Figure 37b. This indicates that a position angle offset error and position sensor time delay cancel each other out. This is expected as it previously have been concluded that a time delay have the same effect as a negative angle offset.

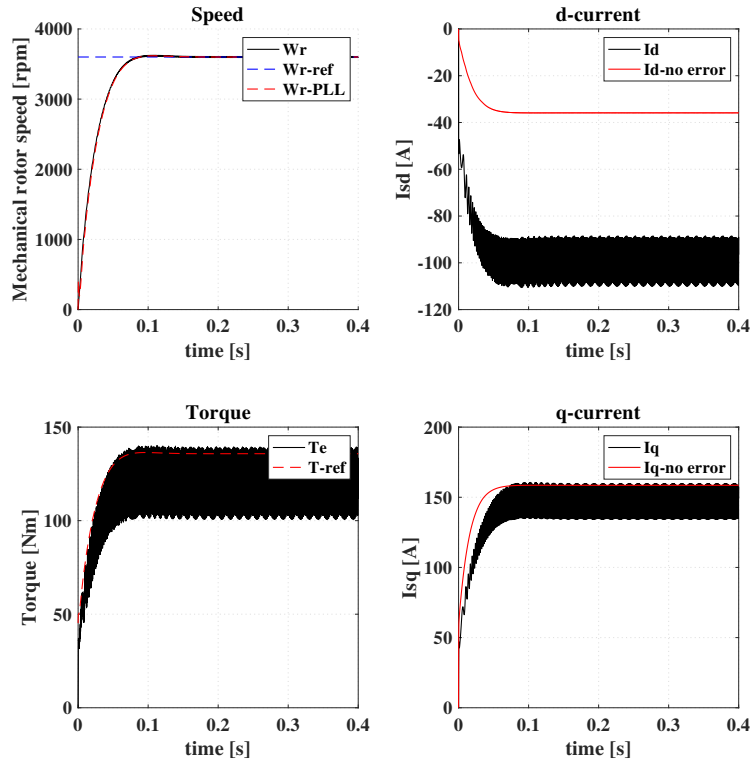


Figure 45: Scenario of all the worst case error parameters implemented simultaneously.

The torque of the three different cases was plotted against each other. This clearly visualizes the difference in torque ripple depending on the implemented error parameters. This plot resulted in Figure 46 which clearly illustrates that the torque ripple is significantly increased with suboptimal error parameters.

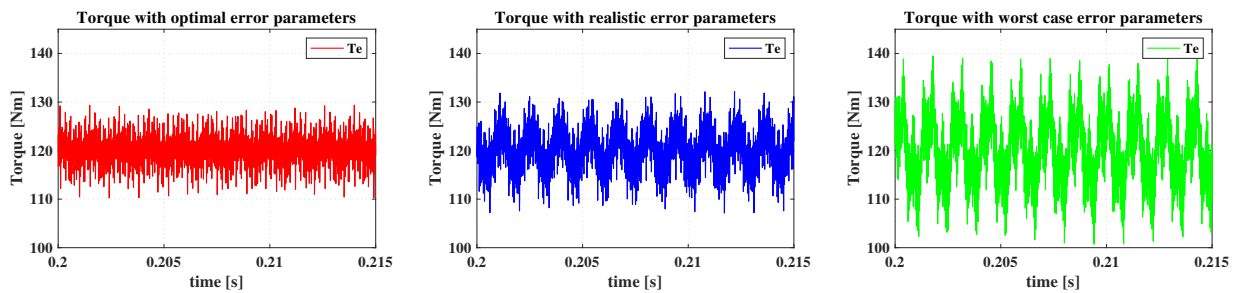


Figure 46: Torque comparison of the three simulated combined error scenarios.

The resulting increase in power loss for the three scenarios compared to the no error power loss was calculated and is presented in Table 5.

Table 5: The increased resistive power loss in the machine for different scenarios of implemented combinations of sensor errors.

Scenario	Resulting increased power loss [Watt]	Percentual increased power loss (%)
Optimal parameters	8.2	2%
Realistic parameters	19.1	4.8%
Worst case parameters	91.5	23.1%

As previously discussed the effect of a positive position angle offset and a position sensor time delay cancel each other out. Because of this fact, a simulation with combined errors where the position offset angle is negative is of interest. Such simulation was performed and resulted in Figure 47. Comparing Figure 43 and Figure 47 it can be observed that the currents have increased which indicates that the position sensor errors amplify each other if a negative offset angle is implemented.

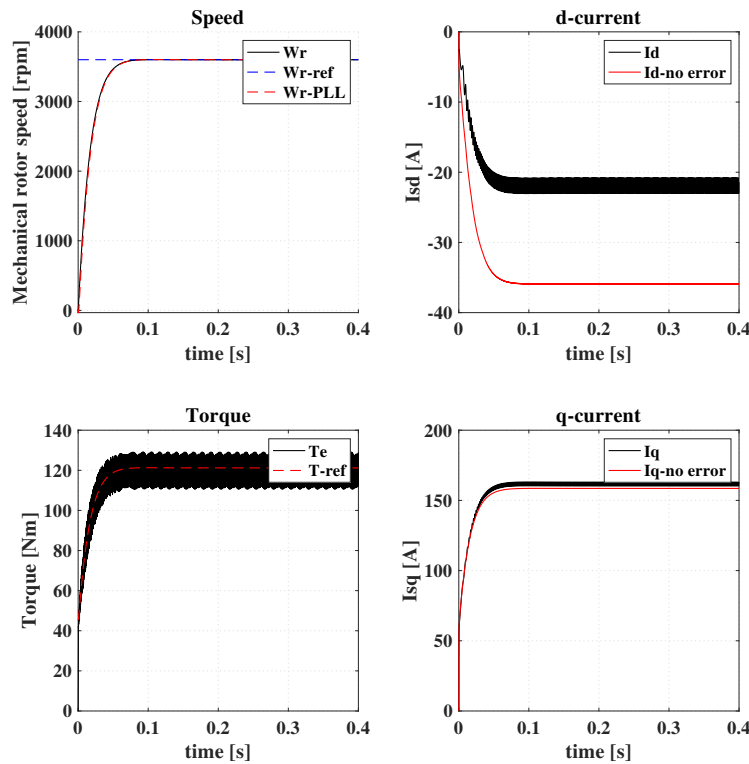


Figure 47: Scenario of all the optimal error parameters implemented simultaneously, but with a negative offset angle.

## 6.4 Sensor technologies comparison matrices

The applicable sensor technologies for PMSM's used in vehicle applications, presented in Section 3 and Section 4 proved to possess various advantages and disadvantages. This section presents a comparison of the different technologies. This was performed according to Section 5.5 as the properties of all the investigated technologies was summarized and presented in Table 6 and 7.

### 6.4.1 Current sensor technologies comparison

The investigated sensor technologies was evaluated according to Section 5.5. The resulting main attributes of interest is presented in Table 6.

Table 6: Current sensor technologies matrix.

<b>Sensor tech</b>	<b>Adv.</b>	<b>Disadv.</b>	<b>Accuracy</b>	<b>Bandwidth</b>
<b>Shunt</b>	-Reliable and simple -Cheap	-No galvanic isolation -Risk for permanent damages -Thermal drift -High power losses	0.1-0.5%	kHz-MHz
<b>Hall-OL</b>	-Galvanic isolation -Lower power consumption than Hall-CL -Cheaper than Hall-CL -Small size	-Limited by core saturation -Sensitive to external magnetic fields	2-3%	25 kHz
<b>Hall-CL</b>	-Galvanic isolation -Accurate & noise immune	-Expensive -Secondary current power consumption -Core saturation limited	>0.5%	200 kHz
<b>AMR</b>	-Galvanic isolation -More accurate than Hall -High reliability -Small weight and size	-Expensive -Higher power loss than Hall at high currents -Limited frequency response due to skin effect	0.5-2%	>500 kHz

### 6.4.2 Position sensor technologies comparison

Similar to the comparison of current sensor technologies, the attributes of the investigated position sensors in Section 4 is compared in Table 7. The incremental encoder was quickly dismissed as an option for use in vehicles. The main motivation behind this was because it can be

regarded as a big safety concern due to its unreliable performance. If a pulse in the measurements is missed by the encoder which is likely in the harsh environment of a vehicle, a significant error in the angle readings will be produced. The main attributes of the sensors according to Section 5.5 was compiled and is presented in Table 7.

Table 7: Comparison of attributes of the position sensor technologies.

Sensor Technology	Advantage	Disadvantage
Optic Encoder	-Very high resolution -High accuracy	-Sensitive to particles, dust and condensation -Unreliable in harsh environment -Limited working temperature range
Capacitive Encoder	-High resolution -High accuracy	- Sensitive to temperature, humidity, foreign matter and vibration. -Not well suited for harsh environment -Difficult mechanical installation
Inductive Encoder	-High accuracy -High resolution -Robust -Cheaper than Resolver -Easy to install -Compact -Lightweight	-Relatively new technology, thus not widely available. -Limited sources which investigates deeper on its performance
Resolver	-High Accuracy -High Resolution -Robust	-High system cost -Bulky -Heavy -Large installation space requirement

From the knowledge in Section 4, a further comparison between the resolver and the inductive encoder is presented in Table 8.

Table 8: Comparison of attributes presented in theory between Resolver versus Inductive Encoder.

Property	Resolver	Inductive Encoder
Ability to work in harsh environments	X	X
Resilience to electrostatic effects	X	X
High Resolution	X	X
High Accuracy	X	X
Easy installation		X
Economical		X
Lightweight		X
Compact		X

# 7

## Discussion

In this Chapter, the presented results are further discussed. It also contains a discussion regarding the comparison of different sensor technologies. Additionally, suitable technologies for vehicle applications that can satisfy the needs of the DHT being developed at CEVT are discussed together with recommendations.

### 7.1 Current sensor simulation

As observed in section 6.3.1, the simulations of a phase current DC offset resulted in a current ripple with the stator electrical frequency. This was consequently translated to a similar ripple in the torque and thus also in the speed. The specification provided by CEVT required a maximum continuous torque ripple of  $\pm 5$  Nm. Looking at Figure 33a, a 2.5 Nm torque ripple was observed when no error was applied which was caused by the PWM switching as previously explained. However, with the DC offset applied in Figure 33b a continuous torque ripple of  $\pm 7.5$  Nm was observed. To be within the constraint of  $\pm 5$  Nm, the DC offset should not exceed 3.5 A according to Figure 34 as this value corresponds to a PTP torque ripple of 10 Nm. As CEVT existing specification on the DHT current sensors is  $\pm 5$  A, it is recommended that further investigations of these specifications are conducted. It should although be consider how the torque ripple manifests itself in the speed output since it depends on the inertia of the machine. If the inertia is high, a high frequency torque ripple will not have a significant effect on the speed, whereas a low inertia would result in significant ripple in the speed.

From Figure 35 it was observed that introducing a time delay in the current sensor resulted in an increased current ripple. As seen in Figure 36 the effect of a time delay starts to have a significant impact when going below 100 kHz which corresponds to a delay of 22  $\mu$ s. However, it can be observed that none of the simulated time delays resulted in a torque ripple which exceeds the constraint of  $\pm 5$  Nm, but it does however exceed the constraint of  $\pm 10$  Nm peaks. It should be mentioned that it was difficult to distinguish the increased torque ripple due to the time delay from the ripple seen without errors. Because of this fact the interpreted numerical values can be questioned.

In conclusion it is recommended that physical testing of current sensors is conducted in order to verify the presented impacts of the measurement errors.

## 7.2 Position sensor simulation

During the simulation stage it was observed that a constant offset angle measurement error resulted in an unaffected speed estimation by the PLL. This is corroborated by the theory presented in Section 2.2.3 which states that the speed is the derivative of the angle and this is valid regardless of shift in the angle. Thus the speed controller is being fed the actual value of the speed. However, as can be seen in Figure 37a and 37b, a constant angle offset will introduce a suboptimal current vector as presented in Figure 39. A positive constant angle error results in a current vector consisting of increased negative d-current, and a reduced q-current. The speed controller will therefore increase the torque reference, which in turn increases the current, in order to achieve the torque required to drive the vehicle to the requested speed.

Introducing the error in the position angle measurement, it is important to mention that this is an error in mechanical degrees. This means that the error is much bigger when converted to electrical degrees which is done by multiplying with the number of pole pairs. A measurement error of one mechanical degree would consequently result in an error of 12 electrical degrees for a PMSM with 12 pole pairs. The important conclusion is that a PMSM with many poles is more sensitive to angle measurement errors.

It can be observed in Figure 38 that offset current magnitude increases significantly faster when approaching 1 degree measurement error and above. It is also seen from the calculated power loss in Table 3 that the power loss increases significantly when going above this angle offset error. An important conclusion to draw from this result is that the accuracy of the sensor should not have an error larger than somewhere between 0.5-1 mechanical degrees depending on how much is considered as an acceptable loss for the system.

An introduced time delay in the position sensor was concluded to act as a negative angle offset. This can be observed by comparing Figure 29 with Figure 40 which corresponds to a negative angle offset and an implemented time delay respectively. This was considered to be a reasonable conclusion. The position sensor measures a delayed angle whereas the actual angle, which should have been sent to the controller, has advanced to a new position. From Figure 41 and Table 4 it can be seen that the power losses start to increase significantly when going below 7.5 kHz.

### 7.3 Combined sensors simulation

The simulations of each sensor error implemented separately resulted in observations regarding the optimal, realistic and unacceptable error parameters. This resulted in the three combination of error parameters presented in Table 2.

It was through the simulations of these combined error parameters, implemented simultaneously, concluded that the previously presented effect of each error could be distinguished in the combined simulation plots. Regarding the torque ripple it was observed that the ripple from the phase current DC offset and current sensor time delay amplified each other. As observed in Figure 46 the constraint of  $\pm 5$  Nm continuous and 10 Nm PTP was almost exceeded already with the most optimal parameters implemented together. With the realistic parameters implemented simultaneously both of the torque constraints were exceed which was not the case with separately implemented realistic error parameters.

The combination of a constant measurement angle offset with a time delay in the position sensor resulted in a cancelling effect if the angle offset is positive. However with a negative angle offset, the effect of the error was amplified. This can be observed when comparing Table 5 and 3. Comparing the worst case scenario where the combined errors yielded a increased power loss of 91.5 W, whereas the increased power loss was 309 W with the solely implemented angle offset of 3 mechanical degrees.

### 7.4 Applicable current sensor technologies

During the extensive literature study of applicable current sensor technologies, several conclusions could be drawn. Many of the sources indicated that only a few of viable current technologies were suitable for usage in vehicle operation due to alternating factors. It was quickly realized that the industry does not use shunt based current sensors. This was also concluded from the fact that the power losses would be unacceptable for this high power application. Although galvanic isolation can be added which would reduce the losses, the cost of this would results in a more expensive sensor than the alternatives is explained in Section 3.1 [9]. The other investigated sensor technologies also proved to have several advantages over the shunt based technology and consequently it was disregarded during further investigation. These advantages can be observed in Table 6 where the most significant ones are the galvanic isolation and less thermal drift.

The Rogowski Coil could in a similar way be excluded from the sensor comparison at an early stage as it was concluded that this automotive application requires DC or close to DC measurements. When the motor operates at low speed the frequency is too low for the Rogowski Coil to be a viable current sensor. However, the study showed examples of a combination of sensor technologies where the Rogowski Coil could be utilized for accurate measurement at higher frequencies. This is a questionable solution as it would increase the complexity and the number of electronic components for the sensors to work smoothly together. This would in turn increase the size and make the sensor configuration more bulky which is undesirable in vehicle operation.

This meant that the two viable alternatives for further comparison were the Hall effect and AMR sensor. Looking at the attributes presented in Table 6 it is indicated that the AMR sensor would be the optimal choice. These sensors provide a larger bandwidth and better accuracy with few disadvantages.

It should however be mentioned that the attributes presented in Table 6 can be questioned. The table is constructed by information extracted from data sheets and technical reports. Few of these displayed sensor attributes for the particular operating conditions found in the DHT specifications. The sensor manufacturers also use different strategies of displaying the accuracy. Usually it is the worst case accuracy that is displayed and a common method is to display it as % FS which means percentage of full scale. An example of this is found in [31] which is a data sheet of an AMR sensor capable of measuring currents up to 1000 A with a total error of 2% FS meaning 20 A error during the total span of possible current measurements. Using this sensor in the DHT system would result in a 20 A error in the 500 A measurements which is not realistic and consequently this method of displaying an accuracy can be questioned. The conclusion of this is that in order to make the most optimal comparison of sensors the specific sensor requirements should be provided to a supplier which then can deliver a more precise sensor specification.

Considering the fact of the reliability of the comparison it was still concluded that the most promising sensor in terms of attributes and accuracy was the AMR sensor which is recommended for further investigation in the DHT project.

## **7.5 Applicable position sensor technologies**

When considering which sensor technology is most suitable to use in the DHT, one should understand the purpose of the component and the role it plays in the system as a whole. Safety is of paramount importance in a vehicle, and the sensor is an important puzzle piece in a safe vehicle. Both passengers and pedestrians need to be safe and not prone to danger of an unreliable vehicle. Therefore, a sensor technology which is robust and reliable must be chosen. As discussed in Section 1.5, the sensor also plays a role in the energy efficiency of the system. This is also seen in Table 3 where inaccurate measurement readings lead to added power losses in the system. Accurate readings are thus an important property in having a sustainable system.

In the comparison between different position sensor technologies, Table 7 shows the advantages versus the disadvantages with the four technologies. The optical and capacitive encoders are both good sensors, but they are both also very sensitive to their environment which makes them difficult to use in vehicle application where you can have an environment with a lot of dust and particles.

The resolver is a common type of sensor used today and is the type of sensor used at CEVT today. This is mainly due to its robust property along with the high accuracy and resolution. However, due to how the resolver works and consisting of heavy transformation coils, it is a very bulky system which causes it to take up a lot of space in the vehicle.

The inductive encoder is a technology with promising properties. As seen in Table 8, the inductive encoder has the benefits of the resolver, but without most of the disadvantages. The rotary inductive encoder is however a relatively new technology which makes this sensor not as widely available on the market as the resolver. The qualities of the sensor however makes it interesting to further investigate if it is a viable replacement to the resolver. There is although not as much literature as the resolver regarding this technology, it is therefore important to stay critical to the sources as the properties can sound skewed when there is not so much negative properties of the sensor being highlighted. At least until it can be verified by independent sources or through practical testing in future work.

## 7.6 Future work

The difference between simulation of combined optimal and worst error parameters are presented in Section 6.3.5. It could be concluded that a increased number of system components required a complex analysis of the simulations. Because of the countless combinations of the error parameters, errors from different sources can either add up or cancel each other out. The errors either amplify or mitigates the effect they have on the system. An example is to compare the result of a the 3 degree angle error in Figure 37b with the worst case scenario of combined errors in Figure 45. It can be observed that the power loss with only the position error is greater than the power loss of the combination of sensor errors with worst case parameters. However, for the worst case the torque ripple is significantly higher. This indicates that the errors cancel out each other regarding the current but amplifies each other regarding the torque once implemented simultaneously. The conclusion drawn from this example is that in order make a more accurate analysis, a more realistic model could be built. This should be done in order to make more accurate specifications of acceptable sensor error parameter values.

Regarding the position sensor technologies, it is encouraged to look deeper into the Inductive Encoder as an option to replace the currently used resolver at CEVT due to its qualities.

Using sensorless control and not having to deal with the cost and challenges of having a sensor measurement device in the system is appealing. To this day however it has been too difficult to deliver the correct torque from start position of the PMSM with stable and accurate measurement readings as discussed in Section 4.7. If sensorless control can be made to work, the advantages would be reduced cost, reduced hardware complexity and less maintenance requirements. It could however imply that an increased accuracy from the current sensors is required as it depends on input coming from the current sensor which would have to be considered. It is therefore a very interesting research topic to follow and be updated on with the hope that it can one day in the future be safely used in vehicles with reliable performance.

Throughout the thesis only one operating point has been under investigation. This was chosen as it was provided by CEVT and it was indicated that continuous operation were of interest to investigate. The number of test quickly grew and with several operating points the effect of each error would be difficult to display in a perspicuous way. It could however be of interest to evaluate the effect of sensor errors in a span of operating points which would resemble a typical driving scenario containing start from zero and high speed operation where field weakening have an impact.

The last interesting work to further look into would be to recreate the errors in real workbench testing. This would validate the conclusions drawn from the simulation results and provide the actual sensor properties.

# 8

## Conclusion

The main goal of this thesis was to evaluate the impact of position and current sensor errors for a PMSM used in automotive application. Additionally the main attributes of applicable sensor technologies was concluded and a perspicuous comparison was presented.

Simulations of a continuous and discrete PMSM system was performed. A current and position sensor containing modelled errors was implemented and simulated individually. It was concluded that an DC offset in the three phase currents as well as a time delay in the current sensor resulted in a current ripple. Consequently the torque experienced a ripple which exceeded the constraint of  $\pm 5$  Nm when the DC offset became larger than 3.5 A. The impact of the current sensor time delay did not cause the torque to exceed the torque constraint other than at peak spikes. However, the ripple increased significantly for bandwidths below 100 kHz in the LPF which represented the time delay.

A simulated offset and time delay of the rotor angle resulted in a suboptimal current vector. The requested operating point was reached but with a larger current vector and thus increased resistive power losses. It was concluded that the power losses experienced a significant increase above 1 mechanical degree offset and for LPF bandwidth lower than 7.5 kHz in the position sensor.

Simulations of combined current and position errors showed that the errors both negates and amplifies each other depending on the error combination. Simulation of the observed worst case error parameters implemented simultaneously resulted in a reduced current vector while the torque ripple was increased. A conclusion drawn from these simulations was that the complexity of the error analysis increases with the number of error sources. In order to perform a most accurate analysis, the model should be as realistic as possible.

Regarding the comparison of applicable sensor technologies for the DHT project, it was concluded that an AMR current sensor and an Inductive Encoder position sensor showed promising attributes. The AMR current sensor provides a better accuracy and bandwidth than the alternatives and have few disadvantages. The properties of the Inductive Encoder have the benefits of the commonly used resolver, but without many of the resolver's disadvantages. It is therefore recommended that further investigation is conducted regarding possible replacement of the currently used resolver with the Inductive Encoder.

# References

- [1] *Global Car Industry Must Shift to Low Carbon to Survive - CDP | UNFCCC*. [Online]. Available: <https://unfccc.int/news/global-car-industry-must-shift-to-low-carbon-to-survive-cdp>.
- [2] S. Bakker and J. Farla, "Electrification of the car – Will the momentum last?: Introduction to the special issue", *Environmental Innovation and Societal Transitions*, vol. 14, pp. 1–4, Mar. 2015, ISSN: 2210-4224. DOI: 10.1016/J.EIST.2014.07.002. [Online]. Available: <https://www.sciencedirect.com/science/article/pii/S2210422414000604>.
- [3] *What's Driving The Move To Electric Vehicles?* [Online]. Available: <https://www.forbes.com/sites/kensilverstein/2016/10/13/whats-driving-the-move-to-electric-vehicles/>.
- [4] R. Czerwinski and T. Rudnicki, "Examination of electromagnetic noises and practical operations of a PMSM motor driven by a DSP and controlled by means of field oriented control", *Elektronika ir Elektrotechnika*, 2014, ISSN: 13921215. DOI: 10.5755/j01.eee.20.5.7099.
- [5] *Home | CEVT*. [Online]. Available: <https://www.cevt.se/>.
- [6] M. Johansson, "Evaluation of Sensor Solutions & Motor Speed Control Methods for BLDCM/PMSM in Aerospace Applications", 2017. [Online]. Available: <http://ltu.diva-portal.org/smash/record.jsf?pid=diva2%3A1065318&dswid=7684>.
- [7] Jens Gächter, "Evaluation of Rotor Position Sensor Characteristics and Impact on Control Quality of Permanent Magnet Synchronous Machines", PhD thesis, Graz University of Technology, 2017, p. 145.
- [8] M. Kim, S.-K. Sul, and J. Lee, "Compensation of Current Measurement Error for Current-Controlled PMSM Drives", *IEEE Transactions on Industry Applications*, vol. 50, no. 5, pp. 3365–3373, Sep. 2014, ISSN: 0093-9994. DOI: 10.1109/TIA.2014.2301873. [Online]. Available: <http://ieeexplore.ieee.org/document/6717990/>.
- [9] S. Ziegler, R. C. Woodward, H. H.-C. Iu, and L. J. Borle, "Current Sensing Techniques: A Review", *IEEE Sensors Journal*, vol. 9, no. 4, pp. 354–376, Apr. 2009, ISSN: 1530-437X. DOI: 10.1109/JSEN.2009.2013914. [Online]. Available: <http://ieeexplore.ieee.org/document/4797906/>.
- [10] A. Bouabana and C. Sourkounis, "A low-cost current sensor with a novel modulated interface (F-PWM)", in *2010 17th IEEE International Conference on Electronics, Circuits and Systems*, IEEE, Dec. 2010, pp. 802–806, ISBN: 978-1-4244-8155-2. DOI: 10.1109/ICECS.2010.5724634. [Online]. Available: <http://ieeexplore.ieee.org/document/5724634/>.
- [11] A. Lidozzi, L. Solero, F. Crescimbin, and A. Di Napoli, "SVM PMSM Drive With Low Resolution Hall-Effect Sensors", *IEEE Transactions on Power Electronics*, vol. 22, no. 1, pp. 282–290, Jan. 2007, ISSN: 0885-8993. DOI: 10.1109/TPEL.2006.886603. [Online]. Available: <http://ieeexplore.ieee.org/document/4052420/>.

- [12] S. Larqvist and H. Östergren, “Electric Machine Comparison for Mild Hybrid Light Vehicles with Respect to Performance and Thermal Capability”, Tech. Rep. [Online]. Available: <http://publications.lib.chalmers.se/records/fulltext/252782/252782.pdf>.
- [13] L. Harnefors, *Control of variable-speed drives*. Västerås: Applied Signal Processing and Control, Department of Electronics, Mälardalen University, 2002.
- [14] S. Kim, Y.-D. Yoon, S.-K. Sul, and K. Ide, “Maximum Torque per Ampere (MTPA) Control of an IPM Machine Based on Signal Injection Considering Inductance Saturation”, *IEEE Transactions on Power Electronics*, vol. 28, no. 1, pp. 488–497, Jan. 2013, ISSN: 0885-8993. DOI: 10.1109/TPEL.2012.2195203. [Online]. Available: <http://ieeexplore.ieee.org/document/6186830/>.
- [15] S. Björkman and A. Dahlin, “Electric Drive Speed Control for Varying Moment of Inertia A Model Reference Adaptive Control Approach for Handling Changing Motor Dynamics”, Tech. Rep. [Online]. Available: [http://publications.lib.chalmers.se/records/fulltext/250406/250406.pdf?fbclid=IwAR001JIfG\\_NqwanL1TKTomUTDye9-IRhSCxvadu693yK0GBtZb5gi2MDlIs](http://publications.lib.chalmers.se/records/fulltext/250406/250406.pdf?fbclid=IwAR001JIfG_NqwanL1TKTomUTDye9-IRhSCxvadu693yK0GBtZb5gi2MDlIs).
- [16] “Field Oriented Control of Permanent Magnet Synchronous Motors User’s Guide”, Tech. Rep. [Online]. Available: [https://www.microsemi.com/document-portal/doc\\_view/130909-sf-foc-pmsm-hall-ug](https://www.microsemi.com/document-portal/doc_view/130909-sf-foc-pmsm-hall-ug).
- [17] M. Marufuzzaman, M. B. I. Reaz, L. F. Rahman, and T. G. Chang, “High-Speed Current  $dq$  PI Controller for Vector Controlled PMSM Drive”, *The Scientific World Journal*, vol. 2014, pp. 1–9, 2014, ISSN: 2356-6140. DOI: 10.1155/2014/709635. [Online]. Available: <https://www.hindawi.com/journals/tswj/2014/709635/>.
- [18] A. A. Abd Samat, M. Zainal, L. Ismail, W. S. Saidon, and A. I. Tajudin, “Current PI-Gain Determination for Permanent Magnet Synchronous Motor by using Particle Swarm Optimization”, *Indonesian Journal of Electrical Engineering and Computer Science*, vol. 6, no. 2, p. 412, May 2017, ISSN: 2502-4760. DOI: 10.11591/ijeecs.v6.i2.pp412-421. [Online]. Available: <http://iaescore.com/journals/index.php/IJECS/article/view/7376>.
- [19] *Permanent magnet synchronous machine current controller - Simulink - MathWorks Nordic*. [Online]. Available: [https://se.mathworks.com/help/physmod/sps/ref/pmsmcurrentcontroller.html#responsive\\_offcanvas](https://se.mathworks.com/help/physmod/sps/ref/pmsmcurrentcontroller.html#responsive_offcanvas).
- [20] D. Luczak, K. Nowopolski, K. Siembab, and B. Wicher, “Speed calculation methods in electrical drive with non-ideal position sensor”, in *2014 19th International Conference on Methods and Models in Automation and Robotics (MMAR)*, IEEE, Sep. 2014, pp. 726–731, ISBN: 978-1-4799-5081-2. DOI: 10.1109/MMAR.2014.6957444. [Online]. Available: <http://ieeexplore.ieee.org/document/6957444/>.
- [21] Yung-kang Chin, “A PERMANENT MAGNET SYNCHRONOUS MOTOR FOR AN ELECTRIC VEHICLE - DESIGN ANALYSIS”, Stockholm, Tech. Rep., 2004. [Online]. Available: <http://www.diva-portal.org/smash/get/diva2:7754/fulltext01>.
- [22] *Module 6: Current Sensing (Part 1/2) | NXP Community*. [Online]. Available: <https://community.nxp.com/thread/469445>.
- [23] *The Lorentz force*. [Online]. Available: <http://farside.ph.utexas.edu/teaching/em/lectures/node33.html>.

- [24] H. International Inc, “MICRO SWITCH Sensing and Control HALL EFFECT SENSING AND APPLICATION”, Tech. Rep. [Online]. Available: <https://sensing.honeywell.com/honeywell-sensing-sensors-magneto-resistive-hall-effect-applications-005715-2-en2.pdf>.
- [25] *Hall Effect Sensor and How Magnets Make It Works*. [Online]. Available: <https://www.electronics-tutorials.ws/electromagnetism/hall-effect.html>.
- [26] “HAH1DRW 400-S Mechanical characteristics”, Tech. Rep. [Online]. Available: [www.lem.com](http://www.lem.com).
- [27] A. D. Saha, “Design and Performance Validation of Closed Loop Hall Effect Current Sensor Using High Bandwidth Class D Amplifier A Project Report Submitted in Partial Fulfillment of Requirements for the Degree of Master of Engineering in Electrical Engineering”, Tech. Rep., 2015. [Online]. Available: [http://www.ee.iisc.ac.in/new/people/faculty/vjohn/pdf/ME2015\\_AalokDyutiSaha.pdf](http://www.ee.iisc.ac.in/new/people/faculty/vjohn/pdf/ME2015_AalokDyutiSaha.pdf).
- [28] H. International Inc, “Product Range Guide SENSING AND CONTROL Current Sensors”, Tech. Rep. [Online]. Available: [www.honeywell.com/sensing](http://www.honeywell.com/sensing).
- [29] *Galvanic Isolation: Purpose and Methodologies*. [Online]. Available: <https://www.allaboutcircuits.com/technical-articles/galvanic-isolation-purpose-and-methodologies/>.
- [30] “Selecting the Most Effective Current Sensing Technology”, Tech. Rep. [Online]. Available: [www.raztec.co.nz](http://www.raztec.co.nz).
- [31] “CFS1000 Integrated MagnetoResistive Current Sensor”, Tech. Rep. [Online]. Available: [https://www.sensitec.com/fileadmin/sensitec/Service\\_and\\_Support/Downloads/Data\\_Sheets/CFS1000/SENSITEC\\_CFS1000\\_DSE\\_03.pdf](https://www.sensitec.com/fileadmin/sensitec/Service_and_Support/Downloads/Data_Sheets/CFS1000/SENSITEC_CFS1000_DSE_03.pdf).
- [32] W. Prillwitz and C. Nau, “Architecture of an Integrated AMR current sensor (IACS) System for a Wide Range of Automotive Applications”, Dortmund, 2011. [Online]. Available: <https://www.ama-science.org/proceedings/getFile/AGD1>.
- [33] “MagnetoResistive Current Sensor”, Tech. Rep. [Online]. Available: [https://www.sensitec.com/fileadmin/sensitec/Service\\_and\\_Support/Downloads/Product\\_Information/Application\\_Notes/SENSITEC\\_CFS1000\\_ANE\\_00.pdf](https://www.sensitec.com/fileadmin/sensitec/Service_and_Support/Downloads/Product_Information/Application_Notes/SENSITEC_CFS1000_ANE_00.pdf).
- [34] Han-Su Jung, Jang-Mok Kim, Cheul-U Kim, and Cheol Choi, “Diminution of current measurement error for vector controlled AC motor drives”, in *IEEE International Conference on Electric Machines and Drives, 2005.*, IEEE, 2005, pp. 551–557, ISBN: 0-7803-8987-5. DOI: 10.1109/IEMDC.2005.195777. [Online]. Available: <http://ieeexplore.ieee.org/document/1531395/>.
- [35] S. Hwang, H. Kim, J. Kim, Hui Li, and Liming Liu, “Compensation of amplitude imbalance and imperfect quadrature in resolver signals for PMSM drives”, in *2009 IEEE Energy Conversion Congress and Exposition*, IEEE, Sep. 2009, pp. 1720–1725, ISBN: 978-1-4244-2893-9. DOI: 10.1109/ECCE.2009.5316214. [Online]. Available: <http://ieeexplore.ieee.org/document/5316214/>.
- [36] *Rotation angle sensor (resolver) for EV/HEV drive motor - MinebeaMitsumi*. [Online]. Available: <https://www.minebeamitsumi.com/english/strengths/column/resolver/>.

- [37] *Resolvers, Optical Encoders and Inductive Encoders*. [Online]. Available: <https://www.zettlex.com/articles/resolvers-optical-encoders-and-inductive-encoders/>.
- [38] *Encoder Resolution, Encoder Accuracy & Repeatability | Dynapar*. [Online]. Available: [https://www.dynapar.com/knowledge/encoder\\_resolution\\_encoder\\_accuracy\\_repeatability/](https://www.dynapar.com/knowledge/encoder_resolution_encoder_accuracy_repeatability/).
- [39] *AMT Absolute Encoders - CUI | DigiKey*. [Online]. Available: <https://www.digikey.com/en/product-highlight/c/cui/amt-absolute-encoders>.
- [40] “Capacitive sensors versus inductive sensors - Zettlex”, [Online]. Available: <https://www.zettlex.com/articles/a-comparison-of-inductive-and-capacitive-position-sensors/>.
- [41] *Capacitive Encoders Deliver Durability and Precision | Machine Design*. [Online]. Available: <https://www.machinedesign.com/technologies/capacitive-encoders-deliver-durability-and-precision>.
- [42] *A Comparison of Resolvers, Inductive Encoders and Optical Encoders*. [Online]. Available: <https://www.azom.com/article.aspx?ArticleID=14783>.
- [43] *What is an inductive sensor? - Zettlex*. [Online]. Available: <https://www.zettlex.com/what-is-an-inductive-sensor/>.
- [44] *Inductive encoder technology*. [Online]. Available: <https://www.posic.com/EN/inductive-encoder-technology.html>.
- [45] M. Howard, “The new generation of inductive sensors”, *World Pumps*, vol. 2013, no. 2, pp. 10–11, Feb. 2013, ISSN: 0262-1762. DOI: 10.1016/S0262-1762(13)70055-5. [Online]. Available: <https://www.sciencedirect.com/science/article/pii/S0262176213700555>.
- [46] *IncOder Inductive Angle Encoder | Inductive Encoder*. [Online]. Available: <https://www.zettlex.com/products/incoder/>.
- [47] *Optical Encoders Versus Inductive Encoders*. [Online]. Available: <https://www.zettlex.com/articles/optical-encoders-versus-inductive-encoders/>.
- [48] Li Yongdong and Zhu Hao, “Sensorless control of permanent magnet synchronous motor — a survey”, in *2008 IEEE Vehicle Power and Propulsion Conference*, IEEE, Sep. 2008, pp. 1–8, ISBN: 978-1-4244-1848-0. DOI: 10.1109/VPPC.2008.4677421. [Online]. Available: <http://ieeexplore.ieee.org/document/4677421/>.

# Appendix

## Appendix 1 - Controller subsystem block

The continuous controller subsystem block in the Simulink model is shown in Figure 48.

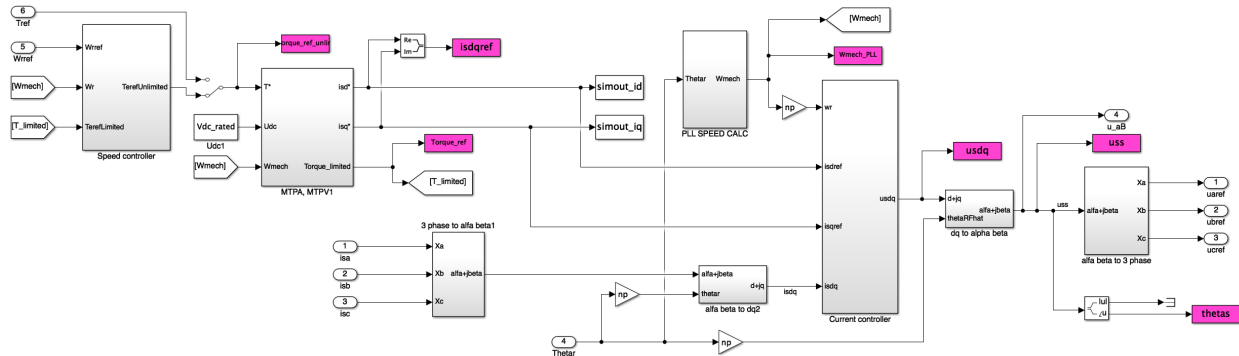


Figure 48: Inside the continuous controller subsystem block in the Simulink model.

The discretized controller subsystem block in the Simulink model is shown in Figure 49.

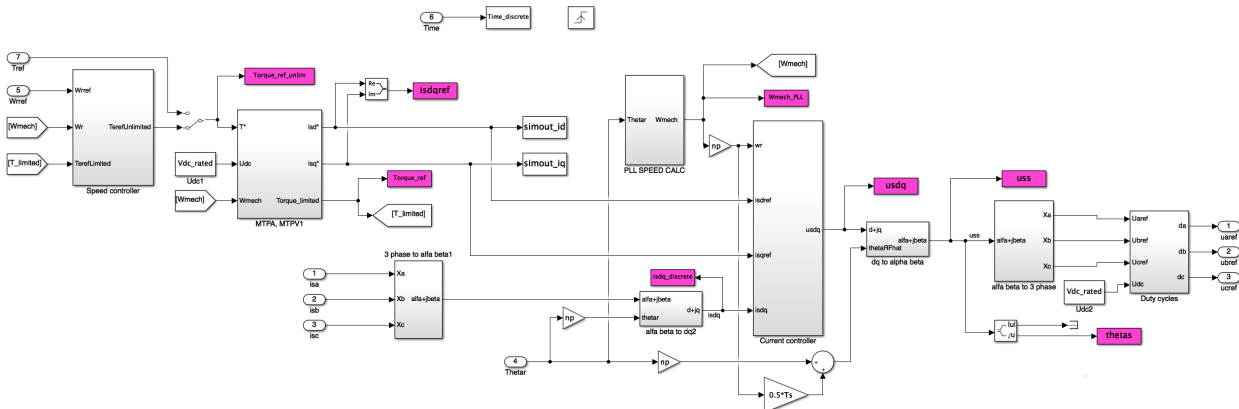


Figure 49: Inside the discretized controller subsystem block in the Simulink model.

In reality there is a time delay in the system due to the computation time of the processor. In this discrete model however, this computational time delay is not considered.

The MTPA block inside the controller in the Simulink model is shown in Figure 50.

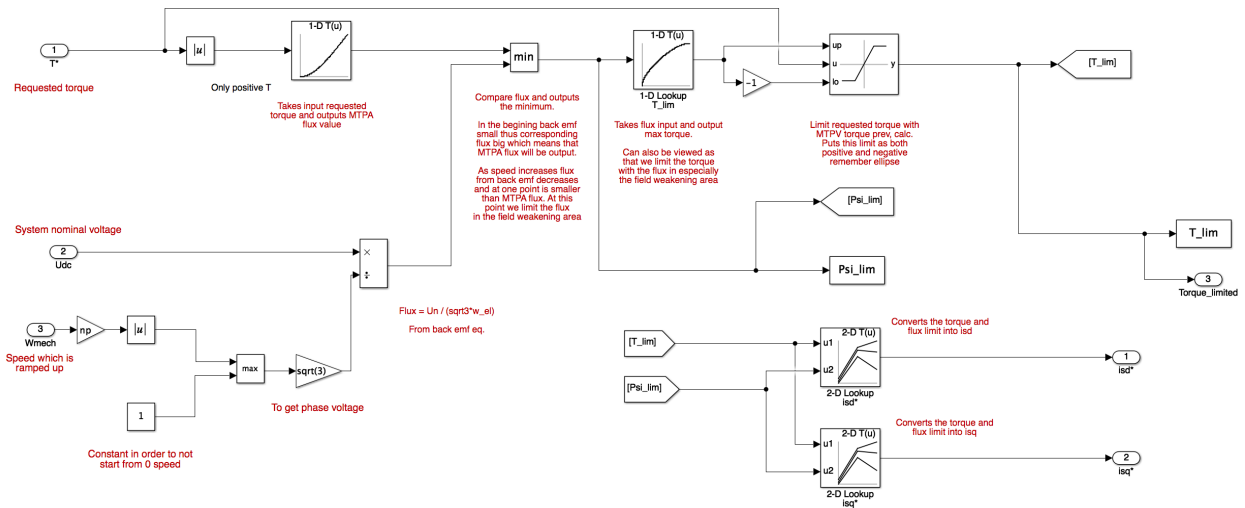


Figure 50: The MTPA subsystem block inside the controller in the Simulink model.

The current controller block inside the controller in the Simulink model is shown in Figure 51.

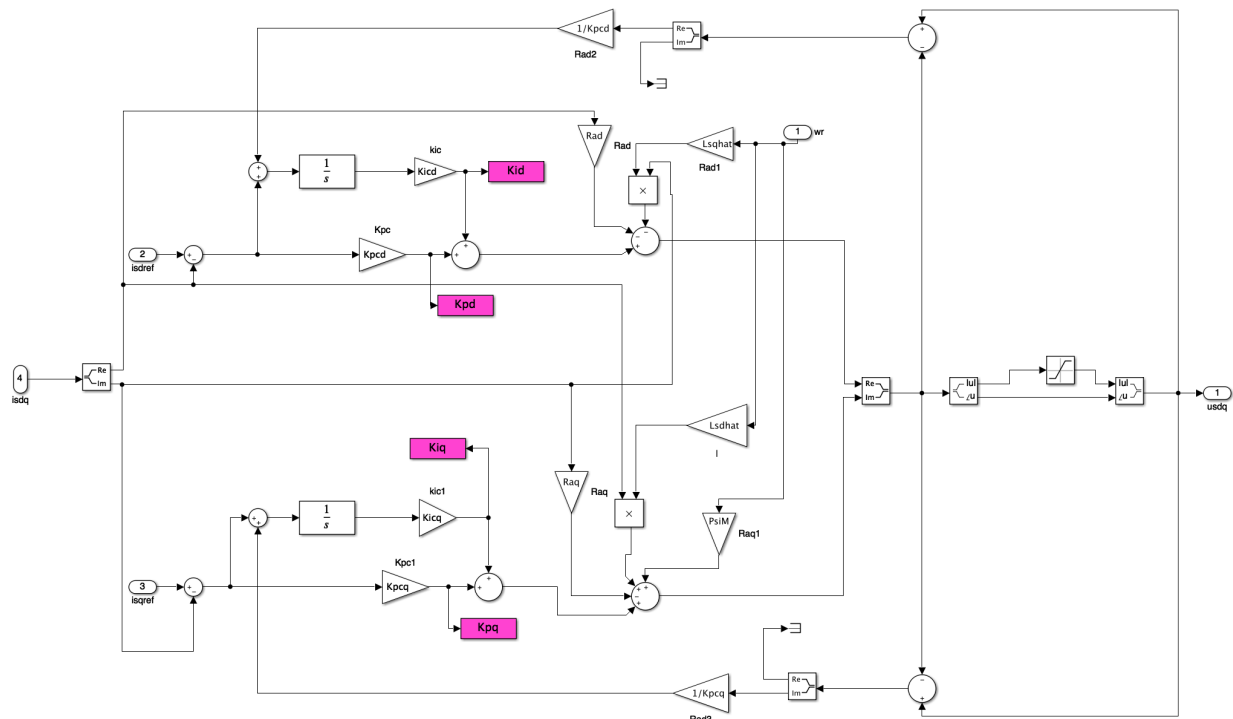


Figure 51: The Current controller subsystem block inside the controller in the Simulink model.

The PLL block inside the controller in the Simulink model is shown in Figure 52.

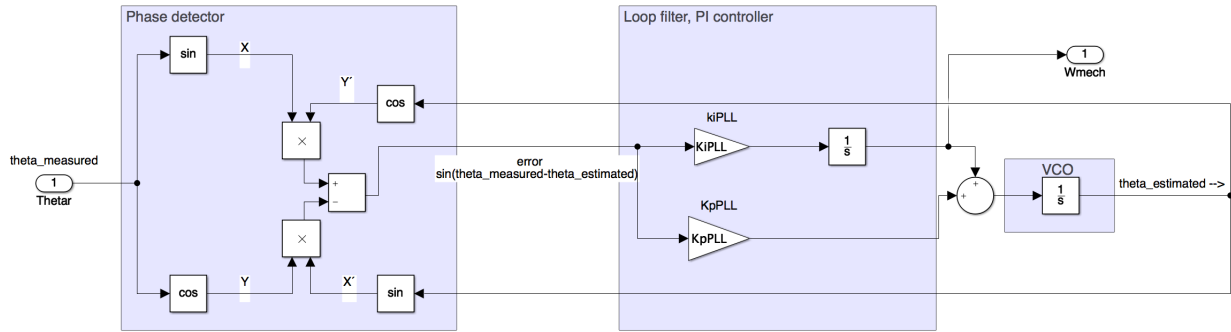


Figure 52: The PLL subsystem block inside the controller in the Simulink model.

The Speed controller block inside the controller in the Simulink model is shown in Figure 53.

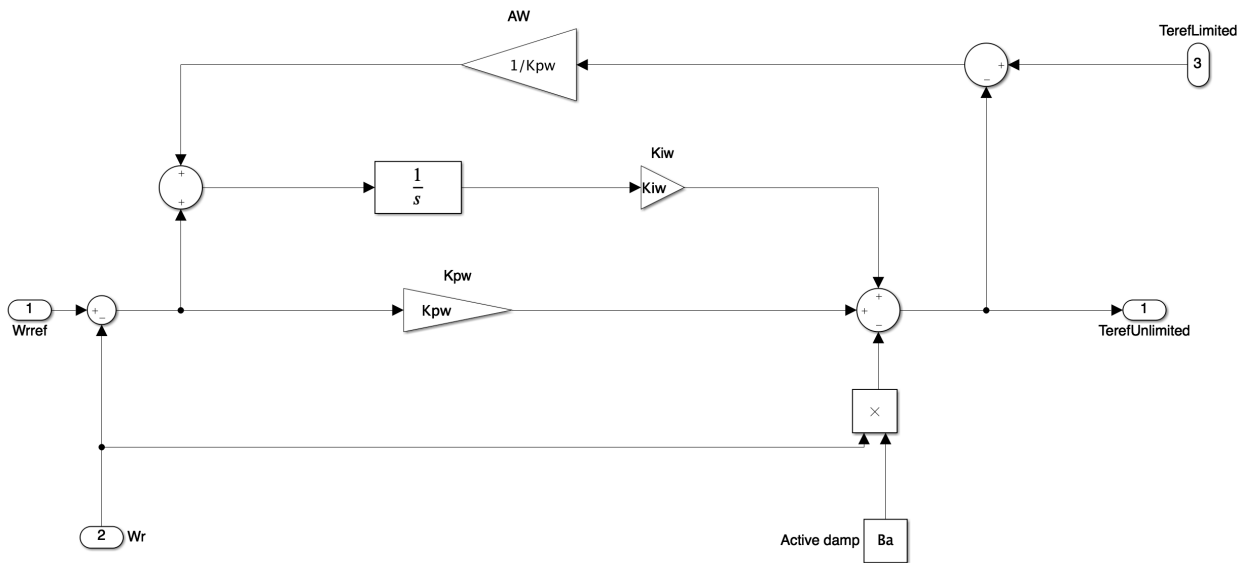


Figure 53: The Speed Controller subsystem block inside the controller in the Simulink model.

## Appendix 2 - PMSM subsystem block

The PMSM subsystem block in the Simulink model is shown in Figure 54.

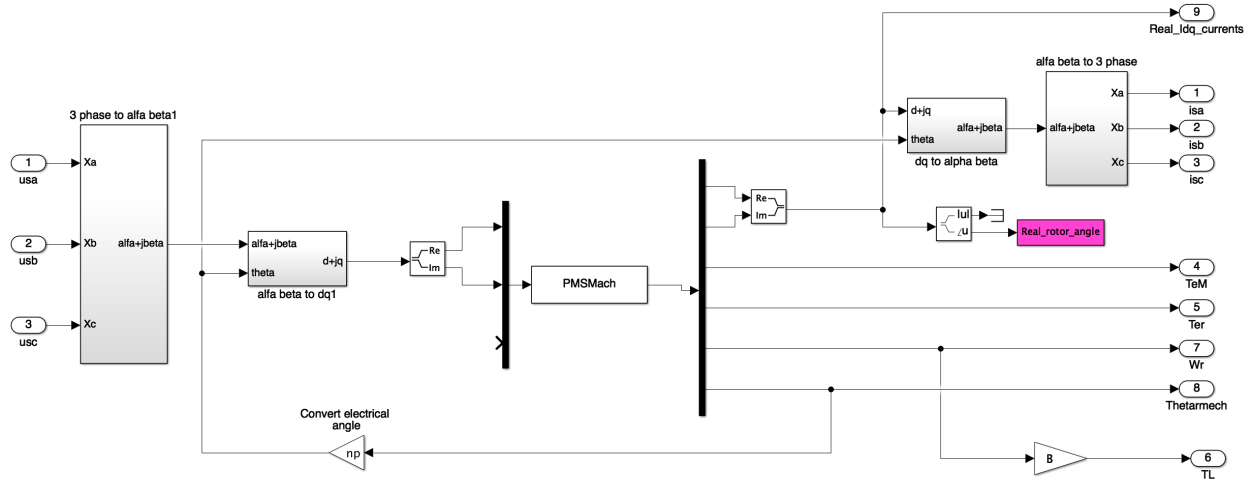


Figure 54: The PMSM subsystem block in the Simulink model.

## Appendix 3 - Overview of discrete system

An overview of the discretized Simulink model is shown in Figure 55.

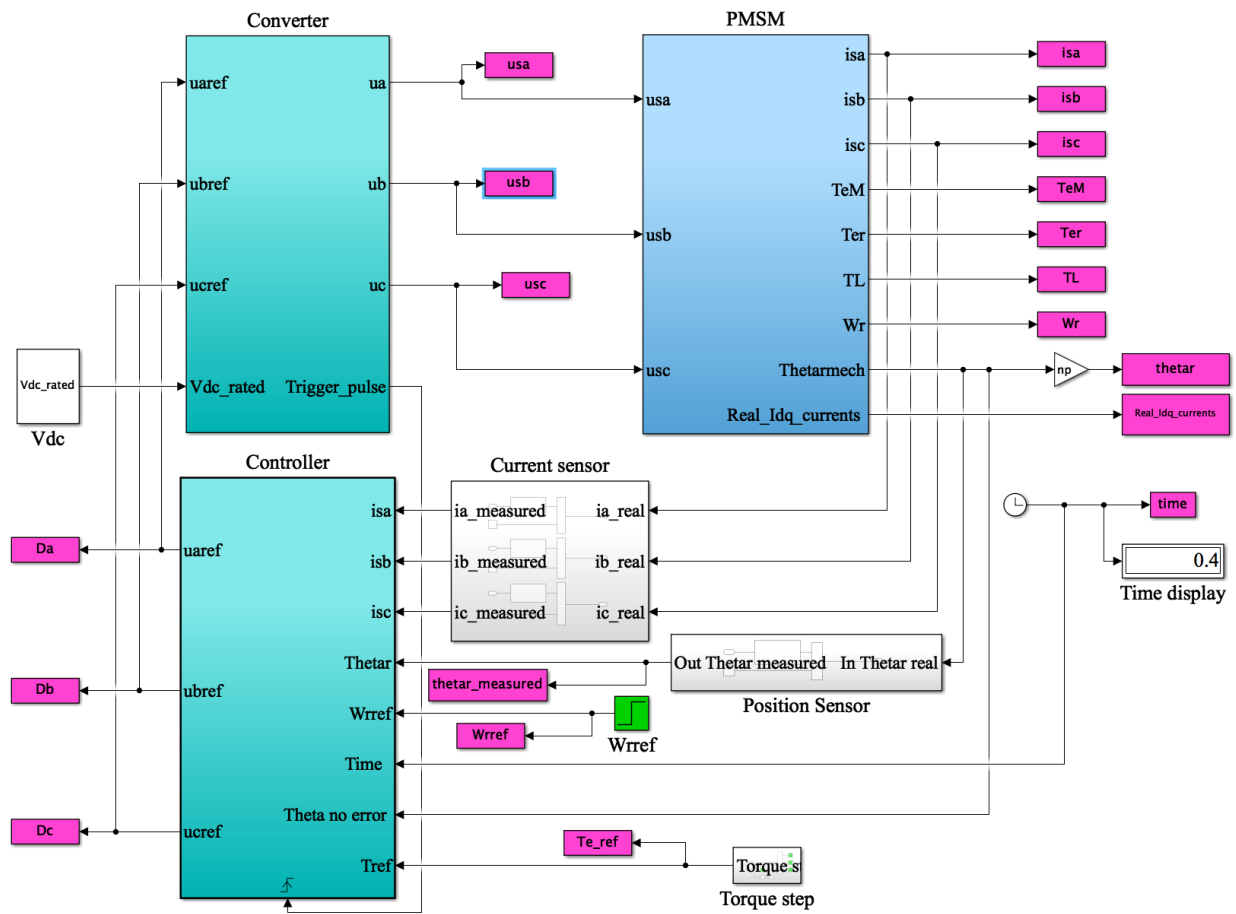


Figure 55: The discretized simulink model.

## Appendix 4 - Converter subsystem block

The discretized converter subsystem block in the Simulink model is shown in Figure 56.

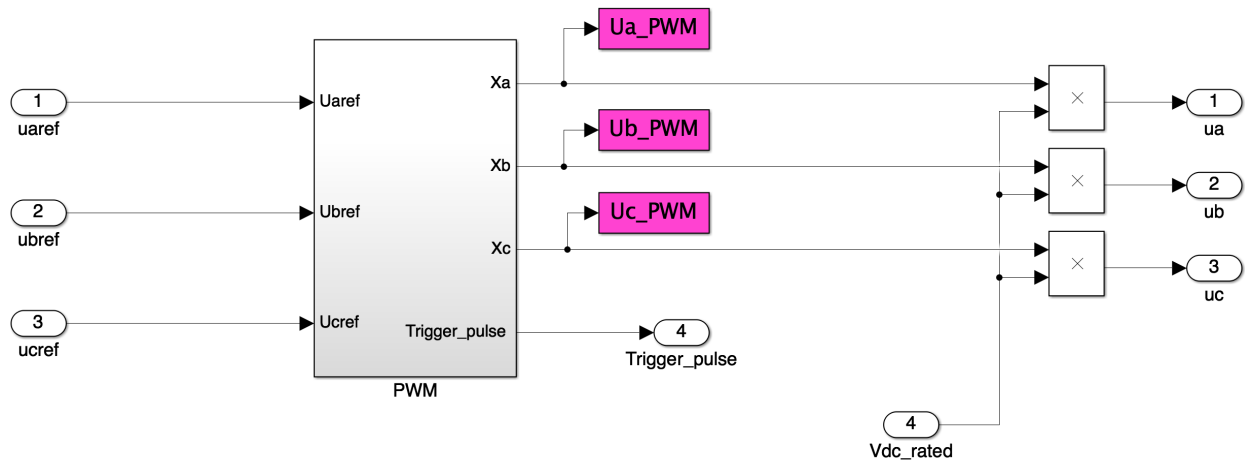


Figure 56: The discretized converter subsystem block in the Simulink model.

The PWM inside the discretized converter subsystem block is shown in Figure 57.

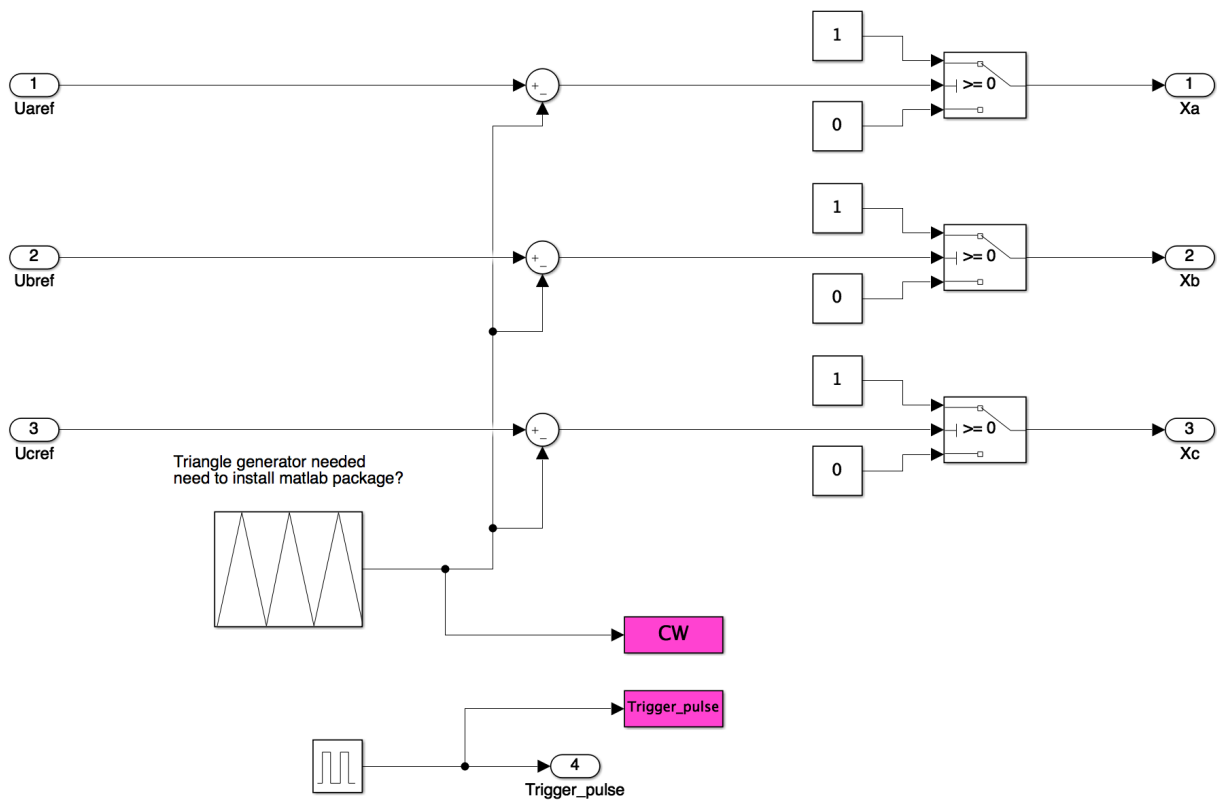


Figure 57: The PWM inside the converter subsystem block.

The Duty cycle subsystem block is shown in Figure 58.

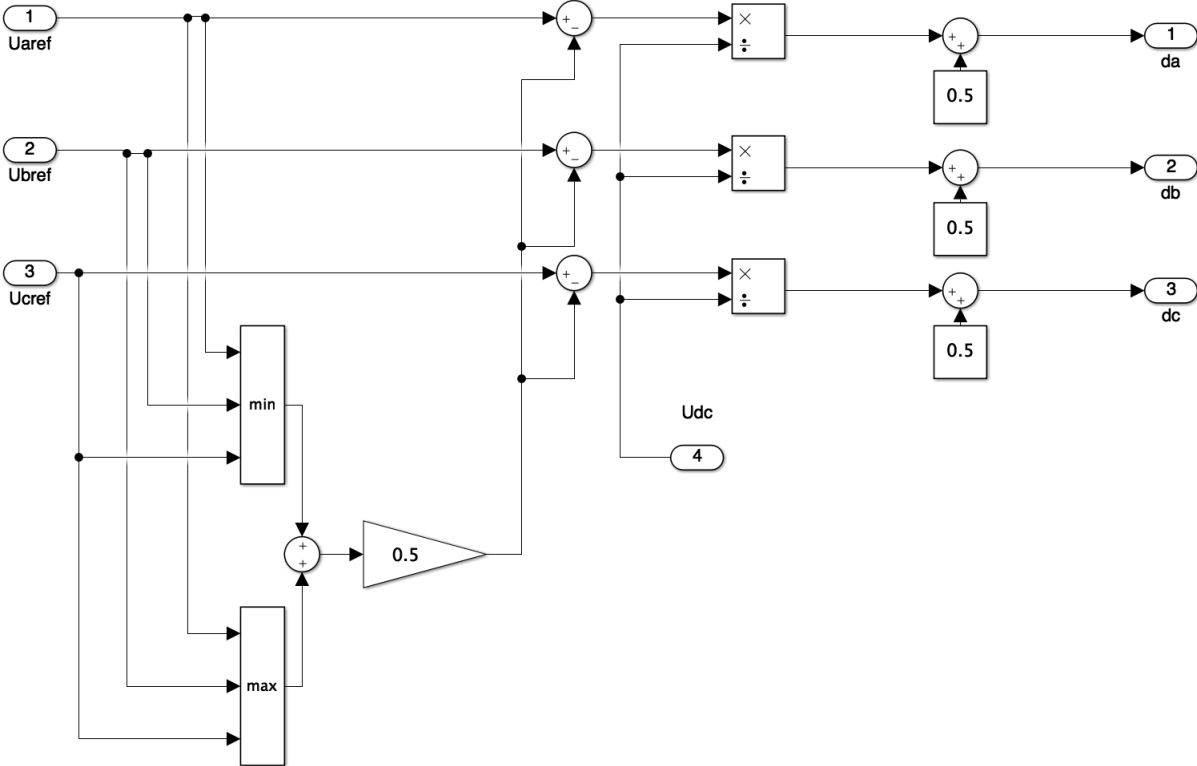


Figure 58: The Duty Cycle block.